Volcanic edifice slip events recorded on the fault plane of the San Andrés Landslide, El Hierro, Canary Islands

Jan Blahůt, Ivanka Mitrovic-Woodell, Ivo Baroň, Miloš René, Matt Rowberry, Pierre-Henri Blard, Filip Hartvich, Jan Balek, Stavros Meletlidis

Elsevier Editorial System(tm) for Tectonophysics

Manuscript Draft

Manuscript Number: TECTO13649R1

Title: Volcanic edifice slip events recorded on the fault plane of the San Andrés Landslide, El Hierro, Canary Islands

Article Type: Research Paper

Keywords: volcanic collapse; frictionite; cataclasis metamorphism; silica layer; cosmogenic radionuclide dating; Canary Islands

Corresponding Author: Dr. Jan Blahut,

Corresponding Author's Institution: Institute of Rock Structure and Mechanics, AS CR

First Author: Jan Blahut

Order of Authors: Jan Blahut; Ivanka Mitrovic-Woodell; Ivo Baroň; Miloš René; Matt Rowberry; Pierre-Henri Blard; Filip Hartvich; Jan Balek; Stavros Meletlidis

Abstract: Volcanic flank collapses often result in giant debris avalanches that are capable of travelling tens of kilometres across the ocean floor and generating tsunamis that devastate distant communities. The San Andrés Landslide on El Hierro, Canary Islands, represents one of the few places in the world where it is possible to investigate the landslide mass and fault planes of a volcanic collapse structure. In this study, a new conceptual model for the development of this enormous slump is presented on the basis of structural geological and geomorphological measurements, petrological and microstructural analyses, and cosmogenic radionuclide dating. Structural geological and geomorphological measurements indicate that the fault plane records two distinct events. Petrological and microstructural analyses demonstrate that a thin layer of frictionite covers the surface of the fault in contact with an oxidised tectonic breccia that transitions into the underlying undeformed basanite host rock. This frictionite comprises a heterogeneous cataclastic layer and a translucent silica layer that are interpreted to represent two separate slip events on the basis of their architecture and crosscutting relationships. Cosmogenic 3He dating reveals a maximum exposure age of 183±17 ka to 52±17 ka. Arguments are presented in support of the idea that the first slip event took place between 545 ka and 430 ka, prior to significant clockwise rotation of El Hierro, and the second slip event took place between 183 ka and 52 ka, perhaps in association with one of the giant debris avalanches that occurred around that time. This is the first time that more than one slip event has been recognised from the fault plane of the San Andrés Landslide. It is also believed to be the first time a silica layer resulting from frictional melt has been described in a volcanic setting.

Research Data Related to this Submission

There are no linked research data sets for this submission. The following reason is given:

Data will be made available on request

*Cover Letter

ÚSTAV STRUKTURY A MECHANIKY HORNIN
Akademie věd ČR, v.v.i.

25/12/2019

Prague, Czechia

Dear Editor,

In name of all the co-authors I would like to submit a reviewed manuscript entitled „Volcanic edifice slip events recorded on the fault plane of the San Andrés Landslide, El Hierro, Canary Islands". We have made thorough revision and we have incorporated the requested information from the editor and both reviewers.

We hope, that the revised manuscript will now be more clear to read and may attract more potential readers.

I hope our manuscript is now in acceptable form,

Yours sincerely,

Jan Blahut

Ústav struktury a mechaniky hornin AV ČR, v.v.i., V Holešovičkách 94/41, 182 09 Praha 8
Tel.: +420266009111, e-mail: irsm@irsm.cas.cz, ID datové schránky: uykngxq
Bankovní spojení: ČNB Praha, 94-10825081/0710, IČO: 67985891, DIČ: CZ67985891

*Abstract
Click here to download Abstract: Abstract.docx

Volcanic edifice slip events recorded on the fault plane of the San Andrés Landslide, El Hierro, Canary Islands

Volcanic flank collapses often result in giant debris avalanches that are capable of travelling tens of kilometres across the ocean floor and generating tsunamis that devastate distant communities. The San Andrés Landslide on El Hierro, Canary Islands, represents one of the few places in the world where it is possible to investigate the landslide mass and fault planes of a volcanic collapse structure. In this study, a new conceptual model for the development of this enormous slump is presented on the basis of structural geological and geomorphological measurements, petrological and microstructural analyses, and cosmogenic radionuclide dating. Structural geological and geomorphological measurements indicate that the fault plane records two distinct events. Petrological and microstructural analyses demonstrate that a thin layer of frictionite covers the surface of the fault in contact with an oxidised tectonic breccia that transitions into the underlying undeformed basanite host rock. This frictionite comprises a heterogeneous cataclastic layer and a translucent silica layer that are interpreted to represent two separate slip events on the basis of their architecture and crosscutting relationships. Cosmogenic ^{3}He dating reveals a maximum exposure age of 183±17 ka to 52±17 ka. Arguments are presented in support of the idea that the first slip event took place between 545 ka and 430 ka, prior to significant clockwise rotation of El Hierro, and the second slip event took place between 183 ka and 52 ka, perhaps in association with one of the giant debris avalanches that occurred around that time. This is the first time that more than one slip event has been recognised from the fault plane of the San Andrés Landslide. It is also believed to be the first time a silica layer resulting from frictional melt has been described in a volcanic setting.

***Revision Notes**
Click here to download Revision Notes: Revision notes.docx

Dear Editor,

The comments of you and the reviewers are in black, while our responses are in red.

Editor:

Dear authors,
At long last I have received two evaluations of your work — many potential reviewers have in fact turned down the review invitation.

While the manuscript has clear merits, there are still some significant issues:

— a more thorough and general introduction should be provided on fault slip and as to how peculiar volcanic edifices may be, and why we should care about the seismicity of landslides there. As Rev#1 points out, it is somewhat unclear "why being in a volcanic setting is noteworthy". This echoes one of your conclusions, ie "This is the first time that more than one slip event has been recognised from the fault plane of the San Andrés Landslide", which does not sound so ground breaking to me (if I may play with words).
We have rewritten the introduction to capture the readers´ interest. We hope, that now the scope of the study is clearer.

— Some petrographic features at the dm-cm scale are missing to ensure a correct scale transfer of descriptions, say from Fig.2 to say Fig. 5.
We have added new photos of MSA1 and MSA2 samples to Fig.2, followed by detailed description. We believe, that this might be sufficient to transfer from Fig.2 to Figs. 5, 6 and 7.

— why are cosmogenic ages not discussed more thoroughly and reported on the surface? I find this really problematic. Table 1 is simply not enough and data should be scrutinized.
We have carefully rewritten this part as we understand that the explanation presented was not enough. We explained the reasons why the cosmogenic ages yielded such different results.

— any hint as to the respective sizes of the landslides? as to a paleomagnitude?...
We have added this information to chapter 2.1.

— You should pay attention to details. Care should be taken about statements such as: "strong ground shaking" (L493), which is not substantiated.
We have corrected this statement – see answer to reviewer 2 (p. 18, l. 493). We also checked the manuscript and corrected such general statements where needed.

— the write-up could be improved. For example, conclusions should be made much more concise and straight to the point. The first part basically repeats the incentive of the study.
We have rewritten the conclusions to be more concise.

— Take-home message: note that there is no scale to Fig. 9. This also does not seem to me like a very impactful take-home message figure and could probably be improved.

We have added the scale to Fig. 9. As the reviewer 2 likes the figure being very illustrative we would like to keep this figure in the manuscript.

Should you be able to address this criticism with the greatest care, I would welcome receiving a thoroughly revised version of your work.

Good luck with your efforts,
Best regards
Philippe

Reviewer 1:

Reviewer #1: I am afraid that I was not the best choice of reviewer for this manuscript as I have no expertise to evaluation most of the material presented. Acknowledging my nearly complete lack of knowledge about how to measure and interpret geologic features at the scales considered in this paper, or the analyses used, the manuscript seems clearly written and analyses very thorough. The authors do not appear to over-interpret the results, acknowledging the uncertainties in the various measurements and interpretations and how they may or may not fit together. Again, I am unable to comment on any of the details.
My only recommendation is that the paper would have broader appeal if there was greater motivation and discussion of issues related to fault slip in a broader context; what do their results imply for current models of fault reactivation, stationarity in process, etc., at multiple scales? The authors also emphasize the fact that this is the first time some of their observations have been made in a volcanic setting, and while perhaps it may be obvious to some why being in a volcanic setting is noteworthy, it is not clear to me why this is noteworthy. Is there something about a volcanic setting that makes the faulting processes inferred surprising?
We have rewritten the abstract, introduction and conclusions so the scope of our study should be clearer and have broader appeal.

I have included very minor comments (mostly grammatical suggestions) in the annotated manuscript returned

p.18, l. 486-487: The typing error in Széréméta et al. (1997) was corrected to (1999).
1. Surname of the corresponding author is Blahůt, in caps BLAHŮT (see references, small circle over the u/U). This was corrected. I used to use "Blahut" without circle over u in the past.

2. Some sentences are difficult to understand, I recommend to reformulate them:

p. 7, r. 161: *The first gives a ground plan view* ... – missing subject
This was corrected.

p. 7, r. 169: *In total eighty eight test sites were sampled* ... – missing subject
This was corrected.

p.7, r. 171: ..., *as is standard protocol*, ... – missing subject
This was corrected.

p. 12, r. 316-318: *The host rocks ... These are mainly pyroxene, plagioclase, olivine, and amphibole together with the accessory minerals apatite, chromite, magnetite, and Ti-magnetite.* – "These" means minerals or rocks, or adjectives to rocks??
This was corrected – These means rocks.

p. 12, r. 319: ... *with an acid rim, An45–70, and a basic core, An79–83*. – I suppose description from core to rim.
This was corrected.

p. 12, r. 321–322: *A high amount of volcanic glass is present while basanites with subordinate amounts of volcanic glass contain frequent phenocrysts of olivine*. – The sentence that follows the previous description of bazanites makes no sense in this formulation.
This was corrected.

p. 12, r. 328: ... *The tectonic breccias host cracks filled by zeolite veins* ... – either the breccias are cut by zeolite veins, or cracks are filled by zeolite. Veins are "filled cracks".
This was corrected.

p. 13, r. 338–339: *Instead attention focuses here on the layers that overlie the tectonic breccia*. – Totally incomprehensible formulation for me.
This was corrected.

p. 13, r. 355: ... *cracks parallel* ... - missing *are*?
This was corrected.

p. 16, r. 429: ... *with horizontal Y- shears, parallel to the slip surface* ... – the slip surface is inclined: what does it mean "*horizontally*" – in the field or in a figure 5?
This was corrected. Y-shears are parallel to the slip surface.

p. 18, r. 479: ... *due to the fact it acts as a lubricant* ... - missing "that"?
This was corrected.

p. 18, r. 497–498: ... *the fault could only have been active only for a geologically short period* ... – double "only".
This was corrected.

p. 29, r. 787: The caption "*Stereoplot of the structural geological measurements* ..." says nothing about what it is. I recommend to use "*Orientation of the fault surface ...*" supplemented by information that it is an *azimuthal projection in the lower hemisphere*.
This was corrected.

3. It is necessary to unify the designation of the year: *yr* (p. 6, r. 140) vs. *a* (p. 9, r. 238 and others). The unit *mm/yr–1* at the same place is nonsense (double "over").
This was corrected to "a" to be unified with the rest of the paper.

4. A problem that goes through much of the text is writing a comma. Use commas to set off introductory elements (as it correctly shown):

- p. 2, r. 26: ... *study, a new* ...

- p. 6, r. 160: ... *cloud, it was* ...
- p.9, r. 244: ... *In theory, the magmatic* ...
- p. 11, r. 293: ... *Most commonly, the striations* ...
- p. 13, r. 339: ... *microscopy, it is* ...
- p. 13, r. 345: ... *samples, it is* ...
- p. 17, r. 450: ... *senses, they are* ...
- p. 18, r. 496: ... *In that study, it was* ...
- p. 19, r. 516: ... *surface, it has been* ...

I suppose to use comma in other cases, such as:
- p. 19, r. 517: ... *event, as evidenced by the cataclastic layer, is proposed* ...
- p. 4 r. 101: ... *Series, which* ... ; p. 6, r. 149: ... *slickenlines, which* ..., etc.

Comma is not needed behind series of adjectives, such as:
- p. 5, r. 103 ... *The most recent, ongoing phase* ...
- p. 5, r. 127 ... *acurate, and presumably listric fault system* ...
- p.15, r. 398: ... *minor, most probably slow displacement* ...

The commas were corrected.

5. Do not use the word *measurements* for data obtained (or directional data): p. 4, r. 84; p. 11, r. 283; p. 29, r. 787.

This was corrected.

6. Indicate that the directions are given as azimuths (p. 11).

This was corrected.

7. For better understanding of the text, I recommend inserting referenced word after the pronouns, such as *this* (p. 6, r. 149), *these* (p. 11, r. 295; p. 12, r. 316), *those* (p. 17, r. 449), although it is not essential.

This was corrected.

8. Two brackets next to each other are not suitable: p. 5, r. 112; p. 9, r. 225; p. 12, r. 325. Two brackets inside each other are not suitable: p. 9, r. 241; p. 13, r. 348.

This was corrected.

9. I suppose to use original spelling for *pseudotachylyte* (Shand, 1916: The Pseudotachylyte of Parijs, Orange Free State, and its Relation to 'Trap-Shotten Gneiss' and 'Flinty Crush-Rock'. *Quarterly Journal of the Geological Society*, **72**, 1–4, *198–221*.) instead of misspelled *pseudotachylite* (p. 15, r. 413 and others), even if it is incorrectly mentioned in the recommendation of Subcommission on the Systematics of Metamorphic Rocks (Fettes & Desmons, 2007: *Metamorphic Rocks – A Classification and Glossary of Terms*).

This was corrected. We accept the recommendation from the reviewer to use the original term (after Shand 1916). A lot of researchers use the other spelling version, as it is seen as the correct one. Out of curiosity, a Tweeter poll was conducted by one of the authors to check what researches prefer: 61% voted for “pseudotachylite”, and 39% for “pseudotachylyte” (out of 83 votes).

Reviewer 2:

Abstract
This was corrected.

p.3, l. 52-53: Where? Globally, in the Nicaraguan Highlands (presumably in Nicaragua?), Canary Islands?
In the whole world – this was corrected.

p.3, l. 54: put in parentheses
This was corrected.

p.3, l. 69: "... development of foliation." Is this what distinguishes cataclasites from frictionite, or are cataclasites a type of frictionite?
We have rewritten this part to be more clear.

p.3, l. 69-70: "Fast slip along shallow fault.." Are the features described here for faults also considered frictionite? The potential similarities and differences between faults and landslides needs clarification; is the implication that they form similar, but not identical structures?
We have rewritten this part to be more clear.

p. 4, l. 77-78: As noted above, it isn't clear that these aggregates or silica layers are observed on landslides generally? Might be useful to say why one might expect things to be different or similar in a volcanic setting (i.e., why does the setting matter)?
Cataclasites or frictionites are normally not observed on landslides. Only few exceptions exist (e.g. Köfels, Tsego-Ri, Arequipa) in case there is large landslide (or rockslide/rock avalanche in particular) able to generate enough frictional heat to produce re-melting of thin layer if rocks.

p. 5, l. 105: How could it have ended in 2012 and lasted until 2014?
The seismic activity lasted from July 2011 till 2014, during that period an offshore eruption occurred (10/10/2011 – March 2012). This sentence was rewritten.

p. 17, l. 458: This sentence needs a verb!
This was corrected.

p. 17, l. 471: This sentence also needs a verb!
This was corrected.

p. 18, l. 481: Figures 8 and 9 are great - they summarize the interpretation in simple, straightforward ways!
Thank you, we also improved these figures according to the reviewers´ and editor´s suggestions.

p. 18, l. 493: "... accompained by ground shaking..." Is the implication here that shaking initiated both the El Golfo debris avalanche and this second slip event, or that the former caused the shaking? If the latter, it's not clear that the shaking would be sufficient (I'd expect low amplitude shaking from a debris avalanche as the coupling efficiency would be low).

We agree with the reviewer, that the shaking induced from the debris avalanche itself wouldn´t be probably enough to cause re-activation of San Andrés Landslide. As more information about triggers of these giant debris avalanches is not known we changed the sentence to reflect this.

p. 18, l. 494: should be 'a model'
This was corrected.

p. 18, l. 497: omit “only”
This was corrected.

Figure 3: What do different colors represent?
The different colours of arrows represent distinct sets of striations and elongated bumps. We have added this explanation to the captions.

Figure 4: should be 'black circles' or 'black dots'?
This was corrected.

Figure 8: Add 'Age before present' to indicate what these numbers are?
We have added this to the figure captions as it is graphically nicer.

Highlights

- Landslide frictionite adorns the fault plane of the San Andrés Landslide on El Hierro
- The frictionite comprises a dark cataclastic layer and a translucent silica layer
- These cataclastic and silica layers formed during two separate fault slip events
- Microstructural observations in good agreement with observations at the outcrop scale
- It is suggested that the fault slip events occurred between 545-430 ka and 183-52 ka
- First time that more than one slip event has ever been recognised on a single fault plane resulting from volcanic flank collapse on an oceanic island
- First time a silica layer resulting from frictional melt has been described from a volcanic setting

Volcanic edifice slip events recorded on the fault plane of the San Andrés Landslide, El Hierro, Canary Islands

Jan ~~BLAHUT~~[a]BLAHŮT[a], Ivanka MITROVIC-WOODELL[b], Ivo BARONŇ[a], Miloš RENÉ[c~~a~~], Matt ROWBERRY[a], Pierre-Henri BLARD[~~d~~c], Filip HARTVICH[a], Jan BALEK [a], Stavros MELETLIDIS[~~e~~d]

[a] ~~Department of Engineering Geology,~~ Institute of Rock Structure ~~&~~ and Mechanics, The Czech Academy of Sciences, V Holešovičkách 41, 182 09 Prague 8, Czech Republic

[b] Department of Geodynamics and Sedimentology, University of Vienna, Althanstraße 14, 1090 Vienna, Austria

~~[c] Department of Geochemistry, Institute of Rock Structure & and Mechanics, The Czech Academy of Sciences, V Holešovičkách 41, 182 09 Prague 8, Czech Republic~~

[~~d~~c] Centre de Recherches Pétrographiques et Géochimiques (CRPG), UMR 7358, CNRS - Université de Lorraine, 15 rue Notre Dame des Pauvres, 54500 Vandœuvre-lès-Nancy, France

[~~e~~d] Centro Geofísico de Canarias, Instituto Geográfico Nacional, Calle Marina 20, 38001 Santa Cruz de Tenerife, Spain

* corresponding author: blahut@irsm.cas.cz

Abstract: Volcanic flank collapses often result in giant debris avalanches that are capable of travelling tens of kilometres across the ocean floor and generating tsunamis that devastate distant communities. The San Andrés Landslide on El Hierro, Canary Islands, represents one of the few places in the world where it is possible to investigate the landslide mass and fault planes of a volcanic collapse structure. In this study, a new conceptual model for the development of this enormous slump is presented on the basis of structural geological and geomorphological measurements, petrological and microstructural analyses, and cosmogenic radionuclide dating. Structural geological and geomorphological measurements indicate that the fault plane records two distinct events. ~~The first event is associated with features plunging 111° and the second is associated with features plunging 125° and 131°.~~ Petrological and microstructural analyses demonstrate that a thin layer of frictionite covers the surface of the fault in contact with an oxidised tectonic breccia ~~which~~ that transitions into the underlying undeformed basanite host rock. This frictionite comprises a heterogeneous cataclastic layer and a translucent silica layer ~~which~~ that are interpreted to represent two separate slip events on the basis of their architecture and crosscutting relationships. Cosmogenic ^{3}He dating reveals a maximum exposure age of 183±17 ka to 52±17 ka. ~~The high degree of variability between the replicate samples reflects the uncertainty associated with estimating the magmatic ^{3}He.~~ Arguments are presented in support of the idea that the first slip event took place between 545 ka and 430 ka, prior to significant clockwise rotation of El Hierro, and the second slip event took place between 183 ka and 52 ka, perhaps in association with one of the giant debris avalanches that occurred around that time. This is the first time that more than one slip event has been recognised from the fault plane of the San Andrés Landslide. It is also believed to be the first time a silica layer resulting from frictional melt has been described in a volcanic setting.

Keywords volcanic collapse; frictionite; cataclasis~~tic~~ metamorphism; silica layer ~~formation~~; cosmogenic radionuclide dating; Canary Islands

1. Introduction

Gravitational slope failures generate~~often produce~~ geological structures at a range of scales that are ~~either~~ similar or identical to those that result from~~related to endogenous~~ tectonic processes (Jaboyedoff et al., 2013). Consequently, ~~F~~faults generated ~~that originate~~ as a result of large slope failures~~landslides~~ are often analogous to their ~~ose produced by~~ tectonic counterparts~~processes~~ (Gomberg et al., 1995). Some of the largest slope failures on Earth are represented by volcanic flank collapses on oceanic islands – these events are so enormous that they are also comparable to the largest mass movements on Mars (Blahůt et al., 2019). The processes that lead to volcanic flank collapses on oceanic islands are not well understood despite their potential to generate catastrophic tsunamis (Paris et al., 2018; Walter et al., 2019). In part this situation reflects the dearth of events as volcanic flank collapses are estimated to have only occurred four times a century ~~in~~for the past five hundred years (Siebert, 1992). Volcanic flank collapses on oceanic islands are usually represented by debris avalanches (sensu Ui et al., 2000), which displace huge volumes of rock and create amphitheatre shaped calderas (Siebert, 1984). Such debris avalanches localise shear deformation along thin sliding surfaces at the base of the displaced mass (De Blasio and Elverhøi, 2008). These events are triggered by a range of factors which can be broadly categorised as seismogenic or magmagenic (McGuire, 1996). Therefore, while huge debris avalanches may occur in other settings, volcanic flank collapses on oceanic islands are especially dangerous due to the interminable nature of the potential triggering events, i.e. volcanic tremors and related seismicity, coupled with the adjacency of an extremely high risk impact environment, i.e. seawater. The run-up heights of consequent tsunami waves may exceed 100 m (Karstens et al., 2019; Walter et al., 2019). Occasionally, volcanic collapses are represented by creeping or slumping but only a small number of studies have focused on these processes. Examples come from Mount Etna in Sicily (Rasa et al., 1996), Pico Ridge in the Azores (Hildebrand et al., 2012), San Andrés in the Canary Islands (Blahůt et al., 2017), and Hilina Slump in the Hawaiian Islands (Liu et al. 2018).

~~Volcanic collapses usually occur as debris avalanches (sensu Ui et al., 2000), removing huge volumes of rock and generating amphitheatre shaped calderas (Siebert, 1984). These debris avalanches, as with other types of slope deformation, localise shear deformation along thin sliding surfaces at the base of the sliding mass (De Blasio and Elverhøi, 2008). In some instances, it possible to obtain information pertaining to creeping or slumping but such studies are rare. Examples come from Mount Etna in Sicily (Rasa et al., 1996), Pico Ridge in~~

~~the Azores (Hildebrand et al., 2012), San Andrés in the Canary Islands (Blahůt et al., 2017), and Hilina Slump in the Hawaiian Islands (Liu et al. 2018).~~

~~In a volcanic setting it has been found that slow collapse of a Tertiary shield volcano in the Nicaraguan Highlands during the Holocene modified the local palaeostress field and generated normal, reverse, and strike slip faults (Baroň et al., 2011). However, volcanic collapses are somewhat difficult to study because they are comparatively rare events. Such failures have occurred at least four times a century for the past five centuries (Siebert, 1992). These events are triggered by a range of factors which can be broadly categorised as seismogenic or magmagenic (McGuire, 1996). Volcanic collapses usually occur as debris avalanches, (sensue Ui et al., (2000), removing huge volumes of rock and generating amphitheatre shaped calderas (Siebert, 1984). These debris avalanches, as with other types of slope deformation, localise shear deformation along thin sliding surfaces at the base of the sliding mass (De Blasio and Elverhøi, 2008). In some instances, it has been possible to obtain information pertaining to creeping or slumping but such studies are rare. Examples come from Mount Etna in Sicily (Rasa et al., 1996), Pico Ridge in the Azores (Hildebrand et al., 2012), San Andres in the Canary Islands (Blahůt et al., 2017), and Hilina Slump in the Hawaiian Islands (Liu et al. 2018). It is, however, probable that more data will be collected in the future due to the increasingly widespread use of GPS and InSAR.~~

During landslide emplacement, flash heating may occur along thin shear layers to produce frictional melt, referred to as frictionite or landslide pseudotachylyite (Masch et al., 1985; Maddock, 1986; Legros et al., 2000; Lavallée et al., 2012; Mitchell et al., 2015). Frictionite is a subtype of pseudotachylyte, *sensu lato*, which is generated at the base of landslides, as opposed to pseudotachylyte, *sensu stricto*, which is generated in greater depths with higher pressure and temperature conditions (Maddock, 1986). Frictionite tends to have thicknesses of between one and three centimetres and develops parallel or subparallel to the dip of the landslide (Weidinger et al., 2014). Indicators of frictionite include significant grain size reduction, evidence for fluidised flow, and the presence of amorphous material~~, and evidence for fluidised flow.~~ Other types of cohesive fault rocks, such as ~~M~~microbreccias and cataclasites, are common ~~also form~~ during the emplacement of large landslide~~s emplacement. typical indicators of cataclastic deformation are~~ Cataclasites typically show grain size reduction, compared to the host rock, with ~~and the~~ development of foliation. To accurately assess the hazard relating to volcanic flank collapses it is crucial to be able to estimate the strength and velocity of the

landslide. Fast slip along shallow faults ~~is evidenced~~ can be inferred by the presence of devitrified material observed in pseudotachylytes, clast-cortex aggregates (Smith et al., 2011; Han and Hirose, 2012; Rempe et al., 2014), ~~and~~ silica layers (Kirkpatrick et al., 2013; Faber et al. 2014), and other type of fault rock architecture. Pseudotachylytes and frictionites are ultrafine-grained rocks, with the presence of partial melt. ~~The~~ Clast-cortex aggregates ~~former are composed~~comprise of a central clast enclosed within a layer, or concentric layers, of material akin to the matrix (e.g. Anders et al., 2010; Rowe et al., 2012). Silica layers ~~while the latter~~ are composed of translucent silica ~~gel layer~~ with microstructures that exhibit flow banding, armoured clasts, and extreme comminution compared to adjacent rocks (Kirkpatrick et al., 2013; Faber et al., 2014). These fault rock structures are not common – they are known to occur in a range of tectonic settings but have not been reported in relation to volcanic flank collapses. The first report of frictionite at the base of a landslide was described from the Köfels landslide in the Austrian Alps (Masch et al., 1985) while the first report of frictionite at the base of a landslide in a volcanic environment was described from the Arequipa volcanic landslide deposit in Peru (Legros et al., 2000). Furthermore, volcanoes tend to be basic in composition and silica layers are not expected to form in predominantly basic environment. ~~Neither clast-cortex aggregates nor silica layers are thought to have ever been reported from a volcanic setting.~~

Reconstruction of past volcanic~~o~~ failures in their source areas is extremely rare as there is usually no material to study and/or the main scarp has since been covered by younger eruptions. For that reason, the majority of studies have focused on the sedimentological properties of these failures (e.g. Hunt et al., 2013). Until recently ~~years~~, it has been assumed that the volcanic flank collapses occur as one major event that displaces hundreds of cubic kilometres of rock. However, new research suggests that at least some of these collapses occurred in multiple stages (Hunt et al., 2013, 2018; León et al., 2017). Such findings may have serious implications for the calculated frequency of such hazards and reopens questions about the possible reactivation of apparently inactive structures. The San Andrés Landslide on El Hierro in the Canary Islands represents one of the few places in the world where it is possible to investigate the ~~landslide mass and~~ fault planes and landslide mass of a volcanic collapse structure. This study integrates a range of structural geological and geomorphological measurements, petrological and microstructural analyses, and cosmogenic nuclide dating in order to reconstruct the developmental history of this huge ~~gravitational~~ slope failure. ~~Measurements~~ Data have been obtained - directly or indirectly - from the surface of the fault plane while samples were collected from both

the fault plane itself and an adjacent gully perpendicular to the footwall. Our hypothesis states that this landslide is not the result of a single event, as proposed by Day et al. (1997), but instead results from a number of successive events spanning a protracted period. This hypothesis is not straightforward to address as unambiguous evidence for multiple slip events along a single fault is difficult to elucidate due to problems associated with overprinting and weathering. Nonetheless, on the basis of previously published research and the results obtained during this study, it has been possible to propose a new ~~developmental~~ conceptual model ~~is proposed~~ for the development of the San Andrés Landslide~~, which is based on previously published research and the results obtained during this study.~~

2. Geological setting

2.1 *The island of El Hierro*

El Hierro is an active volcanic edifice that constitutes the smallest and youngest of the Canary Islands (Figure 1). Its oldest subaerially exposed rocks are represented by the Tiñor Unit, with a maximum age of 1.12 Ma (Guillou et al., 1996), which form the northern and northeastern parts of the island. This unit is thought to have developed rapidly until around the time of the Tiñor debris avalanche at 0.88 Ma (Carracedo et al., 2001). Thereafter, the rocks of the El Golfo-Las Playas Unit, with a maximum age of 0.55 Ma (Guillou et al., 1996), capped much of the Tiñor Unit and infilled the scarp area of the Tiñor debris avalanche (Carracedo et al., 2001). Its~~The~~ youngest subaerially exposed rocks are represented by the Rift Series, with ~~hich has~~ a maximum age of 0.16 Ma (Guillou et al., 1996). Over the past 33 000 years onshore eruptions have reoccurred approximately once every 1 000 years (Becerril et al., 2016a). The ~~most recent~~latest, ongoing~~,~~ phase of volcanism began around 2.5 ka (Carracedo et al., 2001). ~~Latterly a~~Recently a period of intense seismic activity ~~commenced~~ spanned from~~in~~ July 2011 (López et al., 2012) to 2014 (Benito-Saz et al., 2017). During this period ~~, prior to~~ an offshore eruption started~~that began~~ on 10 October 2011 and finished~~ended~~ in March 2012 (Meletlidis et al., 2015). ~~, and lasted until 2014 (Benito-Saz et al., 2017).~~ A more detailed description of the geology of island has recently been presented elsewhere (Carracedo and Troll, 2016).~~Blahůt et al., 2018a).~~

The flanks of El Hierro have hosted a number of enormous gravitational slope failures which have contributed to the development of its characteristic ~~three point~~three-point star morphology (Figure 1). Until now, seven debris avalanches have been identified: Tiñor (< 880 ka), Las Playas I (545-176 ka), Las Playas II (176-145 ka), El

Julan (> 158 ka), El Golfo A (176-133 ka), El Golfo B (87-39 ka), and Punta del Norte ~~with (~~of unknown age~~)~~ (Masson, 1996; Urgeles et al., 1996, 1997; Carracedo et al., 1999, 2001; Masson et al., 2002; Longpré et al., 2011; Becerril et al., 2016b; Carracedo and Troll, 2016; León et al., 2017; Blahůt et al., ~~2018b~~2018a). The volumes of these debris avalanches vary between 50 km^3 and 234 km^3, which makes them average from the known volcanic slope failures (for additional morphometric characteristics, see Blahůt et al., 2019). In addition, a large slump, sensu Moscardelli and Wood (2008), or a deep seated gravitational slope deformation, sensu Sorriso-Valvo et al. (1999) or Agliardi et al. (2001), is located on the southeast flank of the volcanic edifice. This feature, the San Andrés Landslide, is defined by a group of pronounced faults which represent landslide detachment planes. While ~~i~~its volume has not been determined ~~however~~, the deformed toe is visible around 18 km off coast at a depth of more than 3 km (Becerril et al., 2016b). Similar features have been described from other volcanic islands including the Azores (Hildenbrand et al., 2012) and the Hawaiian Islands (Duffield, 1975). It has previously been proposed that the San Andrés Landslide is an anchored block associated with the debris avalanche Las Playas I (Day et al., 1997).

2.2 *San Andrés Landslide*

The San Andrés Landslide has developed in the volcanic rocks of the Tiñor Unit. This unit comprises three distinct subunits (Gómez Sainz de Aja et al., 2010): the basal subunit is represented by relatively thin, 20-40 cm, steeply dipping lava flows; the intermediate subunit, which forms the majority of the unit, is represented by thicker, up to 4 m, shallow dipping lava flows; while the ~~third~~ uppermost subunit is represented by emission vents with well-preserved craters and associated lavas. The broad arcuate~~,~~ and presumably listric~~,~~ fault system which defines the boundaries of the slope deformation to the northeast is terminated to the southwest by an escarpment associated with the giant debris avalanche Las Playas II. Previously the San Andrés Landslide has been interpreted as either an aborted collapse structure (Day et al., 1997) or a deep seated gravitational slope deformation (Klimeš et al., 2016).

It has been reasoned that the fault system must have developed at some point between 545 ka and about 261-176 ka (Day et al., 1997). If correct, this implies that the collapsed landslide mass has remained anchored during ~~all~~ each of the subsequent giant debris avalanches on El Hierro (Carracedo and Troll, 2016). Support for the notion of protracted inactivity is provided by the presence of younger lavas crossing the fault without

displacement and the presence of scree covering lava flows as old as 145 ka in the gully of Las Playas (Carracedo et al., 1997). However, recent research is starting to challenge these arguments. The step-like structure of the incised gullies in the collapsed mass, together with records of progressive creep along its main detachment plane, in the order of 0.5 mm~~/.yr~~a^{-1}, suggests that the landslide mass may be moving steadily to the east and southeast (Klimeš et al., 2016; Blahůt et al., 2017, ~~2018a~~2018b).

The part of San Andrés Fault system investigated in this study is exposed along a narrow road which traverses the Barranco de Tiñor (27°47'18.82"N, 17°55'19.04"W). This outcrop is situated at c. 490 m asl, has a length of c. 70 m, and dips between 65° and 75° to the SE (Figure 2). The fault zone has a total thickness of between one and two metres. Both the footwall and hanging wall rocks comprise basaltic lavas of the Tiñor Unit with a few thin intercalated lapilli beds and soil horizons (Carracedo et al., 1997). No indurated breccia is present on the hanging wall. Its eastern section has only been uncovered relatively recently as a result of road construction and is distinguished by its whitish surface. This part of the fault surface hosts well-preserved slickenlines, which range in size from several millimetres to metre scale surface undulations. Detailed petrographic examinations of the fault rocks have been published previously (Day et al., 1997).

3. Methods

3.1 *Field ~~measurements~~ data and structural analyses*

Structural analyses of the surface of the San Andrés Fault plane incorporated structural geological field measurements alongside the interrogation of a high resolution digital terrain model (DTM). This DTM was constructed on the basis of photogrammetric imagery obtained from an unmanned aerial vehicle (UAV) ~~which was then~~and processed using the commercial software Agisoft PhotoScan (Agisoft LLC, 2014). The accuracy of terrain models constructed following this approach is directly comparable to those constructed on the basis of laser scanning (Balek and Blahůt, 2017). From the photogrammetric point cloud, it was possible to derive two complimentary slope gradient maps with grid cells of 2 x 2 cm. The first gives a ground plan view of the fault (Figure 3A) while the second gives a fault perpendicular view (Figure 3B). These maps have been analysed in detail using the ESRI® ArcGIS applications ArcMap and ArcScene. Slope gradient maps, in contrast to hillshade maps, are particularly suited for the identification of linear features irrespective of their spatial distribution and

orientations. The obtained data were then compared to the structural geological field measurements recorded on the outcrop.

Schmidt hammer sampling ~~can be~~is used in geomorphological research to estimate rates of weathering ~~or~~ and to obtain information relating to relative exposure ages for rock surfaces on the basis of rebound values, R (Aydin and Basu, 2005; Goudie, 2006). ~~In~~ A total of ~~eighty eight~~eighty-eight test sites were sampled on the fault plane using a Proceq SilverSchmidt ST-PC. Each site was sampled twelve times in a direction perpendicular to ~~the fault~~its surface. Of these twelve samples, the uppermost and lowermost values were disregarded, according to standard sampling protocol, and the remaining ten were used to calculate the rebound value. These R values were processed in a GIS. Initially, an orthophotograph of the fault scarp had to be created from a set of photoshots. The position of each test site was recorded on a printed copy of the orthophotograph prior to image rectification in the GIS. The relative positions of several test sites were measured in the field and used as reference points during georeferencing. Each test site is represented by a point placed approximately in its centre and then the calculated R value was added to each test site. Interpolation of these values indicates changes in the relative surface hardness across the exposed part of the fault scarp. Several interpolation algorithms were tested but the character of the data led us to select the natural neighbour technique.

3.2 *Petrographic and microstructural analyses*

Petrographic analyses of the sampled rocks were performed at the Institute of Rock Structure ~~&~~ and Mechanics CAS and the Institute of Geology CAS in Prague. Optical microscopy was conducted using the polarisation microscope Leica DMR while chemical analysis of the primary and accessory minerals was conducted~~ing~~ using the electron microprobe CAMECA SX-100. Microstructural investigations have been made through the application of optical microscopy, scanning electron microscopy (SEM), and energy dispersive spectroscopy (EDS). These investigations were made at the University of Vienna. Thin sections were cut perpendicular to the shear plane and parallel to the direction of sliding prior to mechanical polishing to thicknesses of c. 30 µm. ~~Selected samples were carbon coated for SEM.~~ Optical microscopy was conducted using the polarisation microscope Leica DM4500 P with micrographs obtained under both plane polarised light (PPL) and crossed polarised light (XPL). Selected samples were carbon coated for SEM. The SEM imagining ~~Scanning electron microscopy~~ was conducted using a ~~the SEM microscope~~ FEI Inspect S with an accelerating voltage of 10-15 kV

for spot sizes of 5-7. Images were obtained and presented in the back scattered mode (BSE). Element energy dispersive spectroscopy was also conducted to better understand the chemical effects of fault slip. The EDAX EDS systems were used as an add-on to the FEI Inspect S. ~~SEM.~~ Using the TEAM™ Software Suite and Smart Phase Mapping it was possible to collect spectra and generate phase maps showing elemental distribution and associated spectra. The EDS operating conditions were 15 kV accelerating voltage for spot size of 5, at resolution of 514 x 514, dwell 200 µs.

3.3 *Cosmogenic radionuclide dating*

Cosmogenic radionuclide dating constrains the amount of time a rock has been situated at or near the surface of the Earth (e.g. Lal, 1991). Normal fault planes represent ideal objects for this dating technique as the incoming cosmic rays are only able to penetrate the progressively exposed parts of the fault (e.g. Palumbo et al., 2004). The basaltic lithologies of El Hierro determine that the most suitable cosmogenic nuclide with which to constrain periods of fault activity is ^{3}He (e.g. Kurz, 1986; Poujol et al., 2014). The sampling strategy aimed, first, to obtain samples from the least eroded parts of the fault and, second, to avoid obtaining samples from the whitish part of the fault plane as this was known to have been exposed during road construction. Five samples were collected from two profiles along the footwall (Figure 2). These samples range in thickness from two to five centimetres and belong to the same basaltic sequence ~~which~~ that erupted 1.05±0.02 Ma (Carracedo et al., 2001). Samples were crushed and sieved to isolate fractions of less than 0.25 mm, 0.25-0.5 mm, and 0.5-2.0 mm. ~~0.2 mm to 2 mm and 0.25 mm to 0.5 mm.~~ Several physical separation techniques including magnetic separation and density separation were used to isolate pure olivine and pyroxene phenocrysts.

All helium analyses were performed in the noble gas platform of the Centre de Recherches Pétrographiques et Géochimiques in Nancy. Samples were fused *in vacuo* at 1600°C for 15 minutes using the new custom designed metal induction furnace of CRPG (Zimmermann et al., 2018). Typical furnace blanks were $(1.9\pm0.6) \times 10^{-19}$ and $(5\pm4) \times 10^{-15}$ mol.g^{-1} for ^{3}He and ^{4}He, respectively, which ~~. This~~ represented an average of 1 % and 0.1 % of the ^{3}He and ^{4}He concentrations measured in the samples, respectively. The~~n the~~ extracted gas then underwent standard gas purification (Blard et al., 2015). Helium was cryofucused at 8K before being released at 70K and introduced into the Split Flight Tube mass spectrometer, a Nier source static mass spectrometer optimised for the analysis of cosmogenic nuclides (Protin et al., 2016). The linearity of the mass spectrometer was carefully

established by analysing standard splits with similar ^{4}He pressure to those of the samples. During the ~~one month~~one-month analytical period the observed reproducibility of the system was 2 % at 1σ, ~~both~~ for both ^{3}He and ^{4}He. Furthermore, during this ~~one month~~one-month period, two CRONUS-P pyroxene standards were analysed. These yielded ^{3}He concentrations of $(4.86\pm0.14) \times 10^{9}$ at.g^{-1} and $(5.01\pm0.14) \times 10^{9}$ at.g^{-1}. Both values stand within the internationally recognised error limits for this material (Blard et al., 2015). To determine the $^{3}He/^{4}He$ ratio of the magmatic component step crushing *in vacuo* was conducted on 0.5 mm to 2 mm olivines and pyroxenes obtained from Sample 5III (1^{st} step: 100 strokes, 1 min; 2^{nd} step: 500 strokes, 5 mins;~~)~~ ~~(~~ Table 1). Crushing blanks were $(3\pm2) \times 10^{4}$ and $(7\pm2) \times 10^{9}$ for ^{3}He and ^{4}He, respectively. This represented 1 % and 4 % of the ^{3}He and ^{4}He analysed during the second crushing step.

To determine cosmogenic ^{3}He concentrations it was necessary to correct the melted ^{3}He concentrations ($^{3}He_{melt}$) from the nucleogenic ($^{3}He_{nucleo}$) and the magmatic ($^{3}He_{mag}$) components:

$$^{3}He_{cos} = {}^{3}He_{melt} - {}^{3}He_{nucleo} - {}^{3}He_{mag}$$

With:

$$^{3}He_{nucleo} = P_{3nuc} \times T_{eruption,}$$

P_{3nuc} is the production rate of nucleogenic ^{3}He. In this study, a value of 6×10^{-3} at.g^{-1}.a^{-1} has been used, computed using the equations of Andrews (1985) and the chemical composition measured in the phenocrysts and bulk rock samples (Supp. Table A). Combined with a value of 1.05±0.02 Ma for $T_{eruption}$~~, (~~based on the K-Ar age of the San Andrés basalt presented in Carracedo et al. (2001)~~)~~, this yielded a value of $(6\pm3) \times 10^{3}$ at.g^{-1} for $^{3}He_{nucleo}$.

In theory, the magmatic ^{3}He component has to be computed following this equation from Blard and Farley (2008):

$$^{3}He_{mag} = (^{4}He_{melt} - {}^{4}He_{rad}) \times (^{3}He/^{4}He)_{crush}$$

306

307 With

308

309 $^{4}He_{rad} = P_{4rad} \times T_{eruption,}$

310

311 P_{4rad} being the radiogenic ^{4}He production rate in the analysed olivines and pyroxenes. P_{4rad} is computed using
312 the equations of Blard and Farley (2008) and the U, Th, and Sm concentrations measured in samples COS4-I and
313 COS5-II (Supp. Table A). Using the 1.05±0.02 Ma value for $T_{eruption}$, this yields $^{4}He_{rad}$ theoretical concentrations
314 ranging from 1.2×10^{12} at.g^{-1} to 4.1×10^{12} at.g^{-1}.

315

316 Such $^{4}He_{radio}$ concentrations are similar to the total ^{4}He concentrations measured by fusing the samples, which
317 range from 6.2×10^{12} at.g^{-1} to 1.36×10^{13} at.g^{-1}, for an average of $(3.3\pm4.6)\times10^{12}$ at.g^{-1}.

318

319 Thus the outlined approach for estimating $^{4}He_{rad}$ represents the main source of uncertainty when computing
320 the magmatic ^{3}He correction and, in turn, the main source of uncertainty when computing the final cosmogenic
321 ^{3}He concentrations.

322

323 Instead, we decided to apply the following approach and compute a minimal and a maximal value for the
324 cosmogenic ^{3}He concentrations, as follow (Table 1):

325

326 $^{3}He_{cos\ min} = {}^{3}He_{cos\ min} - {}^{3}He_{nucleo} - {}^{3}He_{crush\ mag,}$

327

328 assuming that $^{3}He_{crush\ mag}$ is the magmatic ^{3}He concentration from the prolonged crushing $(4.3\pm2.0)\times 10^{6}$ at.g^{-1}

329

330 $^{3}He_{cos\ max} = {}^{3}He_{cos\ min} - {}^{3}He_{nucleo}$

331

332 $^{3}He_{cos\ min}$ concentrations range from less than 2×10^{6} at.g^{-1} to $(1.19\pm0.20) \times 10^{7}$ at.g^{-1} while $^{3}He_{cos\ max}$ range from
333 $(2.22\pm2.04) \times 10^{6}$ at.g^{-1} to $(2.17\pm0.21) \times 10^{7}$ at.g^{-1}.

334

Finally, $^{3}He_{cos}$ exposure ages were computed using the CREp calculator (crep.crpg.cnrs-nancy.fr), with the world averaged ^{3}He production rate, the standard atmosphere, and the Lal-Stone time dependent model (Martin et al., 2017). The production rate was computed taking into account the spatial characteristic of the samples, including self-shielding (Table 1).

4. Results

4.1 *Field ~~measurements~~ data and structural analyses*

The NE section of the San Andrés Fault outcrop is morphologically well preserved while its SW section has been smoothed as a result of weathering and incurred~~received~~ some damage during road construction. In general, the exposed fault plane is straight with an orientation of approximately 170/70° (dip direction/dip angle). Only some irregularities can be observed such as two remarkable fault plane undulations protruding from ~~the fault~~its surface, with widths of up 4 m, separated by a parallel depression (Figure 3A-B). These irregularities were also recognised ~~identified~~ during structural geological measurements. In greater detail, it has been possible to identify numerous linear features, which have been grouped into three families on the basis of their character and orientation (Figure 3A-C). First, a family of centimetre to metre scale striations were identified on the basis of structural measurements and from the slope gradient maps. These striations cover most of the outcrop but are best preserved on the fault plane undulations. Most commonly, the striations ~~have~~ plunge with ~~directions of~~ azimuths of 125° and 131°. Second, a family of smooth elongated undulations and strongly elongated protrusions~~bumps~~ were also identified on the basis of structural measurements and from the slope gradient maps. These features are best seen in the ~~depressions and flats in the~~ northeastern section of the fault plane. The undulations and ~~bumps~~ protrusions ~~have a~~ plunge ~~direction of~~with an azimuth of 111°. Third, a family of very smooth, spatially limited, slightly elongated ~~bumps~~ protrusions were identified from the fault perpendicular slope gradient map. These are found in the lower SW and upper NE part of the 4 m wide fault plane undulation as well as at the crest of the other undulation protruding from surface to the NE. The ~~bumps~~ protrusions~~have a~~ plunge with~~direction of~~ an azimuth of 158°.

A photomosaic offering a perpendicular view of the fault outcrop ~~in the background photomosaic~~ overlain by a raster of interpolated R values is presented on Figure 4. Proportional plots ~~have been used to~~ illustrate the spatial variability in rock hardness across the outcrop. In general, higher R values have been measured on the

lower and right side of the fault outcrop than have been measured on its upper and left side. ~~However, notably low R values have been recorded in a wedge-shaped zone between 23 m and 26 m (R < 25), in an area where a rather soft gouge material is attached to the fault surface. However, as the vegetation cover descends much lower here than elsewhere, it is suggested that chemical and biological weathering processes are more intense hereabouts.~~ The highest R values, indicating the least weathering, have been recorded in the lowermost part of the fault outcrop on its right side (R > 50). This finding is not surprising given that the hard whitish surface was exposed only recently during ~~road~~ construction of the road. ~~In addition, high~~High R values have also been recorded on the far left side of the fault outcrop (R > 40). This finding is more surprising but it can be explained by several tens of centimetres of erosion on the fault surface and the presence of harder basalt blocks within the tectonic breccia. Conspicuously low R values have been recorded in a wedge-shaped zone between 23 m and 26 m (R < 25). Here a rather soft gouge material is attached to the fault surface and the vegetation cover descends much lower than elsewhere – this suggests that chemical and biological weathering processes are more intense in this area.

4.2 *Petrographic analyses*

The host rock basanites are ~~composed of~~ fine grained basic ~~volcanic~~ rocks (samples PET3 and PET4). These rocks contain ~~are~~ mainly pyroxene, plagioclase, olivine~~,~~ ~~and~~ amphibole and volcanic glass, together with the accessory minerals (apatite, chromite, magnetite, and Ti-magnetite). The pyroxene is represented by ~~mainly comprises the monoclinic mineral~~ diopside. T~~e while t~~he plagioclases are usually~~tends to be~~ zoned~~al~~ with a~~n~~ basic core (An_{79-83} ~~acid rim~~) and acid rim (~~,~~An_{45-70})~~, and a basic core, An_{79-83}~~. Olivine occurs only in basanites with subordinate amounts of volcanic glass. The olivine is enriched by ~~has a predominant~~ forsterite component~~,~~ (75-80 mol. %)~~,~~ T ~~while t~~he amphibole is represented by~~spans from~~ magnesiohornblende to hornblende tschermakite. ~~A high amount of volcanic glass is present while basanites with subordinate amounts of volcanic glass contain frequent phenocrysts of olivine.~~ The texture of the groundmass is mostly ophitic and gives no indication of a pre-existing preferred fabric orientation. The tectonic breccias sampled from the fault plane are composed ~~byof~~of fragments of volcanic rock (up to several centimetres), cemented by a very fine grained groundmass containing abundant fragments of the original volcanic rock (millimetres to centimetres on samples~~) (~~ PET1 and PET2). The higher proportion of fine grained Fe-oxides and Fe-hydroxides imparts a rusty colour of these tectonic breccias~~to the rock~~. However, the volume of Fe-oxides and Fe-hydroxides is highly

variable, with significant enrichment in the fine grained groundmass of the original volcanic rock. The tectonic breccias ~~host cracks of highly variable orientation and sizes, filled,~~are cross-cut ~~filled~~ by zeolite veins ~~that exhibits~~in a range of orientations and sizes. Frictionite, or landslide pseudotachylyte, was found in samples obtained directly from the fault plane (Figure 2). This~~It~~ is composed of relict frictional melt and material similar to tectonic breccia (Figures 5-7).

4.3 *Microstructural analyses*

The NE part of the fault outcrop is covered by a whitish layer which attains a maximum thickness in the order of several centimetres. Figure 2 shows examples of the ~~This~~ whitish layer that ~~usually~~ overlies the grey~~ish~~ cataclasite and microbreccias. ~~, and i~~In some cases~~ but it sometimes~~ this whitish layer comes into direct contact with tectonic breccia. The tectonic breccia is highly oxidised (Figure 2D, F). Brecciation intensity increases from the undeformed basanite to the more deformed breccia, i.e. towards the fault surface. This~~ This The tectonic~~ breccia ~~marks the transition from undeformed basanite, at greater depths, to more deformed breccia, at the fault surface. The breccia, and is highly oxidised (Figure 2D, F). It has not been analysed further but~~and it may be ~~a~~ the product of an earlier slip event. However, ~~In this study,~~ here we focus on the cataclasite and the whitish layer, i.e. ~~Instead attention focuses here on the~~ those layers that overlie the tectonic breccia. ~~On the basis of~~ Using optical microscopy it is possible to differentiate two distinct layers within the frictionite by their composition and microstructure: a structurally lower cataclasite and a structurally higher silica layer.

The cataclasite cuts the tectonic breccia while in places it is cut by the silica layer. Contact with the host rock is characterised by a sharp boundary that is observed in both hand samples and optical micrographs (Figure 6). Although the cataclasite is grey in hand samples, it is dark brown in optical micrographs (Figure 6~~A,B~~A, B) while the sharpness of the contact is accentuated by the truncation of several clasts (Figures 6 & 7). The main characteristics of this layer are grain size reduction and P- foliation, ~~(according to~~ terminology of~~after~~ Passchier and Trouw, ~~(~~2005)~~)~~. The zones of grain size reduction, in which grain sizes range from c. 10 µm to c. 100 µm, are defined by P- and Y- shears (Figure 6~~B,D~~B, D). A dextral sense of shear is indicated by the P- and Y- shears along with a winged inclusion visible in the optical micrographs (Figure 6~~A,B~~A, B). This finding is consistent with structural observations made at the outcrop scale. Elemental maps highlight the similarity between the composition of the host rock and the composition of the cataclasite (Figure 6~~E,F~~E, F). Moreover, this similarity

is accentuated by the apparent resemblance in composition of a truncated clast, itself in contact with the cataclasite (Figure 6~~E,F~~E, F). A second cataclasite has a more lensoid shape which is apparently defined by P- and Y- shears (Figure 7). It exhibits strong P-foliation which is seen most readily in the elemental maps (Figure 7~~C,E~~C, E). ~~Interestingly,~~ In addition, cracks ~~are~~within this layer are parallel to both the Y-shear~~ing~~, and ~~to~~ the slip surface, and are filled with silica ~~gel~~ (Figure 7E).

The silica layer cuts both the tectonic breccia and the cataclastic layer. The boundary between the silica layer and the subjacent rocks is a sharp, single line, which crosscuts foliation in the cataclasite and truncates clasts in the tectonic breccia. The boundary between the cataclasite layer and the silica layer is sometimes marked by shiny sublayers that parallel the boundary (Figure 6~~B,H~~B, H) and exhibit a high interference colour when seen under cross polarised light with a gypsum tint plate (Figure 5C). There is no indication of mixing between the cataclasite and the silica layer across the boundary ~~between~~ separating these layers. The silica layer appears to be translucent, white to pale coloured under plane polarised light (Figures 5-7). It is composed of a microcrystalline to amorphous silica matrix with a thickness of c. 250 µm to 350 µm. The architecture varies: the matrix consists of an inclusionless silica material that develops into complex structures with flow bands (Figures 5-7), cataclastic sublayers (Figure 5H), and clast-cortex aggregates (Figure 6~~G,I~~G, I). Flow bands, which vary in thickness from c. 25 µm to c. 110 µm, correspond to P- and Y- shears in the cataclastic layer fabric and are characterised by a change in the amount of Mg (Figure 5L and Figure 6~~C,D~~C, D). Cataclasite sublayers form lenticular shapes (Figure 5H). These sublayers appear to have a similar composition to the cataclasite layer but with a finer grain size and present evidence of material mixing with the silica layer. Some clasts embedded in the silica layer have a cortex, or armour, and these are referred to as clast-cortex aggregates. The clast-cortex aggregates vary in size, from c. 90 µm to 290 µm, complexity, and composition. Those clasts within the aggregates consist of fragments of adjacent rock (Figure 7G) or silica matrix (Figure 6I). A complex cortex texture with what appears to be several coatings has been observed (Figure 6G). Elemental maps show that the cortex composition varies as well (e.g. Figure 6L and Figure 7~~D,E~~D, E). It is believed that a significant amount of the cortex material was lost during preparation of the thin sections (e.g. Figure 6G-I).

4.4 *Cosmogenic radionuclide dating*

Cosmogenic ^{3}He exposure ages reveal significant differences between each of the two sampled profiles. Sample COS1 has yielded a maximum exposure age of 21±20 ka while samples COS2 and COS3 have yielded a maximum exposure age of 26±18 ka. Replicates of sample COS4 yielded exposure ages ranging from 21±19 to 61±19 ka while replicates of sample COS5 yielded exposure ages ranging from 52±17 to 183±17 ka (Table 1).

~~The older exposure ages obtained from the left hand profile may simply reflect more recent exhumation or more intensive erosion on the right hand part of the fault.~~ These results indicate that movement across the currently exposed portion of the fault plane occurred over a short period of time as suggested by the fact that there is no gradual decrease in exposure ages from upper to lower part of the two profiles.

The right hand profile (samples COS1-3) revealed exposures ages that are below the detection limit i.e. these were exposed between 0 and 26 ka. These young exposure ages most probably reflect recent exhumation on the right hand part of the fault owing to the fact that the right hand profile is separated from the left hand profile by only 6-7 m. Intense erosion of the right hand profile can be excluded as the R values indicate much greater hardness, i.e. less weathering, here than on the left hand profile.

The left hand profile (samples COS4 and COS5) revealed exposure ages between 21 and 183 ka. The higher sample COS4 provides a younger age than the lower sample COS5. Under normal circumstances this should not be possible – the highest parts of the fault should be exposed before its lower parts – and it suggests that the higher sample has been subjected to weathering. Consequently sample COS5 offers the most reliable results as it has neither been affected by weathering nor by recent exhumation. The high variability of computed exposure ages between the replicate in the~~i~~s sample is due to the considerable uncertainty associated with the estimate of the magmatic ^{3}He component as outlined in Section 3.3. Nonetheless it is believed that the most recent fault reactivation occurred between the calculated exposure ages of sample COS5 (52±17 to 183±17 ka).

5. Interpretation and discussion

5.1 *Landslide displacement direction*

Distinct families of linear and elongated features ~~on~~ at the fault plane evidence past behaviour of the rock mass (Sagy et al., 2007). Two major slip events are interpreted to have occurred on the studied fault plane ~~On~~ on the basis of the relative position and general morphology of such~~its linear and elongated~~ features~~, two major slip~~

~~events are interpreted to have occurred on the studied fault plane~~. The older phase is represented by the family of smooth elongated undulations and strongly elongated bumps, best preserved in the depressions and flats in the northeastern section of the fault plane, which have a plunge direction of 111°. During this phase the rock mass moved towards the ESE. The younger phase is represented by the other two families of linear and elongated features. The onset of this phase is interpreted to have commenced with minor, most probably slow~~,~~ displacement towards the SSE. Support for this ~~slow displacement~~ is gleaned from the smooth, spatially limited, elongated bumps which have a plunge direction of 158°. The displacement rate ~~of displacement~~ is then interpreted to have accelerated as the rock mass moved more towards the SE. Support for this is gleaned from the centimetre to metre scale striations which cover most of the fault outcrop and have plunge directions of 125° and 131°. The general appearance of these ~~linear and elongated~~ features is sufficiently similar to assume that they developed during a single slip phase. It is supposed that ~~the~~ this shift in the displacement direction, from the SSE to the SE, can be explained by either a sudden change in the geometry of the slip surface or a fundamental change in the morphology of the entire volcanic edifice. It is known that El Hierro underwent a clockwise rotation of 15°, beginning ~~at~~ around 440 ka (Széréméta et al., 1999), and it has been suggested that this rotation could be associated with~~relate to~~ activity on the San Andrés Landslide and the debris avalanche Las Playas I (Carracedo, 2008).

5.2 *Fault related microstructures and dynamic rock reworking*

~~It is contended that t~~The microstructures seen ~~at~~ on the surface of the San Andrés Fault are believed to be a result of fast slip, associated with ~~from~~ frictional heating and partial melting during landslide emplacement. ~~and, therefore, this rock is a frictionite (or landslide pseudotachylyite).~~ The first line of evidence for flash heating during flank collapse is observed in ~~comes from~~ both hand samples and polished slabs as ~~energy is seen to have~~heat diffused in the underlying material: ~~. T~~the adjacent host rock and tectonic breccia exhibits increasing level of ~~are only~~ oxidisation~~ed when in immediate contact with the frictionite~~towards the fault surface. This is similar for pseudotachylyites reported from the Köfels landslide (Masch et al., 1985) and from the Arequipa volcanic landslide deposit in Peru (Legros et al., 2000). The second line of evidence comes from the crosscutting relationships between either the host rock or the tectonic breccia and the deformation layers. All of the observed contacts are sharp and accentuated by multiple truncated clasts. This type of crosscutting relationship indicates fast displacement and is often considered a strong indication of a seismic slip (Passchier

and Trouw, 2005; Price et al., 2012; Smeraglia et al., 2017). The third line of evidence comes from the boundary between the silica layer and the adjacent rocks. This boundary is characterised by~~, which has~~ shiny bands that~~,~~ exhibit~~ing~~ a high interference colour under cross polarised light and a positive optical sign under cross polarised light using a gypsum tint plate. These bands are tentatively interpreted as recrystallised material resulting from frictional melting but further analyses are needed ~~in order~~ to confirm this supposition.

The cataclastic layer exhibits P-foliation, grain size reduction, and the development of winged clasts in a heterogeneous matrix. The winged clast presented in Figure 5 resembles those of Grasemann ~~&~~ and Dabrowski (2015) and Grasemann et al. (2019). The foliation developed within this layer is typical of brittle deformation, with ~~horizontal~~ Y- shears~~,~~ parallel to the slip surface, and ~~inclined~~ P-shears inclined relative to the slip surface (i.e. Figure 5l). This type of foliation cannot be used as an indicator for fast slip as it is recorded in association with both seismic and creep phenomena (Verberne et al., 2013; Smeraglia et al., 2017). However, unequivocal evidence for fast slip, instead of~~rather than~~ progressive creep, is provided by the fact that the contact between the cataclastic layer and the adjacent rock is sharp and accentuated by multiple truncated clasts. The cataclasite architecture is similar to those described in other volcanic pseudotachyl~~y~~ites (Lavallée et al., 2012, 2014; Kendrick et al., 2012, 2014) as well as to that described ~~for~~ in seismically deformed limestones (Smith et al., 2011). Therefore, it is necessary to define this cataclastic layer as frictionite *sensu lato*, as it was ~~probably~~ almost certainly emplaced during catastrophic landslide emplacement but there is no decisive proof of flash heating.

In contrast, the silica layer is defined as frictionite *sensu stricto*, ~~due to the fact that~~ as it is comparable to traditional pseudotachyl~~y~~ites (e.g. Passchier and Trouw, 2005; Price et al., 2012; Rowe and Griffith, 2015)~~.~~~~)~~. ~~Identification criteria of deformed pseudotachylytes are presented elsewhere (e.g.; Passchier and Trouw, 2005; Price et al., 2012). For example, Nonetheless the following the identification criteria of deformed pseudotachylytes (Passchier and Trouw, 2005; Price et al., 2012) we list features~~are Here a list of particularly pertinent features is presented with reference to the identification criteria for deformed pseudotachylytes (Passchier and Trouw, 2005; Price et al., 2012)~~in the context of this study.~~ :

i. ~~(i) crosscutting~~ *Crosscutting relationships with sharp layer boundaries.* The silica layer cuts the cataclasite foliation and the boundaries are accentuated by clast truncation and presence of shiny bands which have been interpreted as recrystallised material from frictional melting. Analogous microstructural features have been reported from numerous natural and experimental cases of seismic slip (e.g. Fondriest et al., 2013; Smeraglia et al., 2017; Tesei et al., 2017).

ii. ~~Second, the~~ *The presence of fragments of host rock.* Fragments of adjacent rock appear as isolated islands and vary in size, shape, and complexity. The more complex clasts have an encasing cortex, or armour, and are referred to as clast-cortex aggregates. Typically, those fragments described here have a volcanic clast in the core, cataclastic material in the rim, and they parallel the foliation. In a number of senses, they are similar to "armoured clasts" or "accretionary rounded grains" (Anders et al., 2010; Rowe et al., 2012; Kirkpatrick et al., 2013) and clay-clast aggregates (Boutareaud et al., 2008; Han et al., 2011). The main differences are the ratio between the clast and the rim and their composition. The rims described here appear to be wider than previously reported while they are neither composed of clay nor any other mineral assemblage. Consequently, the clast-cortex aggregates presented~~described here~~ in this study are most readily comparable to the accretionary rounded grains described from the Corona Heights Fault (Kirkpatrick et al., 2013).

iii. ~~Third, the~~ *The presence of an ultra-fine grained matrix.* The silica layer comprises a homogenous silica matrix, ultra-fine grained to amorphous, which is very similar to silica gel (Kirkpatrick et al., 2013; Faber et al., 2014) and amorphous nanopowder (Rowe et al., 2019). More detailed studies are needed in order to measure the amount of water and crystalline material that occurs in this matrix. The presence of new grains that have grown in the voids or bubbles ~~suggests~~ indicates that at least some of this matrix must be crystalline.

iv. ~~Fourth, i~~*Inherited compositional variations from flow structures.* Flow bands in the silica layer are defined by optical and compositional variations. Optical variations are evident as shiny bands and they can be traced along the whole length of the layer. ~~More detailed analyses are needed to fully~~

Formatted: Font: Not Italic
Formatted: Font: Italic
Formatted: Font: Italic
Formatted: List Paragraph, Numbered + Level: 1 + Numbering Style: i, ii, iii, … + Start at: 1 + Alignment: Left + Aligned at: 0.63 cm + Indent at: 1.9 cm
Formatted: List Paragraph, Numbered + Level: 1 + Numbering Style: i, ii, iii, … + Start at: 1 + Alignment: Left + Aligned at: 0.63 cm + Indent at: 1.9 cm
Formatted: Font: Italic
Formatted: Font: Italic
Formatted: List Paragraph, Numbered + Level: 1 + Numbering Style: i, ii, iii, … + Start at: 1 + Alignment: Left + Aligned at: 0.63 cm + Indent at: 1.9 cm

~~understand their origin.~~ The flow bands are structurally controlled, as they parallel the P- and Y-shears, and they localise clasts and clast-cortex aggregates as well as Mg-enriched material. Further analyses are needed to fully understand their origin. Similar to these flow bands are the cataclastic sublayers, which are also structurally controlled, but with evidence for the reworking of cataclastic material. This feature, together with presence of clast-cortex aggregates is~~, can be~~ interpreted as fluidised granular flow ~~which has been~~ reported in many geologic settings (Boutareaud et al., 2008; Anders et al., 2010; Ujiie et al., 2011; Kirkpatrick et al., 2013). Furthermore, fluidised cataclasites have been suggested as a record of seismic slip rates (Brodsky et al., 2009; Rowe et al., 2005).

~~i.~~v. ~~Fifth, differences~~ *Differences between the matrix and host rock mineral assemblages.* The most conspicuous difference between the silica layer and the adjacent rocks is in the mineral assemblage. The homogenous silica layer contrasts greatly with the polymineralic cataclasite and the host rock. Even though the silica layer can be assumed to be a product of hydrothermal fluid deposition, the presence of kinematic indicators such as shears and flow bands consistent with observations at the outcrop scale, indicate that the silica layer was formed as a product of frictional slip. Silica has been reproduced in fast slip experiments (e.g. Di Toro et al., 2011; Kirkpatrick et al., 2013; Rowe et al., 2019) and ~~. It~~ is considered to be a product of frictional wear that~~which~~ weakens the fault~~, due to the fact that it~~ acting~~s~~ as a lubricant (Rowe et al., 2019).

5.3 ~~*Developmental*~~ *Conceptual model for the San Andrés Landslide*

A conceptual~~developmental~~ model for the development of the San Andrés Landslide is proposed here on the basis of the findings presented in this study and age estimates presented elsewhere in the published literature (Figure 8). The first slip event as evidenced by the cataclastic layer is proposed to have occurred between 545 ka and 430 ka. The lower limit for fault activity is defined by the onset of volcanism associated with the El Golfo Series (Guillou et al., 1996) while the upper limit for fault activity is defined by the onset of the clockwise rotation of El Hierro (Széréméta et al., ~~1997~~1999). The second slip event as evidenced by the silica layer is proposed to have occurred between 183 ± 17 and 52 ± 17 ka based on the presented cosmogenic ^{3}He exposure dates. This age range spans termination of volcanism associated with the El Golfo-Las Playas Unit and the onset

of volcanism associated with the Rift Series at 145 ka (Guillou et al., 1996). The lower limit for fault activity broadly relates to the probable timing of the debris avalanches El Golfo A, between 176 ka and 133 ka, and Las Playas II, between 176 ka and 145 ka. Moreover, the upper limit for fault activity broadly relates to the probable timing of the debris avalanche El Golfo B, between 87 ka and 39 ka. ~~One of these giant debris avalanches, accompanied by strong ground shaking,~~ Thus, it is believed that the factor, or factors, which triggered one of these giant debris avalanches may have triggered the second slip event described in this study~~here~~ but ~~,~~ no other data have yet been found to support this hypothesis. In addition, a conceptual model is presented for the development of the surface of the San Andrés Fault (Figure 9). The developmental model outlined here is broadly consistent with the findings of Day et al. (1997). In that study, it was suggested that the minimum age of the San Andrés Fault should be between 250 ka and 150 ka and that the fault could ~~only~~ have been active only for a geologically short period of less than 400 ka. Their ~~findings~~ assertions are based on a younger undisturbed lava flow which covers the southern part of the fault.

6. Conclusions

In this study~~The~~ the fault plane of the San Andrés Landslide on El Hierro in the Canary Islands has been investigated ~~in this study~~ through a combination of geological and geomorphological measurements, petrological and mineralogical analyses, and cosmogenic ^{3}He exposure dating.

- The ~~steeply dipping~~ fault surface is composed of a striated frictionite~~, with a thickness of up to 5 cm,~~ which is in contact with a highly oxidised tectonic breccia~~, with a thickness of up to 1.5 m~~. The tectonic breccia transitions into the underlying undeformed basanite host rock. Microstructural analysis of the frictionite has revealed two distinct layers: a dark heterogeneous cataclastic layer and a translucent silica layer with a thickness of up to 1 cm.
- The architecture of the samples and the observed crosscutting relationships ~~between the layers and adjacent host rock~~ suggest that the cataclasite layer and the silica layer represent two separate slip events associated with seismic rupture during landslide emplacement. ~~The older cataclastic layer cuts the tectonic breccia and presents evidence for P-fabrics and grain size reduction. The younger silica layer cuts the tectonic breccia and the cataclasite and preserves clast-cortex aggregates, flow bands, and reworked cataclastic material in an ultra-fine grained to amorphous matrix.~~ Moreover, the notion

of ~~These~~ two distinct slip phases is supported by ~~are in accordance with the~~ kinematic markers etched on the fault surface.

- This~~Coupling this~~ information – coupled with the cosmogenic ^{3}~~He~~ exposure ~~ages~~ dating and ~~current~~ knowledge about the geological history of the island – forms basis of a conceptual model for the development ~~of the fault surface, it has been possible to propose a development model for~~ of the San Andrés Landslide. The first slip event, represented ~~as evidenced~~ by the cataclastic layer, is ~~proposed~~ thought to have occurred between 545 ka and 430 ka while the second slip event, represented ~~as evidenced~~ by the silica layer, is thought ~~proposed~~ to have occurred between 183 ± 17 and 52 ± 17 ka. ~~based on the presented cosmogenic ^{3}He exposure dates.~~

This is the first time that more than one slip event has ever been recognised on a single fault plane resulting from volcanic flank collapse on an oceanic island. It suggests that the possibility of reactivating supposedly inactive fault structures may be far greater than hitherto assumed. This is a key finding, which may lead to re-evaluation of the threats related to volcanic islands collapses. Furthermore, it is believed that this is the first time a silica layer resulting from frictional melt has been described from a volcanic setting. ~~from the fault plane of the San Andrés Landslide. It is also believed to be the first time a silica layer resulting from frictional melt has been described in a volcanic setting.~~

Acknowledgements

Bernhard Grasemann, Rostislav Melichar, ~~Bernhard Grasemann,~~ Gerlinde Habler, and Jackie Kendrick are thanked for stimulating and insightful discussions regarding ~~the obtained~~our results and their interpretation. We are also grateful to the two reviewers and the editor for significantly improving the clarity of this manuscript.

Funding sources

This study was supported by the Czech Science Foundation [Project GJ16-12227Y], by the OP VVV project CzechGeo EPOS-Sci No. CZ.02.1.01/0.0/0.0 /16_013 /0001800 and the conceptual development research organisation of the Institute of Rock Structure & and Mechanics CAS [RVO:67985891].

References

Agisoft LLC, 2014. Agisoft PhotoScan User Manual, Professional Edition, Version 1.1. Agisoft LLC, St. Petersburg, 78 pp.

Agliardi, F., Crosta, G., Zanchi, A., 2001. Structural constraints on deep seated slope deformation kinematics. Engineering Geology 59, 83-102. https://doi.org/10.1016/S0013-7952(00)00066-1

Ancochea, E., Barrera, J., Bellido, F., Benito, R., Brändle, J., Cebriá, J., Coello, J., Cubas, C., De la Nuez, J., Gómez, J., 2004. Canarias y el vulcanismo neógeno peninsular. In: Vera, J. (Ed.), Geología de España. Sociedad Geológica de España-Instituto Geológico y Minero de España, Madrid, pp 635-682.

Anders, M., Fouke, B., Zerkle, A., Tavarnelli, E., Alvarez, W., Harlow, G., 2010. The role of calcining and basal fluidization in the long runout of carbonate slides: an example from the Heart Mountain Slide Block, Wyoming and Montana, U.S.A. The Journal of Geology 118, 577-599. https://doi.org/10.1086/656383

Andrews, J., 1985. The isotopic composition of radiogenic helium and its use to study groundwater movement in confined aquifers. Chemical Geology 49, 339-351. https://doi.org/10.1016/0009-2541(85)90166-4

Aydin, A., Basu, A., 2005. The Schmidt hammer in rock material characterization. Engineering Geology 81, 1-14. https://doi.org/10.1016/j.enggeo.2005.06.006

Balek, J., Blahůt, J., 2017. A critical evaluation of the use of an inexpensive camera mounted on a recreational unmanned aerial vehicle as a tool for landslide research. Landslides 14, 1217-1224. https://doi.org/10.1007/s10346-016-0782-7

~~Baroň, I., Kernstocková, M., Novotný, R., Buriánek, D., Hradecký, P., Havlíček, P., Melichar, R., 2011. Palaeostress analysis of a giant Holocene rockslide near Boaco and Santa Lucia (Nicaragua, Central America). In: Jaboyedoff, M. (Ed.), Slope Tectonics. Geological Society of London, Special Publication 351, 133-145. https://doi.org/10.1144/SP351.7~~

Becerril, L., Ubide, T., Sudo, M., Martí, J., Galindo, I., Galé, C., Morales, J., Yepes, J., Lago, M., 2016a. Geochronological constraints on the evolution of El Hierro (Canary Islands). Journal of African Earth Sciences 113, 88-94. https://doi.org/10.1016/j.jafrearsci.2015.10.012

Becerril, L., Galve, J., Morales, J., Romero, C., Sánchez, N., Martí, J., Galindo, I., 2016b. Volcanostructure of El Hierro (Canary Islands). Journal of Maps 12, Supplement 1, 43-52. https://doi.org/10.1080/17445647.2016.1157767

Benito-Saz, M., Parks, M., Sigmundsson, F., Hooper, A., García-Cañada, L., 2017. Repeated magmatic intrusions at El Hierro Island following the 2011-2012 submarine eruption. Journal of Volcanology and Geothermal Research 344, 79-91. https://doi.org/10.1016/j.jvolgeores.2017.01.020

Blahůt, J., Rowberry, M., Balek, J., Klimeš, J., Baroň, I., Meletlidis, S., Martí, X., 2017. Monitoring giant landslide detachment planes in the era of big data analytics. In: Mikoš, M., Arbanas, Ž., Yin, Y., Sassa, K. (Eds.), Advancing Culture of Living with Landslides, Volume 3. Springer, Cham, pp. 333-340. https://doi.org/10.1007/978-3-319-53487-9_38

~~Blahůt, J., Baroň, I., Sokol, Ľ., Meletlidis, S., Klimeš, J., Rowberry, M., Melichar, R., García-Cañada, L., Martí, X., 2018a. Large landslide stress states calculated during extreme climatic and tectonic events on El Hierro, Canary Islands. Landslides 15, 1801-1814. https://doi.org/10.1007/s10346-018-0993-1~~

Blahůt, J., Klimeš, J., Rowberry, M., Kusák, M., 2018a~~b~~. Database of giant landslides on volcanic islands - first results from the Atlantic Ocean. Landslides 15, 823-827. https://doi.org/10.1007/s10346-018-0967-3

Blahůt, J., Baroň, I., Sokol, Ľ., Meletlidis, S., Klimeš, J., Rowberry, M., Melichar, R., García-Cañada, L., Martí, X., 2018~~a~~b. Large landslide stress states calculated during extreme climatic and tectonic events on El Hierro, Canary Islands. Landslides 15, 1801-1814. https://doi.org/10.1007/s10346-018-0993-1

Blahůt, J., Balek, J., Klimeš, J., Rowberry, M., Kusák, M., Kalina, J., 2019. A comprehensive global database of giant landslides on volcanic islands. Landslides 16 (10), 2045-2052. https://doi.org/ 10.1007/s10346-019-01275-8

Blard, P.-H., Balco, G., Burnard, P., Farley, K., Fenton, C., Friedrich, R., Jull, A., Niedermann, S., Pik, R., Schaefer, J., Scott, E., Shuster, D., Stuart, F., Stute, M., Tibari, B., Winckler, G., Zimmermann, L., 2015. An inter-laboratory comparison of cosmogenic ^{3}He and radiogenic ^{4}He in the CRONUS-P pyroxene standard. Quaternary Geochronology 26, 11-19. https://doi.org/10.1016/j.quageo.2014.08.004

703 Blard, P.-H., Farley K., 2008. The influence of radiogenic ^{4}He on cosmogenic ^{3}He determinations in volcanic
704 olivine and pyroxene. Earth and Planetary Science Letters 276, 20-29.
705 https://doi.org/10.1016/j.epsl.2008.09.003
706 Boutareaud, S., Calugaru, D.-G., Han, R., Fabbri, O., Mizoguchi, K., Tsutsumi, A., Shimamoto, T., 2008. Clay-clast
707 aggregates: a new textural evidence for seismic fault sliding? Geophysical Research Letters 35, L05302.
708 https://doi.org/10.1029/2007GL032554
709 Brodsky, E., Rowe, C., Meneghini, F., Moore, J., 2009. A geological fingerprint of low viscosity fault fluids
710 mobilized during an earthquake. Journal of Geophysical Research, Solid Earth 114, B01303.
711 https://doi.org/10.1029/2008JB005633
712 Carracedo, J.-C., 2008. Canarian Volcanoes IV: La Palma, La Gomera, El Hierro. Editorial Rueda S.L., Madrid, 213
713 pp.
714 Carracedo, J.-C., Day, S., Guillou, H., Pérez Torrado, F., 1997. Geology of the island of El Hierro, Canary Islands:
715 stratigraphy, volcanology, and structure. Excursion Guidebook, International Workshop on Volcanism
716 and Volcanic Hazards in Immature Intraplate Oceanic Islands, La Palma, 43 pp.
717 Carracedo, J.-C., Day, S., Guillou, H., Pérez Torrado, F., 1999. Giant quaternary landslides in the evolution of La
718 Palma and El Hierro, Canary Islands. Journal of Volcanology and Geothermal Research 94, 169-190.
719 https://doi.org/10.1016/S0377-0273(99)00102-X
720 Carracedo, J.-C., Rodríguez Badiola, E., Guillou, H., De la Nuez, H., Pérez Torrado, F., 2001. Geology and
721 volcanology of the western Canaries: La Palma and El Hierro. Estudios Geológicos 57, 171-295.
722 Carracedo, J.-C., Troll, V., 2016. The Geology of Canary Islands. Elsevier, Amsterdam, 622 pp.
723 Day, S., Carracedo, J.-C., Guillou, H., 1997. Age and geometry of an aborted rift flank collapse: the San Andres
724 fault system, El Hierro, Canary Islands. Geological Magazine 134, 523-537.
725 https://doi.org/10.1017/S0016756897007243
726 De Blasio, F., Elverhøi, A., 2008. A model for frictional melt production beneath large rock avalanches. Journal
727 of Geophysical Research, Earth Surface 113, F02014. https://doi.org/10.1029/2007JF000867
728 Di Toro, G., Han, R., Hirose, T., De Paola, N., Nielsen, S., Mizoguchi, K., Ferri, F., Cocco, M., Shimamoto, T., 2011.
729 Fault lubrication during earthquakes. Nature 471, 494-499. https://doi.org/10.1038/nature09838
730 Duffield, W., 1975. Structure and origin of the Koae Fault System, Kilauea Volcano, Hawaii. United States
731 Geological Survey, Professional Paper 856, 12 pp.

732 Faber, C., Rowe, C., Miller, J., Fagereng, Å., Neethling, J., 2014. Silica gel in a fault slip surface: field evidence for
733 palaeo-earthquakes? Journal of Structural Geology 69 108-121.
734 https://doi.org/10.1016/j.jsg.2014.09.021
735 Fondriest, M., Smith, S., Candela, T., Nielsen, S., Mair, K., Di Toro, G., 2013. Mirror-like faults and power
736 dissipation during earthquakes. Geology 41, 1175-1178. https://doi.org/10.1130/G34641.1
737 Gomberg, J., Bodin, P., Savage, W., Jackson, M., 1995. Landslide faults and tectonic faults, analogs? The
738 Slumgullion earthflow, Colorado. Geology 23, 41-44. https://doi.org/10.1130/0091-
739 7613(1995)023<0041:LFATFA>2.3.CO;2
740 Gómez Sainz de Aja, J., Klein, E., Ruiz García, M., Balcells Herrera, R., Del Pozo, M., Galindo, E., La Moneda, E.,
741 2010. Mapa Geológico de España, Escala 1:25 000, Valverde (Isla de El Hierro), Hoja N° 1105-II,
742 Memoria. Instituto Geológico y Minero de España, Madrid, 96 pp.
743 Goudie, A., 2006. The Schmidt hammer in geomorphological research. Progress in Physical Geography 30, 703-
744 718. https://doi.org/10.1177/0309133306071954
745 Grasemann, B., Dabrowski, M., 2015. Winged inclusions: pinch-and-swell objects during high-strain simple
746 shear. Journal of Structural Geology 70, 78-94. https://doi.org/10.1016/j.jsg.2014.10.017
747 Grasemann, B., Dabrowski, M., Schöpfer, M., 2019. Sense and non-sense of shear reloaded. Journal of
748 Structural Geology 125, 200-228. https://doi.org/10.1016/j.jsg.2018.05.028
749 Guillou, H., Carracedo, J.-C., Pérez Torrado, F., Rodríguez Badiola, E., 1996. K-Ar ages and magnetic stratigraphy
750 of a hotspot-induced, fast grown oceanic island: El Hierro, Canary Islands. Journal of Volcanology and
751 Geothermal Research 73, 141-155. https://doi.org/10.1016/0377-0273(96)00021-2
752 Han, R., Hirose, T., 2012. Clay-clast aggregates in fault gouge: an unequivocal indicator of seismic faulting at
753 shallow depths? Journal of Structural Geology 43, 92-99. https://doi.org/10.1016/j.jsg.2012.07.008
754 Han, R., Hirose, T., Shimamoto, T., Lee, Y., Ando, J., 2011. Granular nanoparticles lubricate faults during seismic
755 slip. Geology 39, 599-602. https://doi.org/10.1130/G31842.1
756 Hildenbrand, A., Marques, F., Catalao, J., Catita, C., Costa, A., 2012. Large scale active slump of the
757 southeastern flank of Pico Island, Azores. Geology 40, 939-942. https://doi.org/10.1130/G33303.1
758 Hunt, J.E., Wynn, R.B., Talling, P.J., Masson, D.G., 2013. Multistage collapse of eight western Canary Island
759 landslides in the last 1.5 Ma: Sedimentological and geochemical evidence from subunits in submarine

760 flow deposits. Geochemistry Geophysics Geosystems 14(7), 2159-2181. https://doi.org/
761 10.1002/ggge.20138
762 Hunt, J.E., Cassidy, M., Talling, P.J., 2018. Multi-stage volcanic island flank collapses with coeval explosive
763 caldera-forming eruptions. Scientific Reports 8, 1146. https://doi.org/10.1038/s41598-018-19285-2
764 Jaboyedoff, M., Penna, I., Pedrazzini, A., Baroň, I., Crosta, G., 2013. An introductory review on gravitational
765 deformation induced structures, fabrics, and modeling. Tectonophysics 605, 1-12.
766 https://doi.org/10.1016/j.tecto.2013.06.027
767 Karstens, J., Berndt, C., Urlaub, M., Watt, S.F.L., Micallef, A., Ray, M., Klaucke, I., Muff, S., Klaeschen, D., Kühn,
768 M., Roth, T., Böttner, C., Schramm, B., Elger, J., Brune, S., 2019. From gradual spreading to catastrophic
769 collapse – Reconstruction of the 1888 Ritter Island volcanic sector collapse from high-resolution 3D
770 seismic data. Earth and Planetary Science Letters 517, 1-13. https://doi.org/10.1016/j.epsl.2019.04.009
771 Kendrick, J., Lavallée, Y., Ferk, A., Perugini, D., Leonhardt, R., Dingwell, D., 2012. Extreme frictional processes in
772 the volcanic conduit of Mount St. Helens (USA) during the 2004-2008 eruption. Journal of Structural
773 Geology 38, 61-76. https://doi.org/10.1016/j.jsg.2011.10.003
774 Kendrick, J., Lavallée, Y., Hess, K.-U., De Angelis, S., Ferk, A., Gaunt, H., Meredith, P., 2014. Seismogenic
775 frictional melting in the magmatic column. Solid Earth 5, 199-208. https://doi.org/10.5194/se-5-199-
776 2014
777 Kirkpatrick, J., Rowe, C., White, J., Brodsky, E., 2013. Silica gel formation during fault slip: evidence from the
778 rock record. Geology 41, 1015-1018. https://doi.org/10.1130/G34483.1
779 Klimeš, J., Yepes, J., Becerril, L., Kusák, M., Galindo, I., Blahůt, J., 2016. Development and recent activity of the
780 San Andrés Landslide on El Hierro, Canary Islands, Spain. Geomorphology 261, 119-131.
781 https://doi.org/10.1016/j.geomorph.2016.02.018
782 Kurz, M., 1986. In situ production of ~~cosmogenic~~ terrestrial cosmogenic helium and some applications to
783 geochronology. Geochimica et Cosmochimica Acta 50, 2855-2862. https://doi.org/10.1016/0016-
784 7037(86)90232-2
785 Lal, D., 1991. Cosmic ray labeling of erosion surfaces: in situ nuclide production rates and erosion models. Earth
786 and Planetary Science Letters 104, 424-439. https://doi.org/10.1016/0012-821X(91)90220-C

787 Lavallée, Y., Hirose, T., Kendrick, J., De Angelis, S., Petrakova, L., Hornby, A., Dingwell, D., 2014. A frictional law
788 for volcanic ash gouge. Earth and Planetary Science Letters 400, 177-183.
789 https://doi.org/10.1016/j.epsl.2014.05.023
790 Lavallée, Y., Mitchell, T., Heap, M., Vasseur, J., Hess, K.-U., Hirose, T., Dingwell, D., 2012. Experimental
791 generation of volcanic pseudotachylytes: constraining rheology. Journal of Structural Geology 38, 222-
792 233. https://doi.org/10.1016/j.jsg.2012.02.001
793 Legros, F., Cantagrel, J.-M., Devouard, B., 2000. Pseudotachylite (frictionite) at the base of the Arequipa
794 Volcanic Landslide Deposit (Peru): implications for emplacement mechanisms. The Journal of Geology
795 108, 601-611. https://doi.org/10.1086/314421
796 León, R., Somoza, L., Urgeles, R., Medialdea, T., Ferrer, M., Biain, A., García-Crespo, J., Mediato, J., Galindo, I.,
797 Yepes, J., González, F., Gimenez-Moreno, J., 2017. Multi-event oceanic island landslides: new onshore-
798 offshore insights from El Hierro Island, Canary Archipelago. Marine Geology 393, 156-175.
799 https://doi.org/10.1016/j.margeo.2016.07.001
800 Liu, C., Lay, T., Xiong, X., 2018. Rupture in the 4 May 2018 M_W 6.9 earthquake seaward of the Kilauea East Rift
801 Zone fissure eruption in Hawaii. Geophysical Research Letters 45, 9508-9515.
802 https://doi.org/10.1029/2018GL079349
803 Longpré, M., Chadwick, J., Wijbrans, J., Iping, R., 2011. Age of the El Golfo debris avalanche, El Hierro (Canary
804 Islands): new constraints from laser and furnace $^{40}Ar/^{39}Ar$ dating. Journal of Volcanology and
805 Geothermal Research 203, 76-80. https://doi.org/10.1016/j.jvolgeores.2011.04.002
806 López, C., Blanco, M., Abella, R., Brenes, B., Cabrera Rodríguez, V., Casas, B., Domínguez Cerdeña, I., Felpeto, A.,
807 Fernández de Villalta, M., Del Fresno, C., et al., 2012. Monitoring the volcanic unrest of El Hierro (Canary
808 Islands) before the onset of the 2011-2012 submarine eruption. Geophysical Research Letters 39,
809 L13303. https://doi.org/10.1029/2012GL051846
810 Maddock, R., 1986. Frictional melting in landslide generated frictionites (hyalomylonites) and fault generated
811 pseudotachylytes: discussion. Tectonophysics 128, 151-153. https://doi.org/10.1016/0040-
812 1951(86)90316-1
813 Martin, L., Blard, P.-H., Balco, G., Lave, J., Delunel, R., Lifton, N., Laurent, V., 2017. The CREp program and the
814 ICE-D production rate calibration database: a fully parameterizable and updated online tool to compute

cosmic-ray exposure ages. Quaternary Geochronology 38, 25-49. https://doi.org/10.1016/j.quageo.2016.11.006

Masch, L., Wenk, H., Preuss, E., 1985. Electron microscopy of hyalomylonites - evidence for frictional melting in landslides. Tectonophysics 115, 131-160. https://doi.org/10.1016/0040-1951(85)90103-9

Masson, D., 1996. Catastrophic collapse of the volcanic island of Hierro 15 ka ago and the history of landslides in the Canary Islands. Geology 24, 231-234. https://doi.org/10.1130/0091-7613(1996)024<0231:CCOTVI>2.3.CO;2

Masson, D., Watts, A., Gee, M., Urgeles, R., Mitchell, N., Le Bas, T., Canals, M., 2002. Slope failures on the flanks of the western Canary Islands. Earth-Science Reviews 57, 1-35. https://doi.org/10.1016/S0012-8252(01)00069-1

McGuire, W., 1996. Volcano instability: a review of contemporary themes. In: McGuire, W., Jones, A., Neuberg, J. (Eds.), Volcano Instability on the Earth and Other Planets. Geological Society of London, Special Publication 110, 1-23. https://doi.org/10.1144/GSL.SP.1996.110.01.01

Meletlidis, S., Di Roberto, A., Domínguez Cerdeña, I., Pompilio, M., García-Cañada, L., Bertagnini, A., Benito-Saz, M., Del Carlo, P., Sainz-Maza Aparicio, S., 2015. New insight into the 2011-2012 unrest and eruption of El Hierro Island (Canary Islands) based on integrated geophysical, geodetical, and petrological data. Annals of Geophysics 58, S0546. https://doi.org/10.4401/ag-6754

Mitchell, T., Smith, S., Anders, M., Di Toro, G., Nielsen, S., Cavallo, A., Beard, A., 2015. Catastrophic emplacement of giant landslides aided by thermal decomposition: Heart Mountain, Wyoming. Earth and Planetary Science Letters 411, 199-207. https://doi.org/10.1016/j.epsl.2014.10.051

Moscardelli, L., Wood, L., 2008. New classification system for mass transport complexes in offshore Trinidad. Basin Research 20, 73-98. https://doi.org/10.1111/j.1365-2117.2007.00340.x

Palumbo, L., Benedetti, L., Bourlès, D., Cinque, A., Finkel, R., 2004. Slip history of the Magnola Fault (Apennines, Central Italy) from ^{36}Cl surface exposure dating: evidence for strong earthquakes over the Holocene. Earth and Planetary Science Letters 225, 163-176. https://doi.org/10.1016/j.epsl.2004.06.012

Paris, R., Ramalho, R.S., Madeira, J., Ávila, S., May, S.M., Rixhon, G., Engel, M., Brűckner, H., Herzog, M., Schukraft, G., Perez-Torrado, F.J., Rodriguez-Gonzales, A., Carracedo, J.C., Giachetti, T., 2018. Mega-tsunami conglomerates and flank collapses of ocean volcanoes. Marine Geology 395, 168-187. https://doi.org/ 10.1016/j.margeo.2017.10.004

844 Passchier, C., Trouw, R., 2005. Microtectonics. Springer, Berlin, 366 pp. https://doi.org/10.1007/3-540-29359-0
845 Poujol, A., Ritz, J.-F., Tahayt, A., Vernant, P., Condomines, M., Blard, P.-H., Billant, J., Vacher, L., Tibari, B., Hni,
846 L., Koulali Idrissi, A., 2014. Active tectonics of the Northern Rif (Morocco) from geomorphic and
847 geochronological data. Journal of Geodynamics 77, 70-88. https://doi.org/10.1016/j.jog.2014.01.004
848 Price, N., Johnson, S., Gerbi, C., West, D., 2012. Identifying deformed pseudotachylyte and its influence on the
849 strength and evolution of a crustal shear zone at the base of the seismogenic zone. Tectonophysics 518-
850 521, 63-83. https://doi.org/10.1016/j.tecto.2011.11.011
851 Protin, M., Blard, P.-H., Marrocchi, Y., Mathon, F., 2016. Irreversible adsorption of atmospheric helium on
852 olivine: a lobster pot analogy. Geochimica et Cosmochimica Acta 179, 76-88.
853 https://doi.org/10.1016/j.gca.2016.01.032
854 Rasa, R., Azzaro, R., Leonardi, O., 1996. Aseismic creep on faults and flank instability at Mount Etna Volcano,
855 Sicily. In: McGuire, W., Jones, A., Neuberg, J. (Eds.), Volcano Instability on the Earth and Other Planets.
856 Geological Society of London, Special Publication 110, 179-192.
857 https://doi.org/10.1144/GSL.SP.1996.110.01.14
858 Rempe, M., Smith, S., Ferri, F., Mitchell, T., Di Toro, G., 2014. Clast-cortex aggregates in experimental and
859 natural calcite bearing fault zones. Journal of Structural Geology 68, 142-157.
860 https://doi.org/10.1016/j.jsg.2014.09.007
861 Rowe, C., Fagereng, Å., Miller, J., Mapani, B., 2012. Signature of coseismic decarbonation in dolomitic fault
862 rocks of the Naukluft Thrust, Namibia. Earth and Planetary Science Letters 333-334, 200-210.
863 https://doi.org/10.1016/j.epsl.2012.04.030
864 Rowe, C., Griffith, W., 2015. Do faults preserve a record of seismic slip: a second opinion. Journal of Structural
865 Geology 78, 1-26. https://doi.org/10.1016/j.jsg.2015.06.006
866 Rowe, C., Lamothe, K., Rempe, M., Andrews, M., Mitchell, T., Di Toro, G., Clancy White, J., Aretusini, S., 2019.
867 Earthquake lubrication and healing explained by amorphous nanosilica. Nature Communications 10,
868 320. https://doi.org/10.1038/s41467-018-08238-y
869 Rowe, C., Moore, J., Meneghini, F., McKeirnan, A., 2005. Large scale pseudotachylytes and fluidized cataclasites
870 from an ancient subduction thrust fault. Geology 33, 937-940. https://doi.org/10.1130/G21856.1
871 Sagy, A., Brodsky, E., Axen, G., 2007. Evolution of fault surface roughness with slip. Geology 35, 283-286.
872 https://doi.org/10.1130/G23235A.1

873 Siebert, L., 1984. Large volcanic debris avalanches: characteristics of source areas, deposits, and associated
874 eruptions. Journal of Volcanology and Geothermal Research 22, 163-197. https://doi.org/10.1016/0377-
875 0273(84)90002-7
876 Siebert, L., 1992. Threats from debris avalanches. Nature 356, 658-659. https://doi:10.1038/356658a0
877 Smeraglia, L., Bettucci, A., Billi, A., Carminati, E., Cavallo, A., Di Toro, G., Natali, M., Passeri, D., Rossi, M.,
878 Spagnuolo, E., 2017. Microstructural evidence for seismic and aseismic slips along clay-bearing,
879 carbonate faults. Journal of Geophysical Research, Solid Earth 122, 3895-3915.
880 https://doi.org/10.1002/2017JB014042
881 Smith, S., Billi, A., Di Toro, G., Spiess, R., 2011. Principal slip zones in limestone: microstructural characterization
882 and implications for the seismic cycle (Tre Monti Fault, Central Apennines, Italy). Pure and Applied
883 Geophysics 168, 2365-2393. https://doi.org/10.1007/s00024-011-0267-5
884 Sorriso-Valvo, M., Gullà, G., Antronico, L., Tansi, C., Amelio, M., 1999. Mass movement, geologic structure, and
885 morphologic evolution of the Pizzotto-Greci Slope (Calabria, Italy). Geomorphology 30, 147-163.
886 https://doi.org/10.1016/S0169-555X(99)00051-3
887 Széréméta, N., Laj, C., Guillou, H., Kissel, C., Mazaud, A., Carracedo, J.-C., 1999. Geomagnetic paleosecular
888 variation in the Brunhes period, from the island of El Hierro (Canary Islands). Earth and Planetary
889 Science Letters 165, 241-253. https://doi.org/10.1016/S0012-821X(98)00270-2
890 Tesei, T., Carpenter, B., Giorgetti, C., Scuderi, M., Sagy, A., Scarlato, P., Collettini, C., 2017. Friction and scale-
891 dependent deformation processes of large experimental carbonate faults. Journal of Structural Geology
892 100, 12-23. https://doi.org/10.1016/j.jsg.2017.05.008
893 Ui, T., Takarada, S., Yoshimoto, M., 2000. Debris avalanches. In: Sigurdsson, H., Houghton, B., McNutt, S.,
894 Rymer, H., Stix, J. (Eds.), Encyclopedia of Volcanoes. Academic Press, San Diego, pp. 617-626.
895 Ujiie, K., Tsutsumi, A., Kameda, J., 2011. Reproduction of thermal pressurization and fluidization of clay-rich
896 fault gouges by high-velocity friction experiments and implications for seismic slip in natural faults.
897 Geological Society of London, Special Publication 359, 267-285. https://doi.org/10.1144/SP359.15
898 Urgeles, R., Canals, M., Baraza, J., Alonso, B., 1996. The submarine El Golfo debris avalanche and the Canary
899 debris flow, west Hierro Island: the last major slides in the Canary Archipelago. Geogaceta 20, 390-393.

Urgeles, R., Canals, M., Baraza, J., Alonso, B., Masson, D., 1997. The most recent megalandslides on the Canary Islands: the El Golfo debris avalanche and the Canary debris flow, west El Hierro Island. Journal of Geophysical Research, Solid Earth 102, 20305-20323. https://doi.org/10.1029/97JB00649

Verberne, B., De Bresser, J., Niemeijer, A., Spiers, C., ~~Matthijs d~~De Winter, M.D., Plümper, O., 2013. Nanocrystalline slip zones in calcite fault gouge show intense crystallographic preferred orientation: crystal plasticity at subseismic slip rates at 18-150°C. Geology 41, 863-866. https://doi.org/10.1130/G34279.1

Walter, T.R., Haghighi, M.H., Schneider, F.M., Coppola D, Motagh, M., Saul, J., Babeyko, A., Dahm, T., Troll, V.R., Tilmann, F., Heimann, S., Valade, S., Triyono, R., Khomarudin, R., Kartadinata, N., Laiolo, M., Massimetti, F., Gaebler, P., 2019. Complex hazard cascade culminating in the Anak Krakatau sector collapse. Nature Communications 10, 4339. https://doi.org/10.1038/s41467-019-12284-5

Weidinger, J., Korup, O., Munack, H., Altenberger, U., Dunning, S., Tippelt, G., Lottermoser, W., 2014. Giant rockslides from the inside. Earth and Planetary Science Letters 389, 62-73. https://doi.org/10.1016/j.epsl.2013.12.017

Zimmermann, L., Avice, G., Blard, P.-H., Marty, B., Füri, E., Burnard, P., 2018. A new all-metal induction furnace for noble gas extraction. Chemical Geology 480, 86-92. https://doi.org/10.1016/j.chemgeo.2017.09.018

Figure captions

Figure 1 A shaded topographic and bathymetric relief map of El Hierro, Canary Islands, overlain by a geological map simplified from Ancochea et al. (2004). The inset shows an aerial image of the studied fault outcrop. SAL: San Andrés Landslide.

Figure 2 (A) General view of the San Andrés Fault outcrop showing the location of each sampling site. The numbers in parentheses following after COS samples 1-5 indicate the estimated exposure ages in ka. (B) Detailed view of the fault outcrop which shows a series of conspicuous vertical or subvertical slickenlines and the whitish layer adorning the recently exposed parts of its surface; (C) Contact between the footwall (left) and the hanging wall (right); (D) Detailed view of the oxidised rock visible in the footwall of the fault which reflects the presence of fine grained Fe-oxides and Fe-hydroxides. (E, F) Samples used for microstructural analysis: (E1) hand sample MSA1 shows slickenlines composed of the whitish layer - note the dashed line parallel to the slickenlines; (E2) closeup view of the slickenlines, (E3) rock slab used to extract thin sections shows the whitish layer that covers the cataclasite and breccia. The black rectangles mark the positions of Figures 5-6; (F1) core sample MSA2 drilled perpendicular to the fault surface shows large clasts in the breccia and white layer - red dashed line highlights the orientation of the slickenlines; (F2) rock slab shows the gradual increase in oxidation of the breccia towards the fault surface; (F3) thin section shows the sharpness of the slip surface and the barely-visible white silica layer. The black rectangle marks the location of Figure 7.

Figure 3 Structural analysis of the surface of the San Andrés Fault outcrop conducted on the basis of a remotely sensed UAV DTM. (A) Slope gradient map giving a ground plan view presented in inverted greyscale and showing distinct sets of striations and elongated bumps. (B) Slope gradient map giving a fault perpendicular view presented in inverted greyscale and visualised in three dimensions (for reference see the right hand part of the fault in (A)). (C) Orientation of the fault surfaceStereoplot of the structural geological measurements and the striations revealed by the

morphostructural analysis of the UAV DTM. The stereoplot is in azimuthal projection of the lower hemisphere while the different coloured arrows represent distinct sets of striations and elongated protrusions.

Figure 4 The interpolated R-values obtained through Schmidt hammer sampling on the San Andrés Fault. The size of the ~~proportional plots~~black dots illustrates the rock hardness at each of the test sites.

Figure 5 Photomicrographs and BSE images of rock~~s~~ from the San Andrés Fault, sample MSA1. First area presented (~~a~~A) under plane polarised light, (~~b~~B) under cross polarised light, (~~c~~C) as a sketch, (~~d~~D) in BSE~~backscattered mode~~, and (~~e f~~E-F) in elemental maps. These show tectonic breccia (TB) covered by a cataclastic layer (CL) which is, in turn, covered by a silica layer (SL). The cataclasite cuts both the tectonic breccia and a zeolite vein (Z) and has preserved P-foliation and a winged inclusion. The boundary between the silica layer and the adjacent cataclastic layer is sharp with high interference bands, characteristic of recrystallisation. The area is rotated during analysis and the sense of shear is marked on the sketch. Second area presented (~~g~~G) under plane polarised light, (~~h~~H) under cross polarised light, (~~i~~I) as a sketch, (~~j~~J) in BSE~~backscattered mode~~, and (~~k l~~K-L) in elemental maps. These show tectonic breccia (TB) with zeolite veins (Z) covered by a thinner cataclastic layer (CL) and a thicker silica layer (SL). The fault slip surface is subhorizontal with a top-to-right shear direction. The boundary between the cataclastic layer and the silica layer is marked by high intensity bands of recrystallised material. The silica layer preserves clast-cortex aggregates (CCA) and flow bands (FB) along with parallel P- and Y- shears. The elongated void was most probably a clast-cortex aggregate lost during preparation of the sample.

Figure 6 Photomicrographs and BSE images of rock~~s~~ from the San Andrés Fault, sample MSA1. Area presented in (~~a~~A) under plane polarised light, (~~b~~B) under cross polarised light, (~~c~~C) under cross polarised light using a gypsum tint plate, (~~d~~D) in BSE~~backscattered mode~~, and (~~e~~E) as a sketch. These show tectonic breccia (TB) covered by a silica layer (SL). The tectonic breccia was cut during deformation which resulted in truncated clasts (TC) while the silica layer preserves clast-cortex aggregates (CCA), a cataclastic sublayer (CL), and flow bands (FB). These flow bands show a positive

birefringence, in contrast to the rest of the silica layer, as evidenced by the second order blue interference colour in (~~c~~C). The rectangles in (~~d~~D) indicate regions highlighted in (~~f~~-~~i~~F-I): (~~f~~F) new crystals growing in a void surrounded by ultrafine grained to amorphous matrix, (~~g~~G) a large clast-cortex aggregate with a complex cortex and elongated clast in its core, (~~h~~H) a lensoid of reworked cataclasite, and (~~i~~I) two smaller clast-cortex aggregates and new crystals growing in the void. The fault slip surface is horizontal with a top-to-right shear direction.

Figure 7 Photomicrographs and BSE images of rock~~s~~ from the San Andrés Fault, sample MSA2. Area presented in (~~a~~A) under plane polarised light, (~~b~~B) under cross polarised light using a gypsum tint plate, and (~~c~~C) as a sketch. These show a large truncated clast (TC) in the tectonic breccia (TB) cut by cataclasite (CL) and covered by a silica layer (SL) which has flow bands (FB) and clast-cortex aggregates (CCA). The rectangle in (~~a~~A) indicates the region highlighted in (~~d~~-~~f~~D-F). In (~~d~~-~~f~~D-F) elemental maps show P-foliation in the cataclastic layer along with clast-cortex aggregates and flow bands in the silica layer. Dashed lines highlight characteristics presented in the sketch. The fault slip surface is horizontal with a top-to-right shear direction.

Figure 8 A ~~proposed~~ conceptual model for the development of the San Andrés Fault system over the last 550 ka based on Day et al. (1997), Carracedo et al. (1997), Széréméta et al. (1999), León et al. (2017), and the findings presented herein. The uppermost labels denote the main geological events to have taken place on El Hierro, i.e. rotation and volcanism, while those beneath denote the supposed age ranges for each of the giant landslides. The proposed timing of activity on the San Andrés Fault is presented underneath the timeline: the first slip event is associated with the formation of the cataclasite while the second slip event is associated with the formation of the silica layer. The time axis depicts~~shows~~ thousands of years before present.

Figure 9 A ~~proposed~~ conceptual model for the development of the surface of the San Andrés Fault. Prior to slip a tectonic breccia, of basaltic origin, hosted zeolite veins, as shown in green. During the first slip event the tectonic breccia was sheared and a foliated cataclasite formed, as shown in red.

During the second slip event both the host rock and foliated cataclasite were sheared and a silica layer formed with clast-cortex aggregate and flow bands, as shown in blue.

Table captions

Table 1 Results of the cosmogenic ^{3}He exposure dating for five samples obtained from the San Andrés Fault.

Supp. Tab. A Chemical composition of the five samples obtained from the San Andrés Fault for cosmogenic ^{3}He exposure dating (COS1 - COS5).

Volcanic edifice slip events recorded on the fault plane of the San Andrés Landslide, El Hierro, Canary Islands

Jan BLAHŮT[a], Ivanka MITROVIC-WOODELL[b], Ivo BAROŇ[a], Miloš RENÉ[a], Matt ROWBERRY[a], Pierre-Henri BLARD[c], Filip HARTVICH[a], Jan BALEK[a], Stavros MELETLIDIS[d]

[a] Institute of Rock Structure and Mechanics, The Czech Academy of Sciences, V Holešovičkách 41, 182 09 Prague 8, Czech Republic

[b] Department of Geodynamics and Sedimentology, University of Vienna, Althanstraße 14, 1090 Vienna, Austria

[c] Centre de Recherches Pétrographiques et Géochimiques (CRPG), UMR 7358, CNRS - Université de Lorraine, 15 rue Notre Dame des Pauvres, 54500 Vandœuvre-lès-Nancy, France

[d] Centro Geofísico de Canarias, Instituto Geográfico Nacional, Calle Marina 20, 38001 Santa Cruz de Tenerife, Spain

* corresponding author: blahut@irsm.cas.cz

Abstract: Volcanic flank collapses often result in giant debris avalanches that are capable of travelling tens of kilometres across the ocean floor and generating tsunamis that devastate distant communities. The San Andrés Landslide on El Hierro, Canary Islands, represents one of the few places in the world where it is possible to investigate the landslide mass and fault planes of a volcanic collapse structure. In this study, a new conceptual model for the development of this enormous slump is presented on the basis of structural geological and geomorphological measurements, petrological and microstructural analyses, and cosmogenic radionuclide dating. Structural geological and geomorphological measurements indicate that the fault plane records two distinct events. Petrological and microstructural analyses demonstrate that a thin layer of frictionite covers the surface of the fault in contact with an oxidised tectonic breccia that transitions into the underlying undeformed basanite host rock. This frictionite comprises a heterogeneous cataclastic layer and a translucent silica layer that are interpreted to represent two separate slip events on the basis of their architecture and crosscutting relationships. Cosmogenic ^{3}He dating reveals a maximum exposure age of 183±17 ka to 52±17 ka. Arguments are presented in support of the idea that the first slip event took place between 545 ka and 430 ka, prior to significant clockwise rotation of El Hierro, and the second slip event took place between 183 ka and 52 ka, perhaps in association with one of the giant debris avalanches that occurred around that time. This is the first time that more than one slip event has been recognised from the fault plane of the San Andrés Landslide. It is also believed to be the first time a silica layer resulting from frictional melt has been described in a volcanic setting.

Keywords volcanic collapse; frictionite; cataclasis metamorphism; silica layer; cosmogenic radionuclide dating; Canary Islands

1. Introduction

Gravitational slope failures generate geological structures at a range of scales that are similar or identical to those that result from tectonic processes (Jaboyedoff et al., 2013). Consequently, faults generated as a result of large slope failures are often analogous to their tectonic counterparts (Gomberg et al., 1995). Some of the largest slope failures on Earth are represented by volcanic flank collapses on oceanic islands – these events are so enormous that they are also comparable to the largest mass movements on Mars (Blahůt et al., 2019). The processes that lead to volcanic flank collapses on oceanic islands are not well understood despite their potential to generate catastrophic tsunamis (Paris et al., 2018; Walter et al., 2019). In part this situation reflects the dearth of events as volcanic flank collapses are estimated to have only occurred four times a century for the past five hundred years (Siebert, 1992). Volcanic flank collapses on oceanic islands are usually represented by debris avalanches (sensu Ui et al., 2000), which displace huge volumes of rock and create amphitheatre shaped calderas (Siebert, 1984). Such debris avalanches localise shear deformation along thin sliding surfaces at the base of the displaced mass (De Blasio and Elverhøi, 2008). These events are triggered by a range of factors which can be broadly categorised as seismogenic or magmagenic (McGuire, 1996). Therefore, while huge debris avalanches may occur in other settings, volcanic flank collapses on oceanic islands are especially dangerous due to the interminable nature of the potential triggering events, i.e. volcanic tremors and related seismicity, coupled with the adjacency of an extremely high risk impact environment, i.e. seawater. The run-up heights of consequent tsunami waves may exceed 100 m (Karstens et al., 2019; Walter et al., 2019). Occasionally, volcanic collapses are represented by creeping or slumping but only a small number of studies have focused on these processes. Examples come from Mount Etna in Sicily (Rasa et al., 1996), Pico Ridge in the Azores (Hildebrand et al., 2012), San Andrés in the Canary Islands (Blahůt et al., 2017), and Hilina Slump in the Hawaiian Islands (Liu et al. 2018).

During landslide emplacement, flash heating may occur along thin shear layers to produce frictional melt, referred to as frictionite or landslide pseudotachylyte (Masch et al., 1985; Maddock, 1986; Legros et al., 2000; Lavallée et al., 2012; Mitchell et al., 2015). Frictionite is a subtype of pseudotachylyte, *sensu lato*, which is generated at the base of landslides, as opposed to pseudotachylyte, *sensu stricto*, which is generated in greater depths with higher pressure and temperature conditions (Maddock, 1986). Frictionite tends to have thicknesses of between one and three centimetres and develops parallel or subparallel to the dip of the

landslide (Weidinger et al., 2014). Indicators of frictionite include significant grain size reduction, evidence for fluidised flow, and the presence of amorphous material. Other types of cohesive fault rocks, such as microbreccias and cataclasites, are common during the emplacement of large landslides. Cataclasites typically show grain size reduction, compared to the host rock, with development of foliation. To accurately assess the hazard relating to volcanic flank collapses it is crucial to be able to estimate the strength and velocity of the landslide. Fast slip along shallow faults can be inferred by the presence of devitrified material observed in pseudotachylytes, clast-cortex aggregates (Smith et al., 2011; Han and Hirose, 2012; Rempe et al., 2014), silica layers (Kirkpatrick et al., 2013; Faber et al. 2014), and other type of fault rock architecture. Pseudotachylytes and frictionites are ultrafine-grained rocks, with the presence of partial melt. Clast-cortex aggregates comprise of a central clast enclosed within a layer, or concentric layers, of material akin to the matrix (e.g. Anders et al., 2010; Rowe et al., 2012). Silica layers are composed of translucent silica with microstructures that exhibit flow banding, armoured clasts, and extreme comminution compared to adjacent rocks (Kirkpatrick et al., 2013; Faber et al., 2014). These fault rock structures are not common – they are known to occur in a range of tectonic settings but have not been reported in relation to volcanic flank collapses. The first report of frictionite at the base of a landslide was described from the Köfels landslide in the Austrian Alps (Masch et al., 1985) while the first report of frictionite at the base of a landslide in a volcanic environment was described from the Arequipa volcanic landslide deposit in Peru (Legros et al., 2000). Furthermore, volcanoes tend to be basic in composition and silica layers are not expected to form in predominantly basic environment.

Reconstruction of past volcanic failures in their source areas is extremely rare as there is usually no material to study and/or the main scarp has since been covered by younger eruptions. For that reason, the majority of studies have focused on the sedimentological properties of these failures (e.g. Hunt et al., 2013). Until recently, it has been assumed that the volcanic flank collapses occur as one major event that displaces hundreds of cubic kilometres of rock. However, new research suggests that at least some of these collapses occurred in multiple stages (Hunt et al., 2013, 2018; León et al., 2017). Such findings may have serious implications for the calculated frequency of such hazards and reopens questions about the possible reactivation of apparently inactive structures. The San Andrés Landslide on El Hierro in the Canary Islands represents one of the few places in the world where it is possible to investigate the fault planes and landslide mass of a volcanic collapse structure. This study integrates a range of structural geological and geomorphological measurements,

petrological and microstructural analyses, and cosmogenic nuclide dating in order to reconstruct the developmental history of this huge slope failure. Data have been obtained - directly or indirectly - from the surface of the fault plane while samples were collected from both the fault plane itself and an adjacent gully perpendicular to the footwall. Our hypothesis states that this landslide is not the result of a single event, as proposed by Day et al. (1997), but instead results from a number of successive events spanning a protracted period. This hypothesis is not straightforward to address as unambiguous evidence for multiple slip events along a single fault is difficult to elucidate due to problems associated with overprinting and weathering. Nonetheless, on the basis of previously published research and the results obtained during this study, it has been possible to propose a new conceptual model for the development of the San Andrés Landslide.

2. Geological setting

2.1 *The island of El Hierro*

El Hierro is an active volcanic edifice that constitutes the smallest and youngest of the Canary Islands (Figure 1). Its oldest subaerially exposed rocks are represented by the Tiñor Unit, with a maximum age of 1.12 Ma (Guillou et al., 1996), which form the northern and northeastern parts of the island. This unit is thought to have developed rapidly until around the time of the Tiñor debris avalanche at 0.88 Ma (Carracedo et al., 2001). Thereafter, the rocks of the El Golfo-Las Playas Unit, with a maximum age of 0.55 Ma (Guillou et al., 1996), capped much of the Tiñor Unit and infilled the scarp area of the Tiñor debris avalanche (Carracedo et al., 2001). Its youngest subaerially exposed rocks are represented by the Rift Series, with a maximum age of 0.16 Ma (Guillou et al., 1996). Over the past 33 000 years onshore eruptions have reoccurred approximately once every 1 000 years (Becerril et al., 2016a). The latest, ongoing phase of volcanism began around 2.5 ka (Carracedo et al., 2001). Recently a period of intense seismic activity spanned from July 2011 (López et al., 2012) to 2014 (Benito-Saz et al., 2017). During this period an offshore eruption started on 10 October 2011 and finished in March 2012 (Meletlidis et al., 2015). A more detailed description of the geology of island has recently been presented elsewhere (Carracedo and Troll, 2016).

The flanks of El Hierro have hosted a number of enormous gravitational slope failures which have contributed to the development of its characteristic three-point star morphology (Figure 1). Until now, seven debris avalanches have been identified: Tiñor (< 880 ka), Las Playas I (545-176 ka), Las Playas II (176-145 ka), El Julan

(> 158 ka), El Golfo A (176-133 ka), El Golfo B (87-39 ka), and Punta del Norte of unknown age (Masson, 1996; Urgeles et al., 1996, 1997; Carracedo et al., 1999, 2001; Masson et al., 2002; Longpré et al., 2011; Becerril et al., 2016b; Carracedo and Troll, 2016; León et al., 2017; Blahůt et al., 2018a). The volumes of these debris avalanches vary between 50 km^3 and 234 km^3, which makes them average from the known volcanic slope failures (for additional morphometric characteristics, see Blahůt et al., 2019). In addition, a large slump, sensu Moscardelli and Wood (2008), or a deep seated gravitational slope deformation, sensu Sorriso-Valvo et al. (1999) or Agliardi et al. (2001), is located on the southeast flank of the volcanic edifice. This feature, the San Andrés Landslide, is defined by a group of pronounced faults which represent landslide detachment planes. While its volume has not been determined, the deformed toe is visible around 18 km off coast at a depth of more than 3 km (Becerril et al., 2016b). Similar features have been described from other volcanic islands including the Azores (Hildenbrand et al., 2012) and the Hawaiian Islands (Duffield, 1975). It has previously been proposed that the San Andrés Landslide is an anchored block associated with the debris avalanche Las Playas I (Day et al., 1997).

2.2 *San Andrés Landslide*

The San Andrés Landslide has developed in the volcanic rocks of the Tiñor Unit. This unit comprises three distinct subunits (Gómez Sainz de Aja et al., 2010): the basal subunit is represented by relatively thin, 20-40 cm, steeply dipping lava flows; the intermediate subunit, which forms the majority of the unit, is represented by thicker, up to 4 m, shallow dipping lava flows; while the uppermost subunit is represented by emission vents with well-preserved craters and associated lavas. The broad arcuate and presumably listric fault system which defines the boundaries of the slope deformation to the northeast is terminated to the southwest by an escarpment associated with the giant debris avalanche Las Playas II. Previously the San Andrés Landslide has been interpreted as either an aborted collapse structure (Day et al., 1997) or a deep seated gravitational slope deformation (Klimeš et al., 2016).

It has been reasoned that the fault system must have developed at some point between 545 ka and about 261-176 ka (Day et al., 1997). If correct, this implies that the collapsed landslide mass has remained anchored during each of the subsequent giant debris avalanches on El Hierro (Carracedo and Troll, 2016). Support for the notion of protracted inactivity is provided by the presence of younger lavas crossing the fault without

158 displacement and the presence of scree covering lava flows as old as 145 ka in the gully of Las Playas
159 (Carracedo et al., 1997). However, recent research is starting to challenge these arguments. The step-like
160 structure of the incised gullies in the collapsed mass, together with records of progressive creep along its main
161 detachment plane, in the order of 0.5 mm.a^{-1}, suggests that the landslide mass may be moving steadily to the
162 east and southeast (Klimeš et al., 2016; Blahůt et al., 2017, 2018b).
163
164 The part of San Andrés Fault system investigated in this study is exposed along a narrow road which traverses
165 the Barranco de Tiñor (27°47'18.82"N, 17°55'19.04"W). This outcrop is situated at c. 490 m asl, has a length of
166 c. 70 m, and dips between 65° and 75° to the SE (Figure 2). The fault zone has a total thickness of between one
167 and two metres. Both the footwall and hanging wall rocks comprise basaltic lavas of the Tiñor Unit with a few
168 thin intercalated lapilli beds and soil horizons (Carracedo et al., 1997). No indurated breccia is present on the
169 hanging wall. Its eastern section has only been uncovered relatively recently as a result of road construction
170 and is distinguished by its whitish surface. This part of the fault surface hosts well-preserved slickenlines, which
171 range in size from several millimetres to metre scale surface undulations. Detailed petrographic examinations
172 of the fault rocks have been published previously (Day et al., 1997).
173
174 **3. Methods**
175 3.1 *Field data and structural analyses*
176 Structural analyses of the surface of the San Andrés Fault plane incorporated structural geological field
177 measurements alongside the interrogation of a high resolution digital terrain model (DTM). This DTM was
178 constructed on the basis of photogrammetric imagery obtained from an unmanned aerial vehicle (UAV) and
179 processed using the commercial software Agisoft PhotoScan (Agisoft LLC, 2014). The accuracy of terrain models
180 constructed following this approach is directly comparable to those constructed on the basis of laser scanning
181 (Balek and Blahůt, 2017). From the photogrammetric point cloud, it was possible to derive two complimentary
182 slope gradient maps with grid cells of 2 x 2 cm. The first gives a ground plan view of the fault (Figure 3A) while
183 the second gives a fault perpendicular view (Figure 3B). These maps have been analysed in detail using the
184 ESRI® ArcGIS applications ArcMap and ArcScene. Slope gradient maps, in contrast to hillshade maps, are
185 particularly suited for the identification of linear features irrespective of their spatial distribution and

186 orientations. The obtained data were then compared to the structural geological field measurements recorded
187 on the outcrop.
188
189 Schmidt hammer sampling is used in geomorphological research to estimate rates of weathering and to obtain
190 information relating to relative exposure ages for rock surfaces on the basis of rebound values, R (Aydin and
191 Basu, 2005; Goudie, 2006). A total of eighty-eight test sites were sampled on the fault plane using a Proceq
192 SilverSchmidt ST-PC. Each site was sampled twelve times in a direction perpendicular to its surface. Of these
193 twelve samples, the uppermost and lowermost values were disregarded, according to standard sampling
194 protocol, and the remaining ten were used to calculate the rebound value. These R values were processed in a
195 GIS. Initially, an orthophotograph of the fault scarp had to be created from a set of photoshots. The position of
196 each test site was recorded on a printed copy of the orthophotograph prior to image rectification in the GIS.
197 The relative positions of several test sites were measured in the field and used as reference points during
198 georeferencing. Each test site is represented by a point placed approximately in its centre and then the
199 calculated R value was added to each test site. Interpolation of these values indicates changes in the relative
200 surface hardness across the exposed part of the fault scarp. Several interpolation algorithms were tested but
201 the character of the data led us to select the natural neighbour technique.
202
203 3.2 *Petrographic and microstructural analyses*
204 Petrographic analyses of the sampled rocks were performed at the Institute of Rock Structure and Mechanics
205 CAS and the Institute of Geology CAS in Prague. Optical microscopy was conducted using the polarisation
206 microscope Leica DMR while chemical analysis of the primary and accessory minerals was conducted using the
207 electron microprobe CAMECA SX-100. Microstructural investigations have been made through the application
208 of optical microscopy, scanning electron microscopy (SEM), and energy dispersive spectroscopy (EDS). These
209 investigations were made at the University of Vienna. Thin sections were cut perpendicular to the shear plane
210 and parallel to the direction of sliding prior to mechanical polishing to thicknesses of c. 30 μm. Optical
211 microscopy was conducted using the polarisation microscope Leica DM4500 P with micrographs obtained
212 under both plane polarised light (PPL) and crossed polarised light (XPL). Selected samples were carbon coated
213 for SEM. The SEM imagining was conducted using a FEI Inspect S with an accelerating voltage of 10-15 kV for
214 spot sizes of 5-7. Images were obtained and presented in the back scattered mode (BSE). Element energy

dispersive spectroscopy was also conducted to better understand the chemical effects of fault slip. The EDAX EDS systems were used as an add-on to the FEI Inspect S. Using the TEAM™ Software Suite and Smart Phase Mapping it was possible to collect spectra and generate phase maps showing elemental distribution and associated spectra. The EDS operating conditions were 15 kV accelerating voltage for spot size of 5, at resolution of 514 x 514, dwell 200 µs.

3.3 *Cosmogenic radionuclide dating*

Cosmogenic radionuclide dating constrains the amount of time a rock has been situated at or near the surface of the Earth (e.g. Lal, 1991). Normal fault planes represent ideal objects for this dating technique as the incoming cosmic rays are only able to penetrate the progressively exposed parts of the fault (e.g. Palumbo et al., 2004). The basaltic lithologies of El Hierro determine that the most suitable cosmogenic nuclide with which to constrain periods of fault activity is ^{3}He (e.g. Kurz, 1986; Poujol et al., 2014). The sampling strategy aimed, first, to obtain samples from the least eroded parts of the fault and, second, to avoid obtaining samples from the whitish part of the fault plane as this was known to have been exposed during road construction. Five samples were collected from two profiles along the footwall (Figure 2). These samples range in thickness from two to five centimetres and belong to the same basaltic sequence that erupted 1.05±0.02 Ma (Carracedo et al., 2001). Samples were crushed and sieved to isolate fractions of less than 0.25 mm, 0.25-0.5 mm, and 0.5-2.0 mm. Several physical separation techniques including magnetic separation and density separation were used to isolate pure olivine and pyroxene phenocrysts.

All helium analyses were performed in the noble gas platform of the Centre de Recherches Pétrographiques et Géochimiques in Nancy. Samples were fused *in vacuo* at 1600°C for 15 minutes using the new custom designed metal induction furnace of CRPG (Zimmermann et al., 2018). Typical furnace blanks were $(1.9\pm0.6) \times 10^{-19}$ and $(5\pm4) \times 10^{-15}$ mol.g^{-1} for ^{3}He and ^{4}He, respectively, which represented an average of 1 % and 0.1 % of the ^{3}He and ^{4}He concentrations measured in the samples, respectively. The extracted gas then underwent standard gas purification (Blard et al., 2015). Helium was cryofucused at 8K before being released at 70K and introduced into the Split Flight Tube mass spectrometer, a Nier source static mass spectrometer optimised for the analysis of cosmogenic nuclides (Protin et al., 2016). The linearity of the mass spectrometer was carefully established by analysing standard splits with similar ^{4}He pressure to those of the samples. During the one-month analytical

period the observed reproducibility of the system was 2 % at 1σ, for both ^{3}He and ^{4}He. Furthermore, during this one-month period, two CRONUS-P pyroxene standards were analysed. These yielded ^{3}He concentrations of $(4.86\pm0.14) \times 10^{9}$ at.g^{-1} and $(5.01\pm0.14) \times 10^{9}$ at.g^{-1}. Both values stand within the internationally recognised error limits for this material (Blard et al., 2015). To determine the $^{3}He/^{4}He$ ratio of the magmatic component step crushing *in vacuo* was conducted on 0.5 mm to 2 mm olivines and pyroxenes obtained from Sample 5III (1^{st} step: 100 strokes, 1 min; 2^{nd} step: 500 strokes, 5 mins; Table 1). Crushing blanks were $(3\pm2) \times 10^{4}$ and $(7\pm2) \times 10^{9}$ for ^{3}He and ^{4}He, respectively. This represented 1 % and 4 % of the ^{3}He and ^{4}He analysed during the second crushing step.

To determine cosmogenic ^{3}He concentrations it was necessary to correct the melted ^{3}He concentrations ($^{3}He_{melt}$) from the nucleogenic ($^{3}He_{nucleo}$) and the magmatic ($^{3}He_{mag}$) components:

$$^{3}He_{cos} = {}^{3}He_{melt} - {}^{3}He_{nucleo} - {}^{3}He_{mag}$$

With:

$$^{3}He_{nucleo} = P_{3nuc} \times T_{eruption,}$$

P_{3nuc} is the production rate of nucleogenic ^{3}He. In this study, a value of 6×10^{-3} at.g^{-1}.a^{-1} has been used, computed using the equations of Andrews (1985) and the chemical composition measured in the phenocrysts and bulk rock samples (Supp. Table A). Combined with a value of 1.05 ± 0.02 Ma for $T_{eruption}$, based on the K-Ar age of the San Andrés basalt presented in Carracedo et al. (2001), this yielded a value of $(6\pm3) \times 10^{3}$ at.g^{-1} for $^{3}He_{nucleo}$.

In theory, the magmatic ^{3}He component has to be computed following this equation from Blard and Farley (2008):

$$^{3}He_{mag} = (^{4}He_{melt} - {}^{4}He_{rad}) \times (^{3}He/^{4}He)_{crush}$$

With

$^{4}He_{rad} = P_{4rad} \times T_{eruption,}$

P_{4rad} being the radiogenic ^{4}He production rate in the analysed olivines and pyroxenes. P_{4rad} is computed using the equations of Blard and Farley (2008) and the U, Th, and Sm concentrations measured in samples COS4-I and COS5-II (Supp. Table A). Using the 1.05±0.02 Ma value for $T_{eruption}$, this yields $^{4}He_{rad}$ theoretical concentrations ranging from 1.2×10^{12} at.g^{-1} to 4.1×10^{12} at.g^{-1}.

Such $^{4}He_{radio}$ concentrations are similar to the total ^{4}He concentrations measured by fusing the samples, which range from 6.2×10^{12} at.g^{-1} to 1.36×10^{13} at.g^{-1}, for an average of $(3.3\pm4.6)\times10^{12}$ at.g^{-1}.

Thus the outlined approach for estimating $^{4}He_{rad}$ represents the main source of uncertainty when computing the magmatic ^{3}He correction and, in turn, the main source of uncertainty when computing the final cosmogenic ^{3}He concentrations.

Instead, we decided to apply the following approach and compute a minimal and a maximal value for the cosmogenic ^{3}He concentrations, as follow (Table 1):

$^{3}He_{cos\ min} = {}^{3}He_{cos\ min} - {}^{3}He_{nucleo} - {}^{3}He_{crush\ mag,}$

assuming that $^{3}He_{crush\ mag}$ is the magmatic ^{3}He concentration from the prolonged crushing $(4.3\pm2.0)\times 10^{6}$ at.g^{-1}

$^{3}He_{cos\ max} = {}^{3}He_{cos\ min} - {}^{3}He_{nucleo}$

$^{3}He_{cos\ min}$ concentrations range from less than 2×10^{6} at.g^{-1} to $(1.19\pm0.20) \times 10^{7}$ at.g^{-1} while $^{3}He_{cos\ max}$ range from $(2.22\pm2.04) \times 10^{6}$ at.g^{-1} to $(2.17\pm0.21) \times 10^{7}$ at.g^{-1}.

Finally, $^{3}He_{cos}$ exposure ages were computed using the CREp calculator (crep.crpg.cnrs-nancy.fr), with the world averaged ^{3}He production rate, the standard atmosphere, and the Lal-Stone time dependent model (Martin et al., 2017). The production rate was computed taking into account the spatial characteristic of the samples, including self-shielding (Table 1).

4. Results

4.1 *Field data and structural analyses*

The NE section of the San Andrés Fault outcrop is morphologically well preserved while its SW section has been smoothed as a result of weathering and incurred some damage during road construction. In general, the exposed fault plane is straight with an orientation of approximately 170/70° (dip direction/dip angle). Only some irregularities can be observed such as two remarkable fault plane undulations protruding from its surface, with widths of up 4 m, separated by a parallel depression (Figure 3A-B). These irregularities were also recognised during structural geological measurements. In greater detail, it has been possible to identify numerous linear features, which have been grouped into three families on the basis of their character and orientation (Figure 3A-C). First, a family of centimetre to metre scale striations were identified on the basis of structural measurements and from the slope gradient maps. These striations cover most of the outcrop but are best preserved on the fault plane undulations. Most commonly, the striations plunge with azimuths of 125° and 131°. Second, a family of smooth elongated undulations and strongly elongated protrusions were also identified on the basis of structural measurements and from the slope gradient maps. These features are best seen in the northeastern section of the fault plane. The undulations and protrusions plunge with an azimuth of 111°. Third, a family of very smooth, spatially limited, slightly elongated protrusions were identified from the fault perpendicular slope gradient map. These are found in the lower SW and upper NE part of the 4 m wide fault plane undulation as well as at the crest of the other undulation protruding from surface to the NE. The protrusions plunge with an azimuth of 158°.

A photomosaic offering a perpendicular view of the fault outcrop overlain by a raster of interpolated R values is presented on Figure 4. Proportional plots illustrate the spatial variability in rock hardness across the outcrop. In general, higher R values have been measured on the lower and right side of the fault outcrop than have been measured on its upper and left side. The highest R values, indicating the least weathering, have been recorded

330 in the lowermost part of the fault outcrop on its right side (R > 50). This finding is not surprising given that the
331 hard whitish surface was exposed only recently during construction of the road. High R values have also been
332 recorded on the far left side of the fault outcrop (R > 40). This finding is more surprising but it can be explained
333 by several tens of centimetres of erosion on the fault surface and the presence of harder basalt blocks within
334 the tectonic breccia. Conspicuously low R values have been recorded in a wedge-shaped zone between 23 m
335 and 26 m (R < 25). Here a rather soft gouge material is attached to the fault surface and the vegetation cover
336 descends much lower than elsewhere – this suggests that chemical and biological weathering processes are
337 more intense in this area.
338
339 4.2 *Petrographic analyses*
340 The host rock basanites are fine grained basic rocks (samples PET3 and PET4). These rocks contain mainly
341 pyroxene, plagioclase, olivine, amphibole and volcanic glass, together with the accessory minerals (apatite,
342 chromite, magnetite, and Ti-magnetite). The pyroxene is represented by diopside. The plagioclases are usually
343 zoned with a basic core ($An_{79–83}$) and acid rim ($An_{45–70}$). Olivine occurs only in basanites with subordinate
344 amounts of volcanic glass. The olivine is enriched by forsterite component (75-80 mol. %). The amphibole is
345 represented by magnesiohornblende to hornblende tschermakite. The texture of the groundmass is mostly
346 ophitic and gives no indication of a pre-existing preferred fabric orientation. The tectonic breccias sampled
347 from the fault plane are composed of fragments of volcanic rock (up to several centimetres), cemented by a
348 very fine grained groundmass containing abundant fragments of the original volcanic rock (millimetres to
349 centimetres on samples PET1 and PET2). The higher proportion of fine grained Fe-oxides and Fe-hydroxides
350 imparts a rusty colour of these tectonic breccias. However, the volume of Fe-oxides and Fe-hydroxides is highly
351 variable, with significant enrichment in the fine grained groundmass of the original volcanic rock. The tectonic
352 breccias are cross-cut by zeolite veins in a range of orientations and sizes. Frictionite, or landslide
353 pseudotachylyte, was found in samples obtained directly from the fault plane (Figure 2). This is composed of
354 relict frictional melt and material similar to tectonic breccia (Figures 5-7).
355
356 4.3 *Microstructural analyses*
357 The NE part of the fault outcrop is covered by a whitish layer which attains a maximum thickness in the order
358 of several centimetres. Figure 2 shows examples of the whitish layer that overlies the grey cataclasite and

359 microbreccias. In some cases this whitish layer comes into direct contact with tectonic breccia. The tectonic
360 breccia is highly oxidised (Figure 2D, F). Brecciation intensity increases from the undeformed basanite to the
361 more deformed breccia, i.e. towards the fault surface. This breccia may be the product of an earlier slip event.
362 However, here we focus on the cataclasite and the whitish layer, i.e. those layers that overlie the tectonic
363 breccia. Using optical microscopy, it is possible to differentiate two distinct layers within the frictionite by their
364 composition and microstructure: a structurally lower cataclasite and a structurally higher silica layer.
365
366 The cataclasite cuts the tectonic breccia while in places it is cut by the silica layer. Contact with the host rock is
367 characterised by a sharp boundary that is observed in both hand samples and optical micrographs (Figure 6).
368 Although the cataclasite is grey in hand samples, it is dark brown in optical micrographs (Figure 6A, B) while the
369 sharpness of the contact is accentuated by the truncation of several clasts (Figures 6 & 7). The main
370 characteristics of this layer are grain size reduction and P- foliation, terminology of Passchier and Trouw, 2005).
371 The zones of grain size reduction, in which grain sizes range from c. 10 μm to c. 100 μm, are defined by P- and
372 Y- shears (Figure 6B, D). A dextral sense of shear is indicated by the P- and Y- shears along with a winged
373 inclusion visible in the optical micrographs (Figure 6A, B). This finding is consistent with structural observations
374 made at the outcrop scale. Elemental maps highlight the similarity between the composition of the host rock
375 and the composition of the cataclasite (Figure 6E, F). Moreover, this similarity is accentuated by the apparent
376 resemblance in composition of a truncated clast, itself in contact with the cataclasite (Figure 6E, F). A second
377 cataclasite has a more lensoid shape which is apparently defined by P- and Y- shears (Figure 7). It exhibits
378 strong P-foliation which is seen most readily in the elemental maps (Figure 7C, E). In addition, cracks within this
379 layer are parallel to both the Y-shear, and the slip surface, and are filled with silica (Figure 7E).
380
381 The silica layer cuts both the tectonic breccia and the cataclastic layer. The boundary between the silica layer
382 and the subjacent rocks is a sharp, single line, which crosscuts foliation in the cataclasite and truncates clasts in
383 the tectonic breccia. The boundary between the cataclasite layer and the silica layer is sometimes marked by
384 shiny sublayers that parallel the boundary (Figure 6B, H) and exhibit a high interference colour when seen
385 under cross polarised light with a gypsum tint plate (Figure 5C). There is no indication of mixing between the
386 cataclasite and the silica layer across the boundary separating these layers. The silica layer appears to be
387 translucent, white to pale coloured under plane polarised light (Figures 5-7). It is composed of a

388 microcrystalline to amorphous silica matrix with a thickness of c. 250 µm to 350 µm. The architecture varies:
389 the matrix consists of an inclusionless silica material that develops into complex structures with flow bands
390 (Figures 5-7), cataclastic sublayers (Figure 5H), and clast-cortex aggregates (Figure 6G, I). Flow bands, which
391 vary in thickness from c. 25 µm to c. 110 µm, correspond to P- and Y- shears in the cataclastic layer fabric and
392 are characterised by a change in the amount of Mg (Figure 5L and Figure 6C, D). Cataclasite sublayers form
393 lenticular shapes (Figure 5H). These sublayers appear to have a similar composition to the cataclasite layer but
394 with a finer grain size and present evidence of material mixing with the silica layer. Some clasts embedded in
395 the silica layer have a cortex, or armour, and these are referred to as clast-cortex aggregates. The clast-cortex
396 aggregates vary in size, from c. 90 µm to 290 µm, complexity, and composition. Those clasts within the
397 aggregates consist of fragments of adjacent rock (Figure 7G) or silica matrix (Figure 6I). A complex cortex
398 texture with what appears to be several coatings has been observed (Figure 6G). Elemental maps show that the
399 cortex composition varies as well (e.g. Figure 6L and Figure 7D, E). It is believed that a significant amount of the
400 cortex material was lost during preparation of the thin sections (e.g. Figure 6G-I).
401
402 4.4 *Cosmogenic radionuclide dating*
403 Cosmogenic ^{3}He exposure ages reveal significant differences between each of the two sampled profiles. Sample
404 COS1 has yielded a maximum exposure age of 21±20 ka while samples COS2 and COS3 have yielded a
405 maximum exposure age of 26±18 ka. Replicates of sample COS4 yielded exposure ages ranging from 21±19 to
406 61±19 ka while replicates of sample COS5 yielded exposure ages ranging from 52±17 to 183±17 ka (Table 1).
407 These results indicate that movement across the currently exposed portion of the fault plane occurred over a
408 short period of time as suggested by the fact that there is no gradual decrease in exposure ages from upper to
409 lower part of the two profiles.
410
411 The right hand profile (samples COS1-3) revealed exposures ages that are below the detection limit i.e. these
412 were exposed between 0 and 26 ka. These young exposure ages most probably reflect recent exhumation on
413 the right hand part of the fault owing to the fact that the right hand profile is separated from the left hand
414 profile by only 6-7 m. Intense erosion of the right hand profile can be excluded as the R values indicate much
415 greater hardness, i.e. less weathering, here than on the left hand profile.
416

417 The left hand profile (samples COS4 and COS5) revealed exposure ages between 21 and 183 ka. The higher
418 sample COS4 provides a younger age than the lower sample COS5. Under normal circumstances this should not
419 be possible – the highest parts of the fault should be exposed before its lower parts – and it suggests that the
420 higher sample has been subjected to weathering. Consequently sample COS5 offers the most reliable results as
421 it has neither been affected by weathering nor by recent exhumation. The high variability of computed
422 exposure ages between the replicate in this sample is due to the considerable uncertainty associated with the
423 estimate of the magmatic ^{3}He component as outlined in Section 3.3. Nonetheless it is believed that the most
424 recent fault reactivation occurred between the calculated exposure ages of sample COS5 (52±17 to 183±17 ka).
425

426 **5. Interpretation and discussion**

427 5.1 *Landslide displacement direction*

428 Distinct families of linear and elongated features at the fault plane evidence past behaviour of the rock mass
429 (Sagy et al., 2007). Two major slip events are interpreted to have occurred on the studied fault plane on the
430 basis of the relative position and general morphology of such features. The older phase is represented by the
431 family of smooth elongated undulations and strongly elongated bumps, best preserved in the depressions and
432 flats in the northeastern section of the fault plane, which have a plunge direction of 111°. During this phase the
433 rock mass moved towards the ESE. The younger phase is represented by the other two families of linear and
434 elongated features. The onset of this phase is interpreted to have commenced with minor, most probably slow
435 displacement towards the SSE. Support for this is gleaned from the smooth, spatially limited, elongated bumps
436 which have a plunge direction of 158°. The displacement rate is then interpreted to have accelerated as the
437 rock mass moved more towards the SE. Support for this is gleaned from the centimetre to metre scale
438 striations which cover most of the fault outcrop and have plunge directions of 125° and 131°. The general
439 appearance of these features is sufficiently similar to assume that they developed during a single slip phase. It
440 is supposed that this shift in the displacement direction, from the SSE to the SE, can be explained by either a
441 sudden change in the geometry of the slip surface or a fundamental change in the morphology of the entire
442 volcanic edifice. It is known that El Hierro underwent a clockwise rotation of 15°, beginning around 440 ka
443 (Széréméta et al., 1999), and it has been suggested that this rotation could be associated with activity on the
444 San Andrés Landslide and the debris avalanche Las Playas I (Carracedo, 2008).
445

446 5.2 *Fault related microstructures and dynamic rock reworking*

447 The microstructures seen on the surface of the San Andrés Fault are believed to be a result of fast slip,
448 associated with frictional heating and partial melting during landslide emplacement. The first line of evidence
449 for flash heating during flank collapse is observed in both hand samples and polished slabs as heat diffused in
450 the underlying material: the adjacent host rock and tectonic breccia exhibits increasing level of oxidisation
451 towards the fault surface. This is similar for pseudotachylytes reported from the Köfels landslide (Masch et al.,
452 1985) and from the Arequipa volcanic landslide deposit in Peru (Legros et al., 2000). The second line of
453 evidence comes from the crosscutting relationships between either the host rock or the tectonic breccia and
454 the deformation layers. All of the observed contacts are sharp and accentuated by multiple truncated clasts.
455 This type of crosscutting relationship indicates fast displacement and is often considered a strong indication of
456 a seismic slip (Passchier and Trouw, 2005; Price et al., 2012; Smeraglia et al., 2017). The third line of evidence
457 comes from the boundary between the silica layer and the adjacent rocks. This boundary is characterised by
458 shiny bands that exhibit a high interference colour under cross polarised light and a positive optical sign under
459 cross polarised light using a gypsum tint plate. These bands are tentatively interpreted as recrystallised
460 material resulting from frictional melting but further analyses are needed to confirm this supposition.
461
462 The cataclastic layer exhibits P-foliation, grain size reduction, and the development of winged clasts in a
463 heterogeneous matrix. The winged clast presented in Figure 5 resembles those of Grasemann and Dabrowski
464 (2015) and Grasemann et al. (2019). The foliation developed within this layer is typical of brittle deformation,
465 with Y- shears parallel to the slip surface, and P-shears inclined relative to the slip surface (i.e. Figure 5I). This
466 type of foliation cannot be used as an indicator for fast slip as it is recorded in association with both seismic
467 and creep phenomena (Verberne et al., 2013; Smeraglia et al., 2017). However, unequivocal evidence for fast
468 slip, instead of progressive creep, is provided by the fact that the contact between the cataclastic layer and the
469 adjacent rock is sharp and accentuated by multiple truncated clasts. The cataclasite architecture is similar to
470 those described in other volcanic pseudotachylytes (Lavallée et al., 2012, 2014; Kendrick et al., 2012, 2014) as
471 well as to that described in seismically deformed limestones (Smith et al., 2011). Therefore, it is necessary to
472 define this cataclastic layer as frictionite *sensu lato*, as it was almost certainly emplaced during catastrophic
473 landslide emplacement but there is no decisive proof of flash heating.
474

475 In contrast, the silica layer is defined as frictionite *sensu stricto*, as it is comparable to traditional
476 pseudotachylytes (e.g. Passchier and Trouw, 2005; Price et al., 2012; Rowe and Griffith, 2015). Here a list of
477 particularly pertinent features is presented with reference to the identification criteria for deformed
478 pseudotachylytes (Passchier and Trouw, 2005; Price et al., 2012):
479
480 i. *Crosscutting relationships with sharp layer boundaries.* The silica layer cuts the cataclasite
481 foliation and the boundaries are accentuated by clast truncation and presence of shiny bands
482 which have been interpreted as recrystallised material from frictional melting. Analogous
483 microstructural features have been reported from numerous natural and experimental cases of
484 seismic slip (e.g. Fondriest et al., 2013; Smeraglia et al., 2017; Tesei et al., 2017).
485
486 ii. *The presence of fragments of host rock.* Fragments of adjacent rock appear as isolated islands and
487 vary in size, shape, and complexity. The more complex clasts have an encasing cortex, or armour,
488 and are referred to as clast-cortex aggregates. Typically, those fragments described here have a
489 volcanic clast in the core, cataclastic material in the rim, and they parallel the foliation. In a
490 number of senses, they are similar to “armoured clasts” or “accretionary rounded grains” (Anders
491 et al., 2010; Rowe et al., 2012; Kirkpatrick et al., 2013) and clay-clast aggregates (Boutareaud et
492 al., 2008; Han et al., 2011). The main differences are the ratio between the clast and the rim and
493 their composition. The rims described here appear to be wider than previously reported while
494 they are neither composed of clay nor any other mineral assemblage. Consequently, the clast-
495 cortex aggregates presented in this study are most readily comparable to the accretionary
496 rounded grains described from the Corona Heights Fault (Kirkpatrick et al., 2013).
497
498 iii. *The presence of an ultra-fine grained matrix.* The silica layer comprises a homogenous silica
499 matrix, ultra-fine grained to amorphous, which is very similar to silica gel (Kirkpatrick et al., 2013;
500 Faber et al., 2014) and amorphous nanopowder (Rowe et al., 2019). More detailed studies are
501 needed in order to measure the amount of water and crystalline material that occurs in this
502 matrix. The presence of new grains that have grown in the voids or bubbles indicates that at least
503 some of this matrix must be crystalline.

iv. *Inherited compositional variations from flow structures.* Flow bands in the silica layer are defined by optical and compositional variations. Optical variations are evident as shiny bands and they can be traced along the whole length of the layer. The flow bands are structurally controlled, as they parallel the P- and Y- shears, and they localise clasts and clast-cortex aggregates as well as Mg-enriched material. Further analyses are needed to fully understand their origin. Similar to these flow bands are the cataclastic sublayers, which are also structurally controlled, but with evidence for the reworking of cataclastic material. This feature, together with presence of clast-cortex aggregates is interpreted as fluidised granular flow reported in many geologic settings (Boutareaud et al., 2008; Anders et al., 2010; Ujiie et al., 2011; Kirkpatrick et al., 2013). Furthermore, fluidised cataclasites have been suggested as a record of seismic slip rates (Brodsky et al., 2009; Rowe et al., 2005).

v. *Differences between the matrix and host rock mineral assemblages.* The most conspicuous difference between the silica layer and the adjacent rocks is in the mineral assemblage. The homogenous silica layer contrasts greatly with the polymineralic cataclasite and the host rock. Even though the silica layer can be assumed to be a product of hydrothermal fluid deposition, the presence of kinematic indicators such as shears and flow bands consistent with observations at the outcrop scale, indicate that the silica layer was formed as a product of frictional slip. Silica has been reproduced in fast slip experiments (e.g. Di Toro et al., 2011; Kirkpatrick et al., 2013; Rowe et al., 2019) and is considered to be a product of frictional wear that weakens the fault, acting as a lubricant (Rowe et al., 2019).

5.3 *Conceptual model for the San Andrés Landslide*

A conceptual model for the development of the San Andrés Landslide is proposed here on the basis of the findings presented in this study and age estimates presented elsewhere in the published literature (Figure 8). The first slip event as evidenced by the cataclastic layer is proposed to have occurred between 545 ka and 430 ka. The lower limit for fault activity is defined by the onset of volcanism associated with the El Golfo Series (Guillou et al., 1996) while the upper limit for fault activity is defined by the onset of the clockwise rotation of

El Hierro (Széréméta et al., 1999). The second slip event as evidenced by the silica layer is proposed to have occurred between 183 ± 17 and 52 ± 17 ka based on the presented cosmogenic ^{3}He exposure dates. This age range spans termination of volcanism associated with the El Golfo-Las Playas Unit and the onset of volcanism associated with the Rift Series at 145 ka (Guillou et al., 1996). The lower limit for fault activity broadly relates to the probable timing of the debris avalanches El Golfo A, between 176 ka and 133 ka, and Las Playas II, between 176 ka and 145 ka. Moreover, the upper limit for fault activity broadly relates to the probable timing of the debris avalanche El Golfo B, between 87 ka and 39 ka. Thus, it is believed that the factor, or factors, which triggered one of these giant debris avalanches may have triggered the second slip event described in this study but no other data have yet been found to support this hypothesis. In addition, a conceptual model is presented for the development of the surface of the San Andrés Fault (Figure 9). The developmental model outlined here is broadly consistent with the findings of Day et al. (1997). In that study, it was suggested that the minimum age of the San Andrés Fault should be between 250 ka and 150 ka and that the fault could have been active only for a geologically short period of less than 400 ka. Their assertions are based on a younger undisturbed lava flow which covers the southern part of the fault.

6. Conclusions

In this study the fault plane of the San Andrés Landslide on El Hierro in the Canary Islands has been investigated through a combination of geological and geomorphological measurements, petrological and mineralogical analyses, and cosmogenic ^{3}He exposure dating.

- The fault surface is composed of a striated frictionite which is in contact with a highly oxidised tectonic breccia. The tectonic breccia transitions into the underlying undeformed basanite host rock. Microstructural analysis of the frictionite has revealed two distinct layers: a dark heterogeneous cataclastic layer and a translucent silica layer with a thickness of up to 1 cm.
- The architecture of the samples and the observed crosscutting relationships suggest that the cataclasite layer and the silica layer represent two separate slip events associated with seismic rupture during landslide emplacement. Moreover, the notion of two distinct slip phases is supported by kinematic markers etched on the fault surface.

- This information – coupled with the cosmogenic exposure dating and knowledge about the geological history of the island – forms basis of a conceptual model for the development of the San Andrés Landslide. The first slip event, represented by the cataclastic layer, is thought to have occurred between 545 ka and 430 ka while the second slip event, represented by the silica layer, is thought to have occurred between 183 ± 17 and 52 ± 17 ka.

This is the first time that more than one slip event has ever been recognised on a single fault plane resulting from volcanic flank collapse on an oceanic island. It suggests that the possibility of reactivating supposedly inactive fault structures may be far greater than hitherto assumed. This is a key finding, which may lead to re-evaluation of the threats related to volcanic islands collapses. Furthermore, it is believed that this is the first time a silica layer resulting from frictional melt has been described from a volcanic setting.

Acknowledgements

Bernhard Grasemann, Rostislav Melichar, Gerlinde Habler, and Jackie Kendrick are thanked for stimulating and insightful discussions regarding our results and their interpretation. We are also grateful to the two reviewers and the editor for significantly improving the clarity of this manuscript.

Funding sources

This study was supported by the Czech Science Foundation [Project GJ16-12227Y], by the OP VVV project CzechGeo EPOS-Sci No. CZ.02.1.01/0.0/0.0 /16_013 /0001800 and the conceptual development research organisation of the Institute of Rock Structure and Mechanics CAS [RVO:67985891].

References

Agisoft LLC, 2014. Agisoft PhotoScan User Manual, Professional Edition, Version 1.1. Agisoft LLC, St. Petersburg, 78 pp.

Agliardi, F., Crosta, G., Zanchi, A., 2001. Structural constraints on deep seated slope deformation kinematics. Engineering Geology 59, 83-102. https://doi.org/10.1016/S0013-7952(00)00066-1

588 Ancochea, E., Barrera, J., Bellido, F., Benito, R., Brändle, J., Cebriá, J., Coello, J., Cubas, C., De la Nuez, J., Gómez,
589 J., 2004. Canarias y el vulcanismo neógeno peninsular. In: Vera, J. (Ed.), Geología de España. Sociedad
590 Geológica de España-Instituto Geológico y Minero de España, Madrid, pp 635-682.
591 Anders, M., Fouke, B., Zerkle, A., Tavarnelli, E., Alvarez, W., Harlow, G., 2010. The role of calcining and basal
592 fluidization in the long runout of carbonate slides: an example from the Heart Mountain Slide Block,
593 Wyoming and Montana, U.S.A. The Journal of Geology 118, 577-599. https://doi.org/10.1086/656383
594 Andrews, J., 1985. The isotopic composition of radiogenic helium and its use to study groundwater movement
595 in confined aquifers. Chemical Geology 49, 339-351. https://doi.org/10.1016/0009-2541(85)90166-4
596 Aydin, A., Basu, A., 2005. The Schmidt hammer in rock material characterization. Engineering Geology 81, 1-14.
597 https://doi.org/10.1016/j.enggeo.2005.06.006
598 Balek, J., Blahůt, J., 2017. A critical evaluation of the use of an inexpensive camera mounted on a recreational
599 unmanned aerial vehicle as a tool for landslide research. Landslides 14, 1217-1224.
600 https://doi.org/10.1007/s10346-016-0782-7
601 Becerril, L., Ubide, T., Sudo, M., Martí, J., Galindo, I., Galé, C., Morales, J., Yepes, J., Lago, M., 2016a.
602 Geochronological constraints on the evolution of El Hierro (Canary Islands). Journal of African Earth
603 Sciences 113, 88-94. https://doi.org/10.1016/j.jafrearsci.2015.10.012
604 Becerril, L., Galve, J., Morales, J., Romero, C., Sánchez, N., Martí, J., Galindo, I., 2016b. Volcanostructure of El
605 Hierro (Canary Islands). Journal of Maps 12, Supplement 1, 43-52.
606 https://doi.org/10.1080/17445647.2016.1157767
607 Benito-Saz, M., Parks, M., Sigmundsson, F., Hooper, A., García-Cañada, L., 2017. Repeated magmatic intrusions
608 at El Hierro Island following the 2011-2012 submarine eruption. Journal of Volcanology and Geothermal
609 Research 344, 79-91. https://doi.org/10.1016/j.jvolgeores.2017.01.020
610 Blahůt, J., Rowberry, M., Balek, J., Klimeš, J., Baroň, I., Meletlidis, S., Martí, X., 2017. Monitoring giant landslide
611 detachment planes in the era of big data analytics. In: Mikoš, M., Arbanas, Ž., Yin, Y., Sassa, K. (Eds.),
612 Advancing Culture of Living with Landslides, Volume 3. Springer, Cham, pp. 333-340.
613 https://doi.org/10.1007/978-3-319-53487-9_38
614 Blahůt, J., Klimeš, J., Rowberry, M., Kusák, M., 2018a. Database of giant landslides on volcanic islands - first
615 results from the Atlantic Ocean. Landslides 15, 823-827. https://doi.org/10.1007/s10346-018-0967-
616 3Blahůt, J., Baroň, I., Sokol, Ľ., Meletlidis, S., Klimeš, J., Rowberry, M., Melichar, R., García-Cañada, L.,

Martí, X., 2018b. Large landslide stress states calculated during extreme climatic and tectonic events on El Hierro, Canary Islands. Landslides 15, 1801-1814. https://doi.org/10.1007/s10346-018-0993-1

Blahůt, J., Balek, J., Klimeš, J., Rowberry, M., Kusák, M., Kalina, J., 2019. A comprehensive global database of giant landslides on volcanic islands. Landslides 16 (10), 2045-2052. https://doi.org/ 10.1007/s10346-019-01275-8

Blard, P.-H., Balco, G., Burnard, P., Farley, K., Fenton, C., Friedrich, R., Jull, A., Niedermann, S., Pik, R., Schaefer, J., Scott, E., Shuster, D., Stuart, F., Stute, M., Tibari, B., Winckler, G., Zimmermann, L., 2015. An inter-laboratory comparison of cosmogenic ^{3}He and radiogenic ^{4}He in the CRONUS-P pyroxene standard. Quaternary Geochronology 26, 11-19. https://doi.org/10.1016/j.quageo.2014.08.004

Blard, P.-H., Farley K., 2008. The influence of radiogenic ^{4}He on cosmogenic ^{3}He determinations in volcanic olivine and pyroxene. Earth and Planetary Science Letters 276, 20-29. https://doi.org/10.1016/j.epsl.2008.09.003

Boutareaud, S., Calugaru, D.-G., Han, R., Fabbri, O., Mizoguchi, K., Tsutsumi, A., Shimamoto, T., 2008. Clay-clast aggregates: a new textural evidence for seismic fault sliding? Geophysical Research Letters 35, L05302. https://doi.org/10.1029/2007GL032554

Brodsky, E., Rowe, C., Meneghini, F., Moore, J., 2009. A geological fingerprint of low viscosity fault fluids mobilized during an earthquake. Journal of Geophysical Research, Solid Earth 114, B01303. https://doi.org/10.1029/2008JB005633

Carracedo, J.-C., 2008. Canarian Volcanoes IV: La Palma, La Gomera, El Hierro. Editorial Rueda S.L., Madrid, 213 pp.

Carracedo, J.-C., Day, S., Guillou, H., Pérez Torrado, F., 1997. Geology of the island of El Hierro, Canary Islands: stratigraphy, volcanology, and structure. Excursion Guidebook, International Workshop on Volcanism and Volcanic Hazards in Immature Intraplate Oceanic Islands, La Palma, 43 pp.

Carracedo, J.-C., Day, S., Guillou, H., Pérez Torrado, F., 1999. Giant quaternary landslides in the evolution of La Palma and El Hierro, Canary Islands. Journal of Volcanology and Geothermal Research 94, 169-190. https://doi.org/10.1016/S0377-0273(99)00102-X

Carracedo, J.-C., Rodríguez Badiola, E., Guillou, H., De la Nuez, H., Pérez Torrado, F., 2001. Geology and volcanology of the western Canaries: La Palma and El Hierro. Estudios Geológicos 57, 171-295.

Carracedo, J.-C., Troll, V., 2016. The Geology of Canary Islands. Elsevier, Amsterdam, 622 pp.

646 Day, S., Carracedo, J.-C., Guillou, H., 1997. Age and geometry of an aborted rift flank collapse: the San Andres
647 fault system, El Hierro, Canary Islands. Geological Magazine 134, 523-537.
648 https://doi.org/10.1017/S0016756897007243
649 De Blasio, F., Elverhøi, A., 2008. A model for frictional melt production beneath large rock avalanches. Journal
650 of Geophysical Research, Earth Surface 113, F02014. https://doi.org/10.1029/2007JF000867
651 Di Toro, G., Han, R., Hirose, T., De Paola, N., Nielsen, S., Mizoguchi, K., Ferri, F., Cocco, M., Shimamoto, T., 2011.
652 Fault lubrication during earthquakes. Nature 471, 494-499. https://doi.org/10.1038/nature09838
653 Duffield, W., 1975. Structure and origin of the Koae Fault System, Kilauea Volcano, Hawaii. United States
654 Geological Survey, Professional Paper 856, 12 pp.
655 Faber, C., Rowe, C., Miller, J., Fagereng, Å., Neethling, J., 2014. Silica gel in a fault slip surface: field evidence for
656 palaeo-earthquakes? Journal of Structural Geology 69 108-121.
657 https://doi.org/10.1016/j.jsg.2014.09.021
658 Fondriest, M., Smith, S., Candela, T., Nielsen, S., Mair, K., Di Toro, G., 2013. Mirror-like faults and power
659 dissipation during earthquakes. Geology 41, 1175-1178. https://doi.org/10.1130/G34641.1
660 Gomberg, J., Bodin, P., Savage, W., Jackson, M., 1995. Landslide faults and tectonic faults, analogs? The
661 Slumgullion earthflow, Colorado. Geology 23, 41-44. https://doi.org/10.1130/0091-
662 7613(1995)023<0041:LFATFA>2.3.CO;2
663 Gómez Sainz de Aja, J., Klein, E., Ruiz García, M., Balcells Herrera, R., Del Pozo, M., Galindo, E., La Moneda, E.,
664 2010. Mapa Geológico de España, Escala 1:25 000, Valverde (Isla de El Hierro), Hoja N° 1105-II,
665 Memoria. Instituto Geológico y Minero de España, Madrid, 96 pp.
666 Goudie, A., 2006. The Schmidt hammer in geomorphological research. Progress in Physical Geography 30, 703-
667 718. https://doi.org/10.1177/0309133306071954
668 Grasemann, B., Dabrowski, M., 2015. Winged inclusions: pinch-and-swell objects during high-strain simple
669 shear. Journal of Structural Geology 70, 78-94. https://doi.org/10.1016/j.jsg.2014.10.017
670 Grasemann, B., Dabrowski, M., Schöpfer, M., 2019. Sense and non-sense of shear reloaded. Journal of
671 Structural Geology 125, 200-228. https://doi.org/10.1016/j.jsg.2018.05.028
672 Guillou, H., Carracedo, J.-C., Pérez Torrado, F., Rodríguez Badiola, E., 1996. K-Ar ages and magnetic stratigraphy
673 of a hotspot-induced, fast grown oceanic island: El Hierro, Canary Islands. Journal of Volcanology and
674 Geothermal Research 73, 141-155. https://doi.org/10.1016/0377-0273(96)00021-2

675 Han, R., Hirose, T., 2012. Clay-clast aggregates in fault gouge: an unequivocal indicator of seismic faulting at
676 shallow depths? Journal of Structural Geology 43, 92-99. https://doi.org/10.1016/j.jsg.2012.07.008
677 Han, R., Hirose, T., Shimamoto, T., Lee, Y., Ando, J., 2011. Granular nanoparticles lubricate faults during seismic
678 slip. Geology 39, 599-602. https://doi.org/10.1130/G31842.1
679 Hildenbrand, A., Marques, F., Catalao, J., Catita, C., Costa, A., 2012. Large scale active slump of the
680 southeastern flank of Pico Island, Azores. Geology 40, 939-942. https://doi.org/10.1130/G33303.1
681 Hunt, J.E., Wynn, R.B., Talling, P.J., Masson, D.G., 2013. Multistage collapse of eight western Canary Island
682 landslides in the last 1.5 Ma: Sedimentological and geochemical evidence from subunits in submarine
683 flow deposits. Geochemistry Geophysics Geosystems 14(7), 2159-2181. https://doi.org/
684 10.1002/ggge.20138
685 Hunt, J.E., Cassidy, M., Talling, P.J., 2018. Multi-stage volcanic island flank collapses with coeval explosive
686 caldera-forming eruptions. Scientific Reports 8, 1146. https://doi.org/10.1038/s41598-018-19285-2
687 Jaboyedoff, M., Penna, I., Pedrazzini, A., Baroň, I., Crosta, G., 2013. An introductory review on gravitational
688 deformation induced structures, fabrics, and modeling. Tectonophysics 605, 1-12.
689 https://doi.org/10.1016/j.tecto.2013.06.027
690 Karstens, J., Berndt, C., Urlaub, M., Watt, S.F.L., Micallef, A., Ray, M., Klaucke, I., Muff, S., Klaeschen, D., Kühn,
691 M., Roth, T., Böttner, C., Schramm, B., Elger, J., Brune, S., 2019. From gradual spreading to catastrophic
692 collapse – Reconstruction of the 1888 Ritter Island volcanic sector collapse from high-resolution 3D
693 seismic data. Earth and Planetary Science Letters 517, 1-13. https://doi.org/10.1016/j.epsl.2019.04.009
694 Kendrick, J., Lavallée, Y., Ferk, A., Perugini, D., Leonhardt, R., Dingwell, D., 2012. Extreme frictional processes in
695 the volcanic conduit of Mount St. Helens (USA) during the 2004-2008 eruption. Journal of Structural
696 Geology 38, 61-76. https://doi.org/10.1016/j.jsg.2011.10.003
697 Kendrick, J., Lavallée, Y., Hess, K.-U., De Angelis, S., Ferk, A., Gaunt, H., Meredith, P., 2014. Seismogenic
698 frictional melting in the magmatic column. Solid Earth 5, 199-208. https://doi.org/10.5194/se-5-199-
699 2014
700 Kirkpatrick, J., Rowe, C., White, J., Brodsky, E., 2013. Silica gel formation during fault slip: evidence from the
701 rock record. Geology 41, 1015-1018. https://doi.org/10.1130/G34483.1

Klimeš, J., Yepes, J., Becerril, L., Kusák, M., Galindo, I., Blahůt, J., 2016. Development and recent activity of the San Andrés Landslide on El Hierro, Canary Islands, Spain. Geomorphology 261, 119-131. https://doi.org/10.1016/j.geomorph.2016.02.018

Kurz, M., 1986. In situ production of terrestrial cosmogenic helium and some applications to geochronology. Geochimica et Cosmochimica Acta 50, 2855-2862. https://doi.org/10.1016/0016-7037(86)90232-2

Lal, D., 1991. Cosmic ray labeling of erosion surfaces: in situ nuclide production rates and erosion models. Earth and Planetary Science Letters 104, 424-439. https://doi.org/10.1016/0012-821X(91)90220-C

Lavallée, Y., Hirose, T., Kendrick, J., De Angelis, S., Petrakova, L., Hornby, A., Dingwell, D., 2014. A frictional law for volcanic ash gouge. Earth and Planetary Science Letters 400, 177-183. https://doi.org/10.1016/j.epsl.2014.05.023

Lavallée, Y., Mitchell, T., Heap, M., Vasseur, J., Hess, K.-U., Hirose, T., Dingwell, D., 2012. Experimental generation of volcanic pseudotachylytes: constraining rheology. Journal of Structural Geology 38, 222-233. https://doi.org/10.1016/j.jsg.2012.02.001

Legros, F., Cantagrel, J.-M., Devouard, B., 2000. Pseudotachylite (frictionite) at the base of the Arequipa Volcanic Landslide Deposit (Peru): implications for emplacement mechanisms. The Journal of Geology 108, 601-611. https://doi.org/10.1086/314421

León, R., Somoza, L., Urgeles, R., Medialdea, T., Ferrer, M., Biain, A., García-Crespo, J., Mediato, J., Galindo, I., Yepes, J., González, F., Gimenez-Moreno, J., 2017. Multi-event oceanic island landslides: new onshore-offshore insights from El Hierro Island, Canary Archipelago. Marine Geology 393, 156-175. https://doi.org/10.1016/j.margeo.2016.07.001

Liu, C., Lay, T., Xiong, X., 2018. Rupture in the 4 May 2018 M_W 6.9 earthquake seaward of the Kilauea East Rift Zone fissure eruption in Hawaii. Geophysical Research Letters 45, 9508-9515. https://doi.org/10.1029/2018GL079349

Longpré, M., Chadwick, J., Wijbrans, J., Iping, R., 2011. Age of the El Golfo debris avalanche, El Hierro (Canary Islands): new constraints from laser and furnace $^{40}Ar/^{39}Ar$ dating. Journal of Volcanology and Geothermal Research 203, 76-80. https://doi.org/10.1016/j.jvolgeores.2011.04.002

López, C., Blanco, M., Abella, R., Brenes, B., Cabrera Rodríguez, V., Casas, B., Domínguez Cerdeña, I., Felpeto, A., Fernández de Villalta, M., Del Fresno, C., et al., 2012. Monitoring the volcanic unrest of El Hierro (Canary

730 Islands) before the onset of the 2011-2012 submarine eruption. Geophysical Research Letters 39,
731 L13303. https://doi.org/10.1029/2012GL051846
732 Maddock, R., 1986. Frictional melting in landslide generated frictionites (hyalomylonites) and fault generated
733 pseudotachylytes: discussion. Tectonophysics 128, 151-153. https://doi.org/10.1016/0040-
734 1951(86)90316-1
735 Martin, L., Blard, P.-H., Balco, G., Lave, J., Delunel, R., Lifton, N., Laurent, V., 2017. The CREp program and the
736 ICE-D production rate calibration database: a fully parameterizable and updated online tool to compute
737 cosmic-ray exposure ages. Quaternary Geochronology 38, 25-49.
738 https://doi.org/10.1016/j.quageo.2016.11.006
739 Masch, L., Wenk, H., Preuss, E., 1985. Electron microscopy of hyalomylonites - evidence for frictional melting in
740 landslides. Tectonophysics 115, 131-160. https://doi.org/10.1016/0040-1951(85)90103-9
741 Masson, D., 1996. Catastrophic collapse of the volcanic island of Hierro 15 ka ago and the history of landslides
742 in the Canary Islands. Geology 24, 231-234. https://doi.org/10.1130/0091-
743 7613(1996)024<0231:CCOTVI>2.3.CO;2
744 Masson, D., Watts, A., Gee, M., Urgeles, R., Mitchell, N., Le Bas, T., Canals, M., 2002. Slope failures on the flanks
745 of the western Canary Islands. Earth-Science Reviews 57, 1-35. https://doi.org/10.1016/S0012-
746 8252(01)00069-1
747 McGuire, W., 1996. Volcano instability: a review of contemporary themes. In: McGuire, W., Jones, A., Neuberg,
748 J. (Eds.), Volcano Instability on the Earth and Other Planets. Geological Society of London, Special
749 Publication 110, 1-23. https://doi.org/10.1144/GSL.SP.1996.110.01.01
750 Meletlidis, S., Di Roberto, A., Domínguez Cerdeña, I., Pompilio, M., García-Cañada, L., Bertagnini, A., Benito-Saz,
751 M., Del Carlo, P., Sainz-Maza Aparicio, S., 2015. New insight into the 2011-2012 unrest and eruption of El
752 Hierro Island (Canary Islands) based on integrated geophysical, geodetical, and petrological data. Annals
753 of Geophysics 58, S0546. https://doi.org/10.4401/ag-6754
754 Mitchell, T., Smith, S., Anders, M., Di Toro, G., Nielsen, S., Cavallo, A., Beard, A., 2015. Catastrophic
755 emplacement of giant landslides aided by thermal decomposition: Heart Mountain, Wyoming. Earth and
756 Planetary Science Letters 411, 199-207. https://doi.org/10.1016/j.epsl.2014.10.051
757 Moscardelli, L., Wood, L., 2008. New classification system for mass transport complexes in offshore Trinidad.
758 Basin Research 20, 73-98. https://doi.org/10.1111/j.1365-2117.2007.00340.x

759 Palumbo, L., Benedetti, L., Bourlès, D., Cinque, A., Finkel, R., 2004. Slip history of the Magnola Fault (Apennines,
760 Central Italy) from ^{36}Cl surface exposure dating: evidence for strong earthquakes over the Holocene.
761 Earth and Planetary Science Letters 225, 163-176. https://doi.org/10.1016/j.epsl.2004.06.012
762 Paris, R., Ramalho, R.S., Madeira, J., Ávila, S., May, S.M., Rixhon, G., Engel, M., Brűckner, H., Herzog, M.,
763 Schukraft, G., Perez-Torrado, F.J., Rodriguez-Gonzales, A., Carracedo, J.C., Giachetti, T., 2018. Mega-
764 tsunami conglomerates and flank collapses of ocean volcanoes. Marine Geology 395, 168-187.
765 https://doi.org/ 10.1016/j.margeo.2017.10.004
766 Passchier, C., Trouw, R., 2005. Microtectonics. Springer, Berlin, 366 pp. https://doi.org/10.1007/3-540-29359-0
767 Poujol, A., Ritz, J.-F., Tahayt, A., Vernant, P., Condomines, M., Blard, P.-H., Billant, J., Vacher, L., Tibari, B., Hni,
768 L., Koulali Idrissi, A., 2014. Active tectonics of the Northern Rif (Morocco) from geomorphic and
769 geochronological data. Journal of Geodynamics 77, 70-88. https://doi.org/10.1016/j.jog.2014.01.004
770 Price, N., Johnson, S., Gerbi, C., West, D., 2012. Identifying deformed pseudotachylyte and its influence on the
771 strength and evolution of a crustal shear zone at the base of the seismogenic zone. Tectonophysics 518-
772 521, 63-83. https://doi.org/10.1016/j.tecto.2011.11.011
773 Protin, M., Blard, P.-H., Marrocchi, Y., Mathon, F., 2016. Irreversible adsorption of atmospheric helium on
774 olivine: a lobster pot analogy. Geochimica et Cosmochimica Acta 179, 76-88.
775 https://doi.org/10.1016/j.gca.2016.01.032
776 Rasa, R., Azzaro, R., Leonardi, O., 1996. Aseismic creep on faults and flank instability at Mount Etna Volcano,
777 Sicily. In: McGuire, W., Jones, A., Neuberg, J. (Eds.), Volcano Instability on the Earth and Other Planets.
778 Geological Society of London, Special Publication 110, 179-192.
779 https://doi.org/10.1144/GSL.SP.1996.110.01.14
780 Rempe, M., Smith, S., Ferri, F., Mitchell, T., Di Toro, G., 2014. Clast-cortex aggregates in experimental and
781 natural calcite bearing fault zones. Journal of Structural Geology 68, 142-157.
782 https://doi.org/10.1016/j.jsg.2014.09.007
783 Rowe, C., Fagereng, Å., Miller, J., Mapani, B., 2012. Signature of coseismic decarbonation in dolomitic fault
784 rocks of the Naukluft Thrust, Namibia. Earth and Planetary Science Letters 333-334, 200-210.
785 https://doi.org/10.1016/j.epsl.2012.04.030
786 Rowe, C., Griffith, W., 2015. Do faults preserve a record of seismic slip: a second opinion. Journal of Structural
787 Geology 78, 1-26. https://doi.org/10.1016/j.jsg.2015.06.006

788 Rowe, C., Lamothe, K., Rempe, M., Andrews, M., Mitchell, T., Di Toro, G., Clancy White, J., Aretusini, S., 2019.
789 Earthquake lubrication and healing explained by amorphous nanosilica. Nature Communications 10,
790 320. https://doi.org/10.1038/s41467-018-08238-y
791 Rowe, C., Moore, J., Meneghini, F., McKeirnan, A., 2005. Large scale pseudotachylytes and fluidized cataclasites
792 from an ancient subduction thrust fault. Geology 33, 937-940. https://doi.org/10.1130/G21856.1
793 Sagy, A., Brodsky, E., Axen, G., 2007. Evolution of fault surface roughness with slip. Geology 35, 283-286.
794 https://doi.org/10.1130/G23235A.1
795 Siebert, L., 1984. Large volcanic debris avalanches: characteristics of source areas, deposits, and associated
796 eruptions. Journal of Volcanology and Geothermal Research 22, 163-197. https://doi.org/10.1016/0377-
797 0273(84)90002-7
798 Siebert, L., 1992. Threats from debris avalanches. Nature 356, 658-659. https://doi:10.1038/356658a0
799 Smeraglia, L., Bettucci, A., Billi, A., Carminati, E., Cavallo, A., Di Toro, G., Natali, M., Passeri, D., Rossi, M.,
800 Spagnuolo, E., 2017. Microstructural evidence for seismic and aseismic slips along clay-bearing,
801 carbonate faults. Journal of Geophysical Research, Solid Earth 122, 3895-3915.
802 https://doi.org/10.1002/2017JB014042
803 Smith, S., Billi, A., Di Toro, G., Spiess, R., 2011. Principal slip zones in limestone: microstructural characterization
804 and implications for the seismic cycle (Tre Monti Fault, Central Apennines, Italy). Pure and Applied
805 Geophysics 168, 2365-2393. https://doi.org/10.1007/s00024-011-0267-5
806 Sorriso-Valvo, M., Gullà, G., Antronico, L., Tansi, C., Amelio, M., 1999. Mass movement, geologic structure, and
807 morphologic evolution of the Pizzotto-Greci Slope (Calabria, Italy). Geomorphology 30, 147-163.
808 https://doi.org/10.1016/S0169-555X(99)00051-3
809 Szérémèta, N., Laj, C., Guillou, H., Kissel, C., Mazaud, A., Carracedo, J.-C., 1999. Geomagnetic paleosecular
810 variation in the Brunhes period, from the island of El Hierro (Canary Islands). Earth and Planetary
811 Science Letters 165, 241-253. https://doi.org/10.1016/S0012-821X(98)00270-2
812 Tesei, T., Carpenter, B., Giorgetti, C., Scuderi, M., Sagy, A., Scarlato, P., Collettini, C., 2017. Friction and scale-
813 dependent deformation processes of large experimental carbonate faults. Journal of Structural Geology
814 100, 12-23. https://doi.org/10.1016/j.jsg.2017.05.008
815 Ui, T., Takarada, S., Yoshimoto, M., 2000. Debris avalanches. In: Sigurdsson, H., Houghton, B., McNutt, S.,
816 Rymer, H., Stix, J. (Eds.), Encyclopedia of Volcanoes. Academic Press, San Diego, pp. 617-626.

817 Ujiie, K., Tsutsumi, A., Kameda, J., 2011. Reproduction of thermal pressurization and fluidization of clay-rich
818 fault gouges by high-velocity friction experiments and implications for seismic slip in natural faults.
819 Geological Society of London, Special Publication 359, 267-285. https://doi.org/10.1144/SP359.15
820 Urgeles, R., Canals, M., Baraza, J., Alonso, B., 1996. The submarine El Golfo debris avalanche and the Canary
821 debris flow, west Hierro Island: the last major slides in the Canary Archipelago. Geogaceta 20, 390-393.
822 Urgeles, R., Canals, M., Baraza, J., Alonso, B., Masson, D., 1997. The most recent megalandslides on the Canary
823 Islands: the El Golfo debris avalanche and the Canary debris flow, west El Hierro Island. Journal of
824 Geophysical Research, Solid Earth 102, 20305-20323. https://doi.org/10.1029/97JB00649
825 Verberne, B., De Bresser, J., Niemeijer, A., Spiers, C., De Winter, M.D., Plümper, O., 2013. Nanocrystalline slip
826 zones in calcite fault gouge show intense crystallographic preferred orientation: crystal plasticity at
827 subseismic slip rates at 18-150°C. Geology 41, 863-866. https://doi.org/10.1130/G34279.1
828 Walter, T.R., Haghighi, M.H., Schneider, F.M., Coppola D, Motagh, M., Saul, J., Babeyko, A., Dahm, T., Troll, V.R.,
829 Tilmann, F., Heimann, S., Valade, S., Triyono, R., Khomarudin, R., Kartadinata, N., Laiolo, M., Massimetti,
830 F., Gaebler, P., 2019. Complex hazard cascade culminating in the Anak Krakatau sector collapse. Nature
831 Communications 10, 4339. https://doi.org/10.1038/s41467-019-12284-5
832 Weidinger, J., Korup, O., Munack, H., Altenberger, U., Dunning, S., Tippelt, G., Lottermoser, W., 2014. Giant
833 rockslides from the inside. Earth and Planetary Science Letters 389, 62-73.
834 https://doi.org/10.1016/j.epsl.2013.12.017
835 Zimmermann, L., Avice, G., Blard, P.-H., Marty, B., Füri, E., Burnard, P., 2018. A new all-metal induction furnace
836 for noble gas extraction. Chemical Geology 480, 86-92. https://doi.org/10.1016/j.chemgeo.2017.09.018

Figure captions

Figure 1 A shaded topographic and bathymetric relief map of El Hierro, Canary Islands, overlain by a geological map simplified from Ancochea et al. (2004). The inset shows an aerial image of the studied fault outcrop. SAL: San Andrés Landslide.

Figure 2 (A) General view of the San Andrés Fault outcrop showing the location of each sampling site. The numbers in parentheses after COS samples 1-5 indicate the estimated exposure ages in ka. (B) Detailed view of the fault outcrop which shows a series of conspicuous vertical or subvertical slickenlines and the whitish layer adorning the recently exposed parts of its surface; (C) Contact between the footwall (left) and the hanging wall (right); (D) Detailed view of the oxidised rock visible in the footwall of the fault which reflects the presence of fine grained Fe-oxides and Fe-hydroxides. (E, F) Samples used for microstructural analysis: (E1) hand sample MSA1 shows slickenlines composed of the whitish layer - note the dashed line parallel to the slickenlines; (E2) closeup view of the slickenlines, (E3) rock slab used to extract thin sections shows the whitish layer that covers the cataclasite and breccia. The black rectangles mark the positions of Figures 5-6; (F1) core sample MSA2 drilled perpendicular to the fault surface shows large clasts in the breccia and white layer - red dashed line highlights the orientation of the slickenlines; (F2) rock slab shows the gradual increase in oxidation of the breccia towards the fault surface; (F3) thin section shows the sharpness of the slip surface and the barely-visible white silica layer. The black rectangle marks the location of Figure 7.

Figure 3 Structural analysis of the surface of the San Andrés Fault outcrop conducted on the basis of a remotely sensed UAV DTM. (A) Slope gradient map giving a ground plan view presented in inverted greyscale and showing distinct sets of striations and elongated bumps. (B) Slope gradient map giving a fault perpendicular view presented in inverted greyscale and visualised in three dimensions (for reference see the right hand part of the fault in A). (C) Orientation of the fault surface and the striations revealed by the morphostructural analysis of the UAV DTM. The

stereoplot is in azimuthal projection of the lower hemisphere while the different coloured arrows represent distinct sets of striations and elongated protrusions.

Figure 4 The interpolated R-values obtained through Schmidt hammer sampling on the San Andrés Fault. The size of the black dots illustrates the rock hardness at each of the test sites.

Figure 5 Photomicrographs and BSE images of rock from the San Andrés Fault, sample MSA1. First area presented (A) under plane polarised light, (B) under cross polarised light, (C) as a sketch, (D) in BSE, and (E-F) in elemental maps. These show tectonic breccia (TB) covered by a cataclastic layer (CL) which is, in turn, covered by a silica layer (SL). The cataclasite cuts both the tectonic breccia and a zeolite vein (Z) and has preserved P-foliation and a winged inclusion. The boundary between the silica layer and the adjacent cataclastic layer is sharp with high interference bands, characteristic of recrystallisation. The area is rotated during analysis and the sense of shear is marked on the sketch. Second area presented (G) under plane polarised light, (H) under cross polarised light, (I) as a sketch, (J) in BSE, and (K-L) in elemental maps. These show tectonic breccia (TB) with zeolite veins (Z) covered by a thinner cataclastic layer (CL) and a thicker silica layer (SL). The fault slip surface is subhorizontal with a top-to-right shear direction. The boundary between the cataclastic layer and the silica layer is marked by high intensity bands of recrystallised material. The silica layer preserves clast-cortex aggregates (CCA) and flow bands (FB) along with parallel P- and Y- shears. The elongated void was most probably a clast-cortex aggregate lost during preparation of the sample.

Figure 6 Photomicrographs and BSE images of rock from the San Andrés Fault, sample MSA1. Area presented in (A) under plane polarised light, (B) under cross polarised light, (C) under cross polarised light using a gypsum tint plate, (D) in BSE, and (E) as a sketch. These show tectonic breccia (TB) covered by a silica layer (SL). The tectonic breccia was cut during deformation which resulted in truncated clasts (TC) while the silica layer preserves clast-cortex aggregates (CCA), a cataclastic sublayer (CL), and flow bands (FB). These flow bands show a positive birefringence, in contrast to the rest of the silica layer, as evidenced by the second order blue interference colour in

(C). The rectangles in (D) indicate regions highlighted in (F-I): (F) new crystals growing in a void surrounded by ultrafine grained to amorphous matrix, (G) a large clast-cortex aggregate with a complex cortex and elongated clast in its core, (H) a lensoid of reworked cataclasite, and (I) two smaller clast-cortex aggregates and new crystals growing in the void. The fault slip surface is horizontal with a top-to-right shear direction.

Figure 7 Photomicrographs and BSE images of rock from the San Andrés Fault, sample MSA2. Area presented in (A) under plane polarised light, (B) under cross polarised light using a gypsum tint plate, and (C) as a sketch. These show a large truncated clast (TC) in the tectonic breccia (TB) cut by cataclasite (CL) and covered by a silica layer (SL) which has flow bands (FB) and clast-cortex aggregates (CCA). The rectangle in (A) indicates the region highlighted in (D-F). In (D-F) elemental maps show P-foliation in the cataclastic layer along with clast-cortex aggregates and flow bands in the silica layer. Dashed lines highlight characteristics presented in the sketch. The fault slip surface is horizontal with a top-to-right shear direction.

Figure 8 A conceptual model for the development of the San Andrés Fault system over the last 550 ka based on Day et al. (1997), Carracedo et al. (1997), Széréméta et al. (1999), León et al. (2017), and the findings presented herein. The uppermost labels denote the main geological events to have taken place on El Hierro, i.e. rotation and volcanism, while those beneath denote the supposed age ranges for each of the giant landslides. The proposed timing of activity on the San Andrés Fault is presented underneath the timeline: the first slip event is associated with the formation of the cataclasite while the second slip event is associated with the formation of the silica layer. The time axis depicts thousands of years before present.

Figure 9 A conceptual model for the development of the surface of the San Andrés Fault. Prior to slip a tectonic breccia, of basaltic origin, hosted zeolite veins, as shown in green. During the first slip event the tectonic breccia was sheared and a foliated cataclasite formed, as shown in red. During the second slip event both the host rock and foliated cataclasite were sheared and a silica layer formed with clast-cortex aggregate and flow bands, as shown in blue.

Table captions

Table 1 Results of the cosmogenic ^{3}He exposure dating for five samples obtained from the San Andrés Fault.

Supp. Tab. A Chemical composition of the five samples obtained from the San Andrés Fault for cosmogenic ^{3}He exposure dating (COS1 - COS5).

Table 1

Click here to download Table: Blahut et al. 2019 - Tectonophysics Table.pdf

Sample	Size (mm)	Extraction method	Mass (g)	$^{3}He_{melt}$ (10^{6} at.g^{-1})	$^{4}He_{melt}$ (10^{12} at.g^{-1})	$^{3}He_{cos\ min}$ (10^{6} at.g^{-1})	$^{3}He_{cos\ max}$ (10^{6} at.g^{-1})	Dip slope (°)	Local scaling factor	Minimal exposure (ka)	Maximum exposure (ka)
COS5-III	0.5 - 1	1 min vacuum crushing / 100 strokes	0.5	0.195 ± 0.096	0.014 ± 0.001						
COS5-III	0.5 - 2	5 min vacuum crushing / 500 strokes	0.5	4.27 ± 0.16	0.36 ± 0.01						
COS-1	0.5 - 2	Furnace 1700°C / 15 min	0.1182	2.22 ± 0.39	13.62 ± 0.21	< 2	2.22 ± 2.04	75	0.68	< 20	21 ± 20
COS-2 and 3	0.2 - 2	Furnace 1700°C / 15 min	0.1206	2.95 ± 0.39	0.62 ± 0.02	< 2	2.95 ± 2.04	67	0.75	< 21	26 ± 18
COS - 4I	0.2 - 2	Furnace 1700°C / 15 min	0.3007	6.46 ± 0.25	2.05 ± 0.03	2.19 ± 2.02	6.46 ± 2.02	71	0.7	21 ± 19	61 ± 19
COS - 4II	0.2 - 2	Furnace 1700°C / 15 min	0.2089	7.13 ± 0.32	1.21 ± 0.02	2.85 ± 2.03	7.13 ± 2.03	65	0.78	24 ± 17	60 ± 17
COS - 5II	0.25 - 0.5	Furnace 1700°C / 15 min	0.2097	10.48 ± 0.37	1.99 ± 0.03	6.21 ± 2.03	10.48 ± 2.03	65	0.78	52 ± 17	88 ± 17
COS - 5III	0.5 - 2	Furnace 1700°C / 15 min	0.1939	16.16 ± 0.48	1.63 ± 0.03	11.88 ± 2.06	16.16 ± 2.06	65	0.78	100 ± 17	136 ± 17
COS - 5III	0.5 - 2	Furnace 1700°C / 15 min	0.2606	21.75 ± 0.53	2.16 ± 0.04	17.47 ± 2.07	21.75 ± 2.07	65	0.78	147 ± 17	183 ± 17
Age of lava eruption: (1.05 +- 0.02) Ma											
All sample are a mixture of pure olivines and pyroxenes											
Ra = 1.384×10^{-6}											

Table 1 Results of the cosmogenic ^{3}He exposure dating for five samples obtained from the San Andrés Fault.

Figure 1 (with caption below and on the same page)

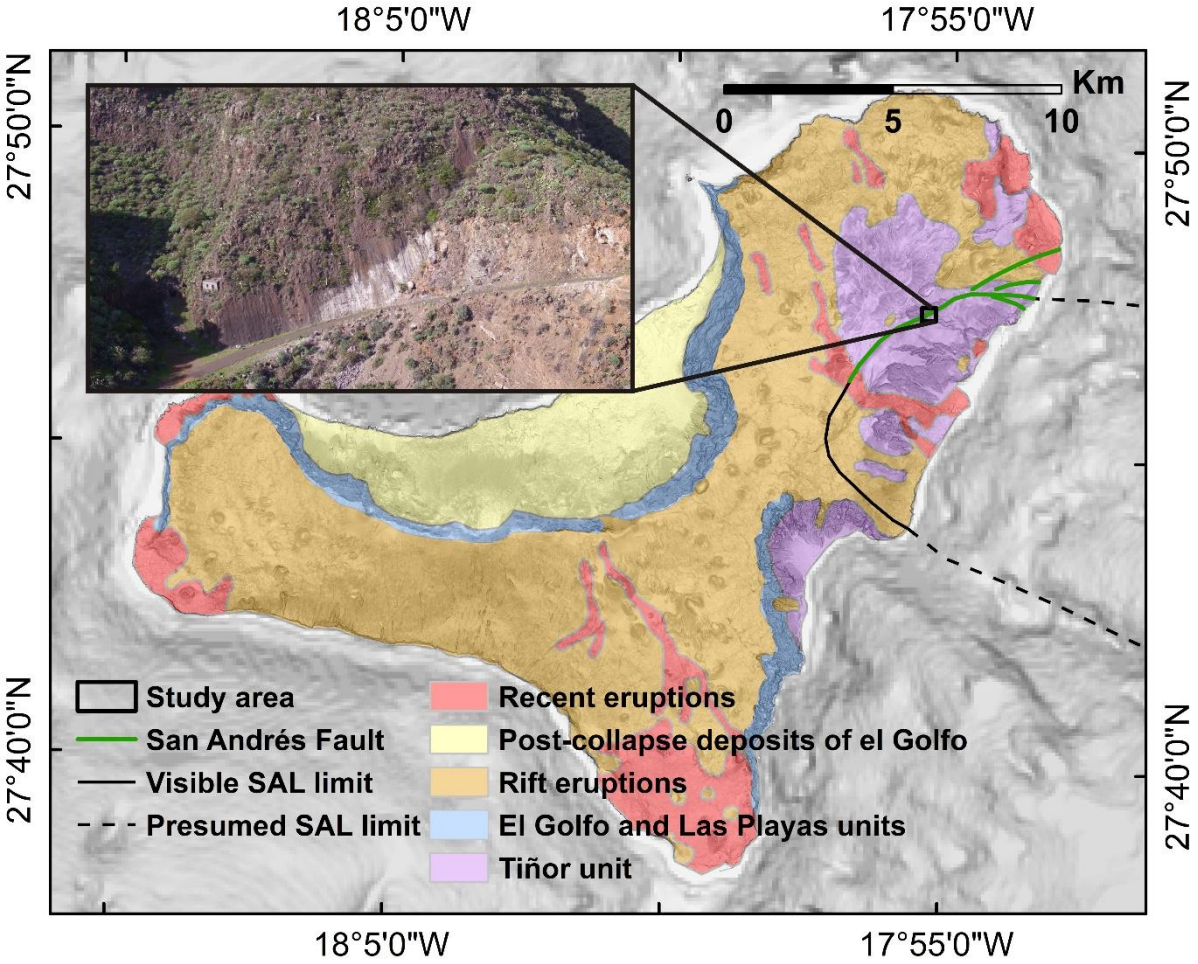

Figure 1 A shaded topographic and bathymetric relief map of El Hierro, Canary Islands, overlain by a geological map simplified from Ancochea et al. (2004). The inset shows an aerial image of the studied fault outcrop. SAL: San Andrés Landslide.

Figure 2 (with caption below and on the same page)

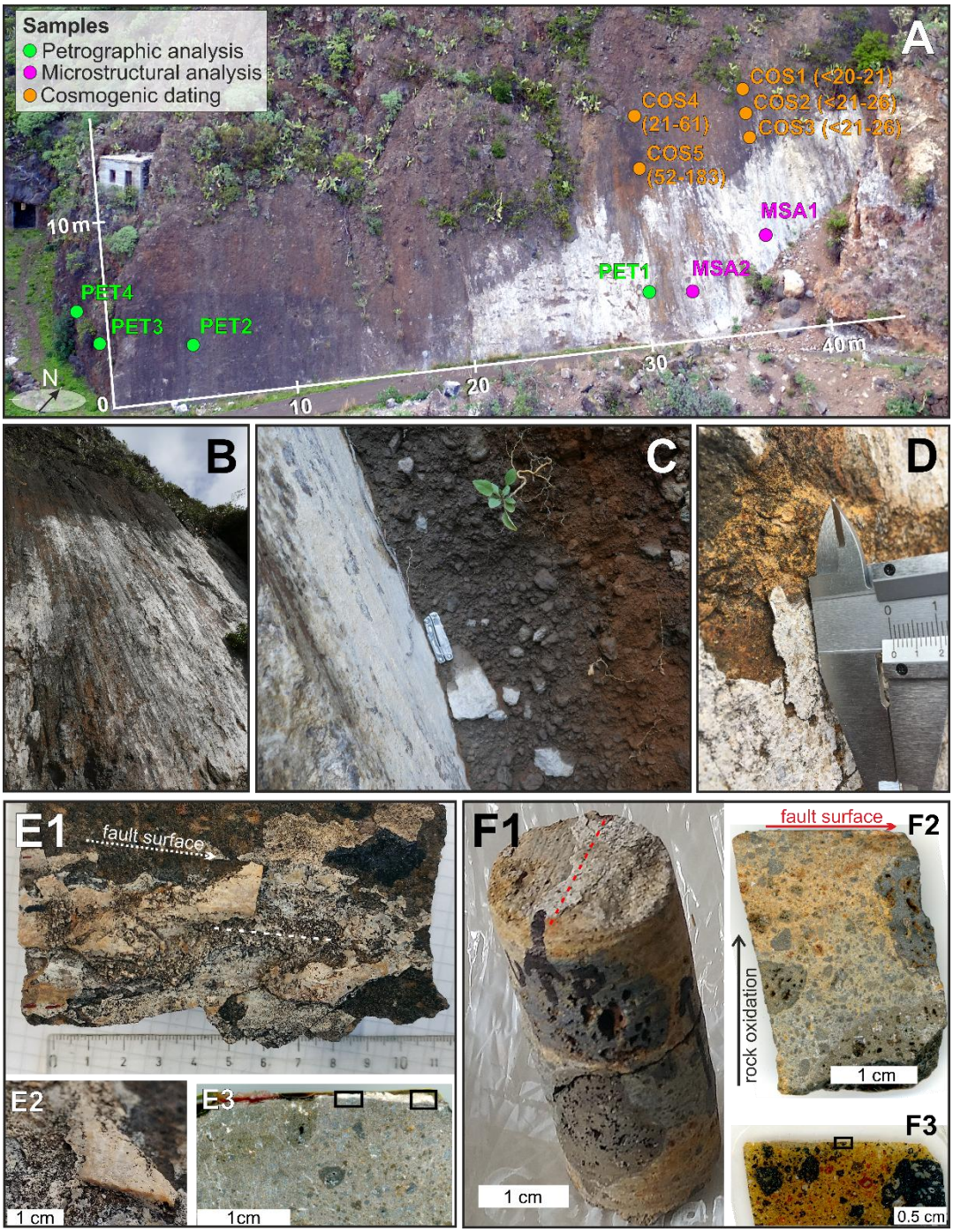

Figure 2 (A) General view of the San Andrés Fault outcrop showing the location of each sampling site. The numbers in parentheses after COS samples 1-5 indicate the estimated exposure ages in ka. (B) Detailed view of the fault outcrop which shows a series of conspicuous vertical or subvertical slickenlines and the whitish layer adorning the recently exposed parts of its surface; (C) Contact between the footwall (left) and the hanging wall (right); (D) Detailed view of the oxidised rock visible in the footwall of the fault which reflects the presence of fine grained Fe-oxides and Fe-hydroxides. (E, F) Samples used for microstructural analysis: (E1) hand sample MSA1 shows slickenlines composed of the whitish layer - note the dashed line parallel to the slickenlines; (E2) closeup view of the slickenlines, (E3) rock slab used to extract thin sections shows the whitish layer that covers the cataclasite and breccia. The black rectangles mark the positions of Figures 5-6; (F1) core sample MSA2 drilled perpendicular to the fault surface shows large clasts in the breccia and white layer - red dashed line highlights the orientation of the slickenlines; (F2) rock slab shows the gradual increase in oxidation of the breccia towards the fault surface; (F3) thin section shows the sharpness of the slip surface and the barely-visible white silica layer. The black rectangle marks the location of Figure 7.

Figure 3 (with caption below and on the same page)

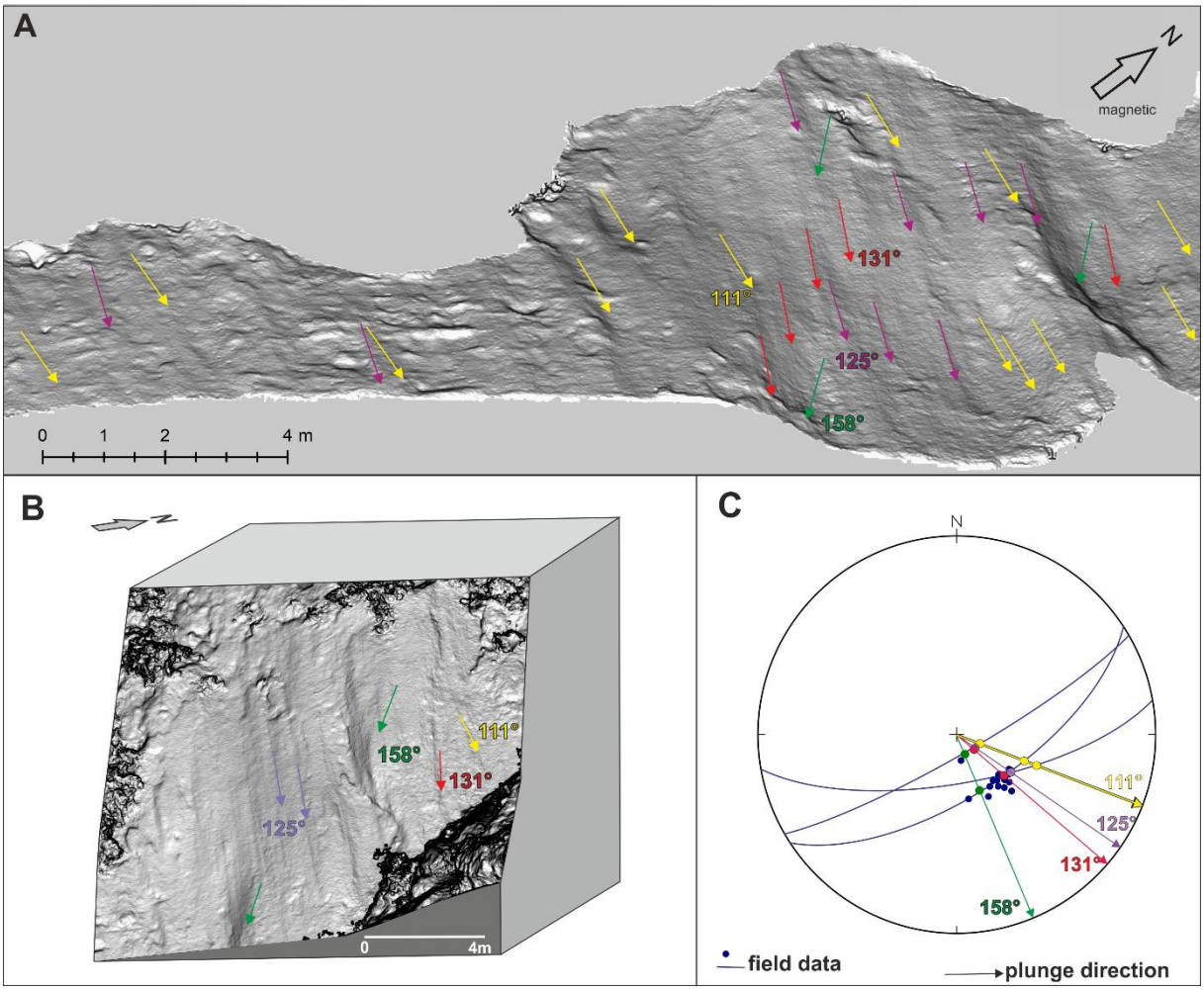

Figure 3 Structural analysis of the surface of the San Andrés Fault outcrop conducted on the basis of a remotely sensed UAV DTM. (A) Slope gradient map giving a ground plan view presented in inverted greyscale and showing distinct sets of striations and elongated bumps. (B) Slope gradient map giving a fault perpendicular view presented in inverted greyscale and visualised in three dimensions (for reference see the right hand part of the fault in A). (C) Orientation of the fault surface and the striations revealed by the morphostructural analysis of the UAV DTM. The stereoplot is in azimuthal projection of the lower hemisphere while the different coloured arrows represent distinct sets of striations and elongated protrusions.

Figure 4 (with caption below and on the same page)

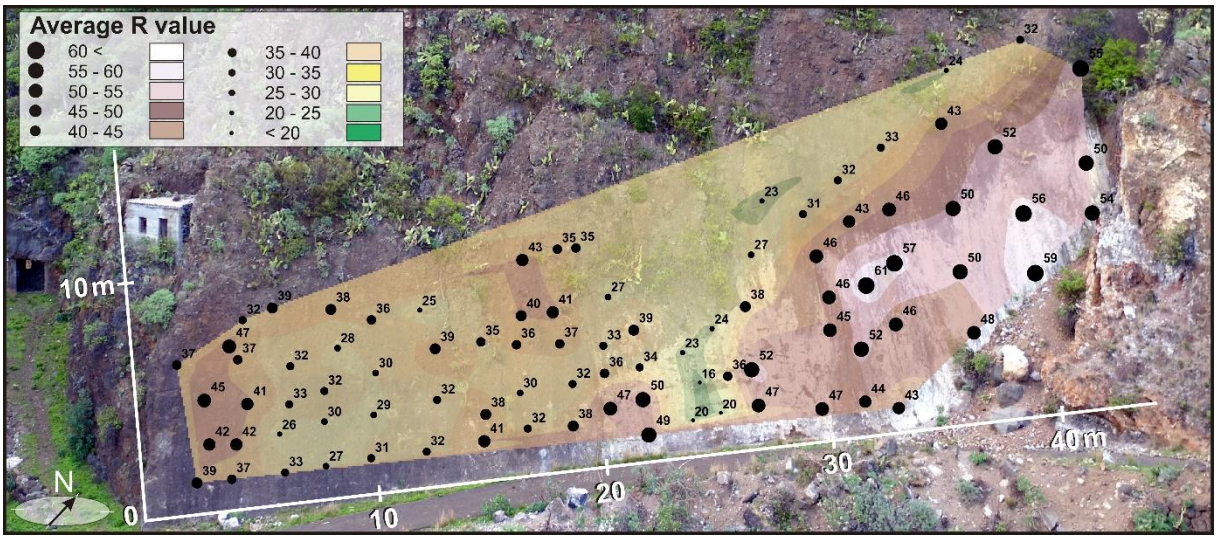

Figure 4 The interpolated R-values obtained through Schmidt hammer sampling on the San Andrés Fault. The size of the black dots illustrates the rock hardness at each of the test sites.

Figure 5 (with caption below and on the same page)

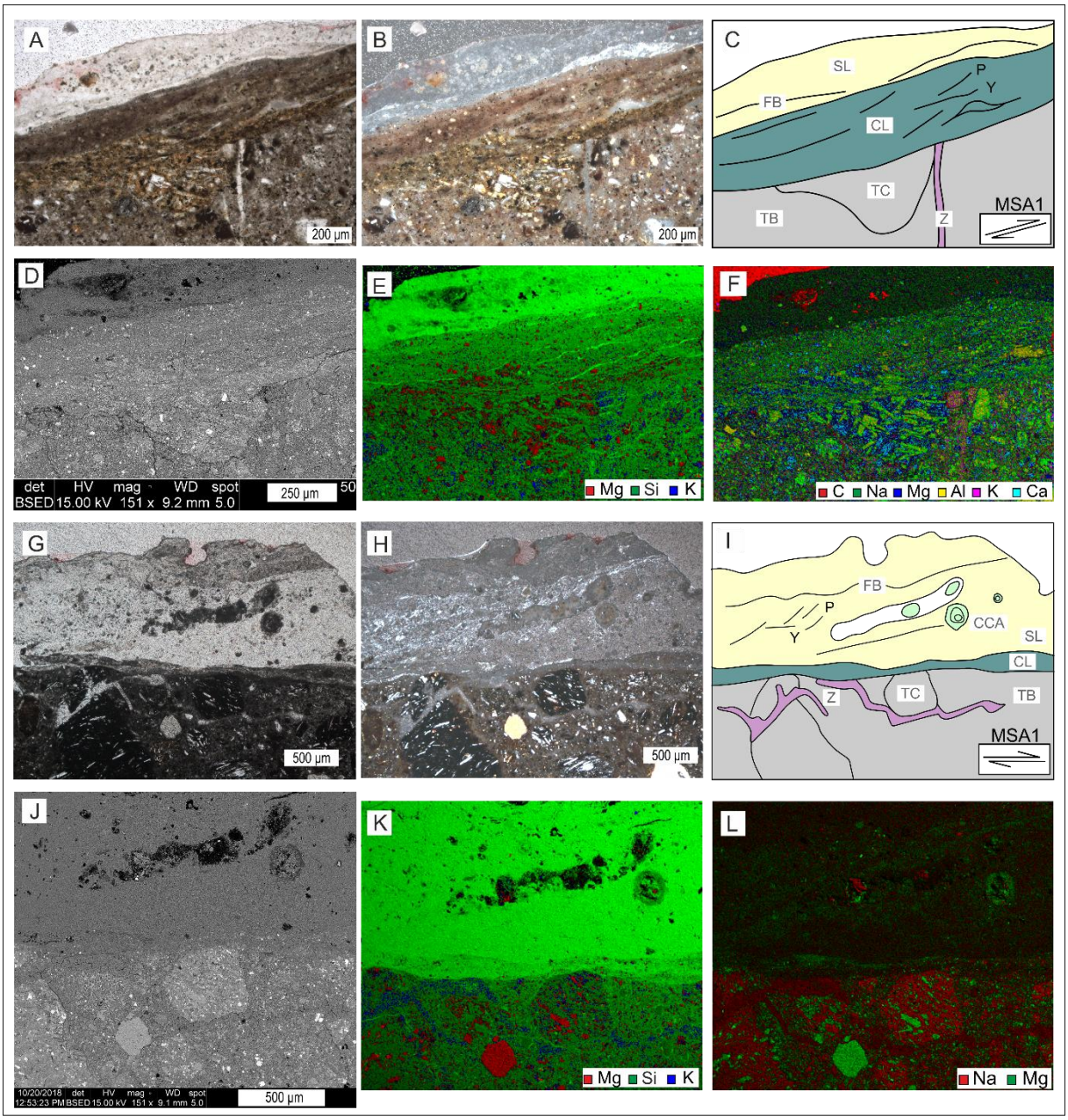

Figure 5 Photomicrographs and BSE images of rock from the San Andrés Fault, sample MSA1. First area presented (A) under plane polarised light, (B) under cross polarised light, (C) as a sketch, (D) in BSE, and (E-F) in elemental maps. These show tectonic breccia (TB) covered by a cataclastic layer (CL) which is, in turn, covered by a silica layer (SL). The cataclasite cuts both the tectonic breccia and a zeolite vein (Z) and has preserved P-foliation and a winged inclusion. The boundary between the silica layer and the adjacent cataclastic layer is sharp with high interference bands, characteristic of recrystallisation. The area is rotated during analysis and the sense of shear is marked on the sketch. Second area presented (G) under plane polarised light, (H) under cross polarised light, (I) as a sketch, (J) in BSE, and (K-L) in elemental maps. These show tectonic breccia (TB) with zeolite veins (Z) covered by a thinner cataclastic layer (CL) and a thicker silica layer (SL). The fault slip surface is subhorizontal with a top-to-right shear direction. The boundary between the cataclastic layer and the silica layer is marked by high intensity bands of recrystallised material. The silica layer preserves clast-cortex aggregates (CCA) and flow bands (FB) along with parallel P- and Y- shears. The elongated void was most probably a clast-cortex aggregate lost during preparation of the sample.

Figure 6 (with caption below and on the same page)

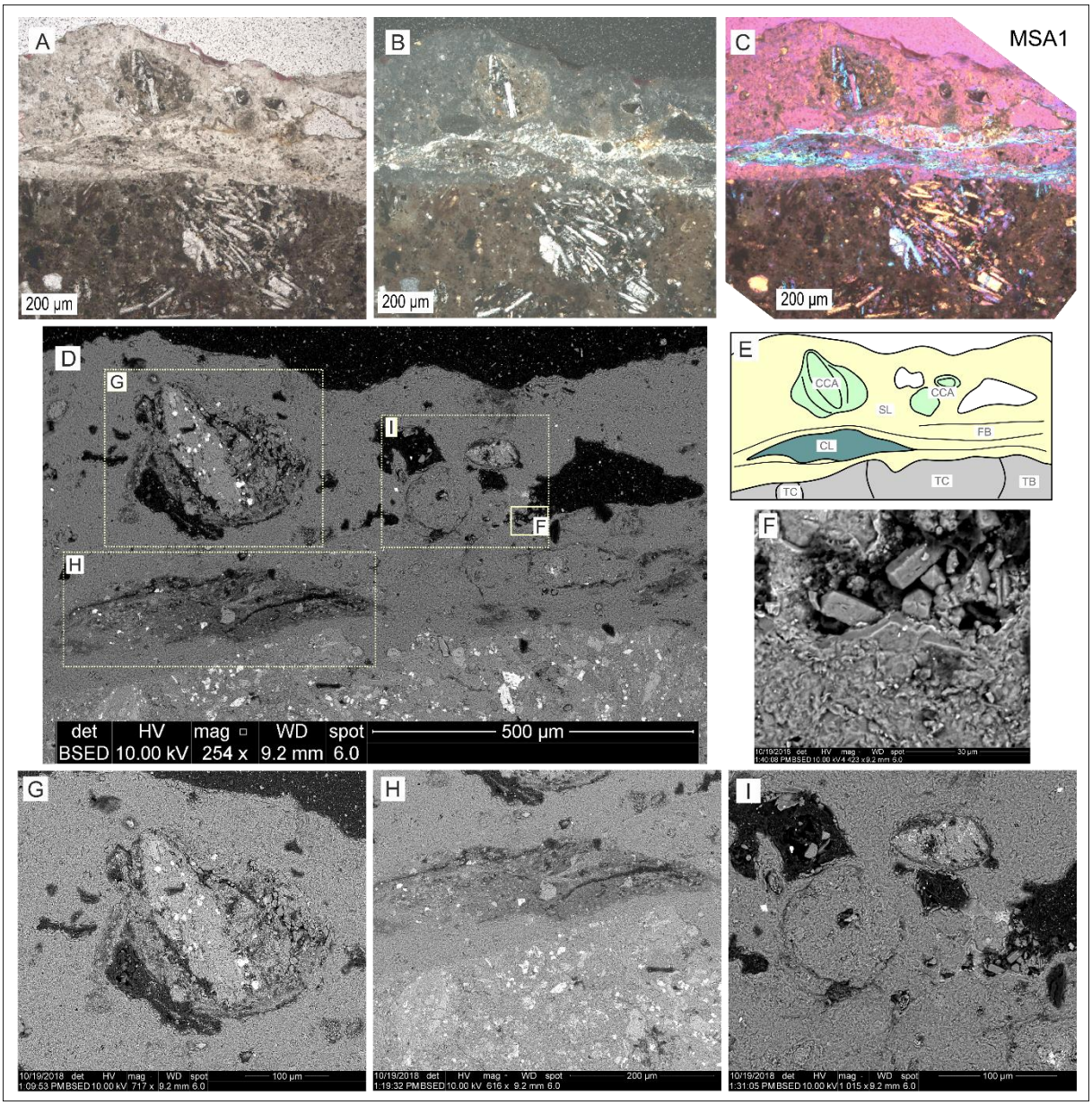

Figure 6 Photomicrographs and BSE images of rock from the San Andrés Fault, sample MSA1. Area presented in (A) under plane polarised light, (B) under cross polarised light, (C) under cross polarised light using a gypsum tint plate, (D) in BSE, and (E) as a sketch. These show tectonic breccia (TB) covered by a silica layer (SL). The tectonic breccia was cut during deformation which resulted in truncated clasts (TC) while the silica layer preserves clast-cortex aggregates (CCA), a cataclastic sublayer (CL), and flow bands (FB). These flow bands show a positive birefringence, in contrast to the rest of the silica layer, as evidenced by the second order blue interference colour in (C). The rectangles in (D) indicate regions highlighted in (F-I): (F) new crystals growing in a void surrounded by ultrafine grained to amorphous matrix, (G) a large clast-cortex aggregate with a complex cortex and elongated clast in its core, (H) a lensoid of reworked cataclasite, and (I) two smaller clast-cortex aggregates and new crystals growing in the void. The fault slip surface is horizontal with a top-to-right shear direction.

Figure 7 (with caption below and on the same page)

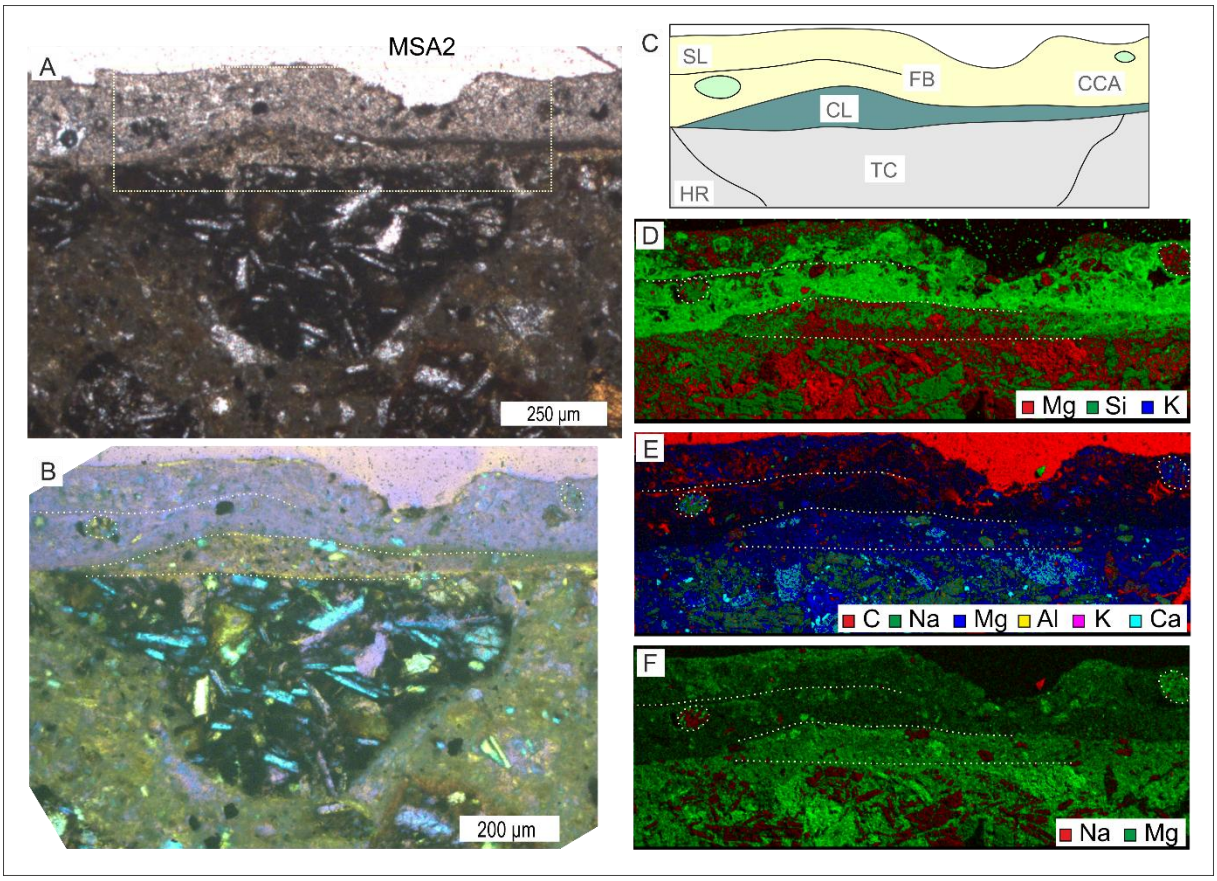

Figure 7 Photomicrographs and BSE images of rock from the San Andrés Fault, sample MSA2. Area presented in (A) under plane polarised light, (B) under cross polarised light using a gypsum tint plate, and (C) as a sketch. These show a large truncated clast (TC) in the tectonic breccia (TB) cut by cataclasite (CL) and covered by a silica layer (SL) which has flow bands (FB) and clast-cortex aggregates (CCA). The rectangle in (A) indicates the region highlighted in (D-F). In (D-F) elemental maps show P-foliation in the cataclastic layer along with clast-cortex aggregates and flow bands in the silica layer. Dashed lines highlight characteristics presented in the sketch. The fault slip surface is horizontal with a top-to-right shear direction.

Figure 8 (with caption below and on the same page)

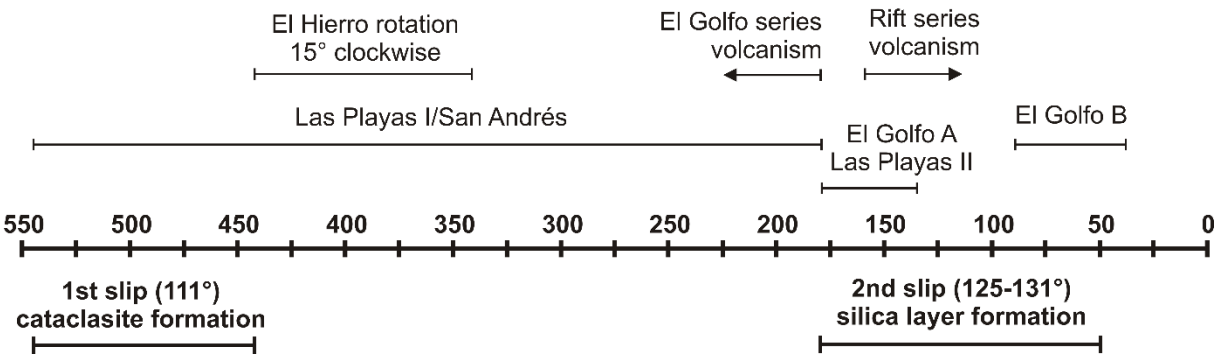

Figure 8 A conceptual model for the development of the San Andrés Fault system over the last 550 ka based on Day et al. (1997), Carracedo et al. (1997), Széréméta et al. (1999), León et al. (2017), and the findings presented herein. The uppermost labels denote the main geological events to have taken place on El Hierro, i.e. rotation and volcanism, while those beneath denote the supposed age ranges for each of the giant landslides. The proposed timing of activity on the San Andrés Fault is presented underneath the timeline: the first slip event is associated with the formation of the cataclasite while the second slip event is associated with the formation of the silica layer. The time axis depicts thousands of years before present.

Figure 9 (with caption below and on the same page)

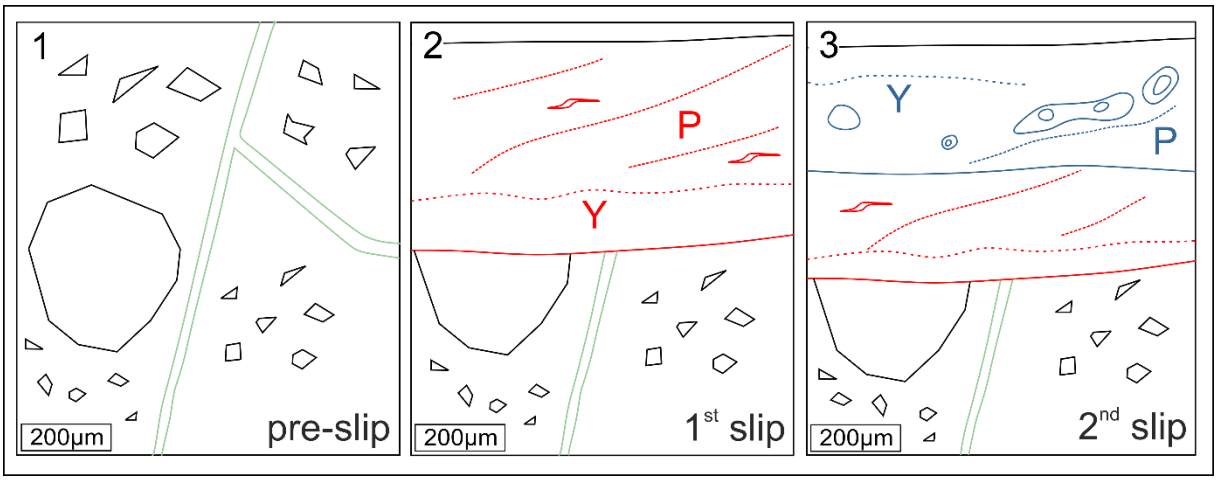

Figure 9 A conceptual model for the development of the surface of the San Andrés Fault. Prior to slip a tectonic breccia, of basaltic origin, hosted zeolite veins, as shown in green. During the first slip event the tectonic breccia was sheared and a foliated cataclasite formed, as shown in red. During the second slip event both the host rock and foliated cataclasite were sheared and a silica layer formed with clast-cortex aggregate and flow bands, as shown in blue.

Supplementary Table

Click here to download Supplementary material for online publication only: Blahut et al. 2019 - Tectonophysics SuppTable.pdf

***Credit Author Statement**

Jan Blahůt: Conceptualization, Methodology, Formal analysis, Writing – Original draft, Writing – Review and editing, Visualization, Supervision, Project Administration, Funding Acquisition

Ivanka Mitrovic-Woodell: Methodology, Validation, Formal Analysis, Investigation, Writing – Original draft, Writing – Review and editing, Resources

Ivo Baroň: Methodology, Investigation, Writing – Original draft

Miloš René: Methodology, Investigation, Writing – Original draft, Writing – Review and editing

Matt Rowberry: Methodology, Investigation, Writing – Original draft, Writing – Review and editing

Pierre-Henri Blard: Methodology, Investigation, Writing – Original draft

Filip Hartvich: Methodology, Investigation, Writing – Original draft, Writing – Review and editing

Jan Balek: Data Curation

Stavros Meletlidis: Investigation

***Declaration of Interest Statement**

Declaration of interests

☒ The authors declare that they have no known competing financial interests or personal relationships that could have appeared to influence the work reported in this paper.

☐The authors declare the following financial interests/personal relationships which may be considered as potential competing interests:

Jan BLAHŮT, Ivanka MITROVIC-WOODELL, Ivo BAROŇ, Miloš RENÉ, Matt ROWBERRY, Pierre-Henri BLARD,

Filip HARTVICH, Jan BALEK, Stavros MELETLIDIS